UiT The Arctic University of Norway

Faculty of Science and Technology
Department of Physics and Technology

Comparative performance analysis of two high-latitude solar photovoltaic systems

Frank Martin Fossland

EOM-3901 Master's thesis in Energy, Climate and Environment
May 2023

Abstract

The global energy demand and the urgency to limit greenhouse gas emissions require a transition to cleaner energy sources. Solar energy harvesting is a compelling solution because it can harness the sun's enormous resources. Solar photovoltaic technology is widely adopted worldwide due to being versatile, adaptable, and mature. However, low solar irradiation and harsh weather conditions limit its deployment in high-latitude regions. A significant research gap exists on the viability of technologies and addressing climate-related challenges. The research gap hinders further development because of a broad perception that solar photovoltaic technology is unviable in these regions.

This thesis aims to fill the research gap by performing a comparative performance analysis of a vertically installed bifacial heterojunction technology (HJT) system ("OES" system) and a 10°-tilted monofacial polycrystalline silicon (pc-Si) system ("ILP" system), both installed in Tromsø, Norway (69°N). The core purpose of the research is for our findings to shape the future deployments of solar photovoltaic systems in the regions.

Our study investigates and compares system performances between September 20, 2022, and April 30, 2023. We collect energy production data from the systems and perform full-year simulations in PVSyst to estimate expected performances under typical and ideal weather conditions. We use the collected data to calculate industry-standard energy performance metrics, while the simulations help identify critical factors influencing system performances.

The results show that the vertically installed bifacial HJT technology system exhibited a superior performance across all performance metrics, including 2.1% higher availability, 230% higher specific yield, 20.1% higher performance ratio, and 1.9% higher capacity factor.

Our study concludes that the vertically installed bifacial HJT technology system performed better than the 10°-tilted monofacial pc-Si system during the research period. The decisive factor for the superior performance was its ability to withstand snow accumulation and capitalize on increased albedo, indicating that it is a viable installation in winter conditions. In contrast, light snowfall could render the monofacial pc-Si system's power output zero, and an accumulated layer of snow remained in place for a long time. Therefore, we conclude that the installation is less suited for snowy conditions.

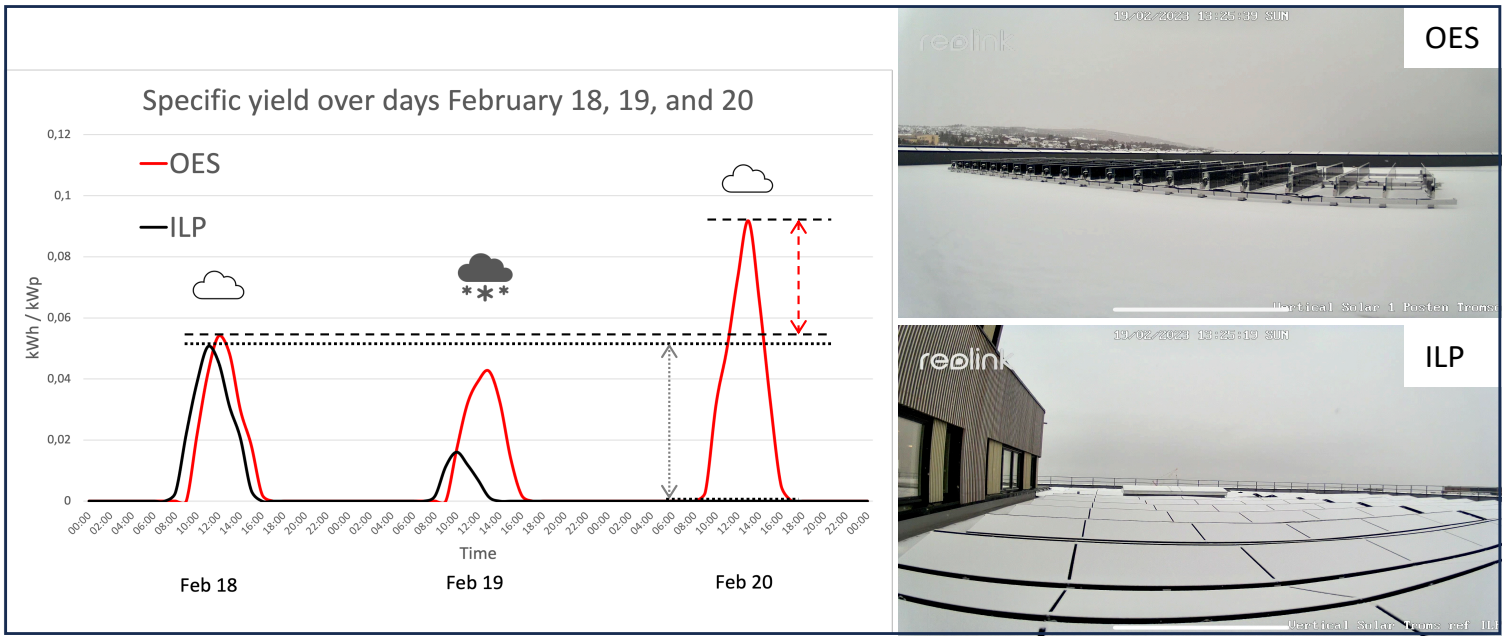

$\sum_{ILP} A = 19.4\% < \sum_{OES} A = 21.5\%$

$\sum_{ILP} SY = 44.39 \frac{kWh}{kWp} < \sum_{OES} SY = 146.31 \frac{kWh}{kWp}$

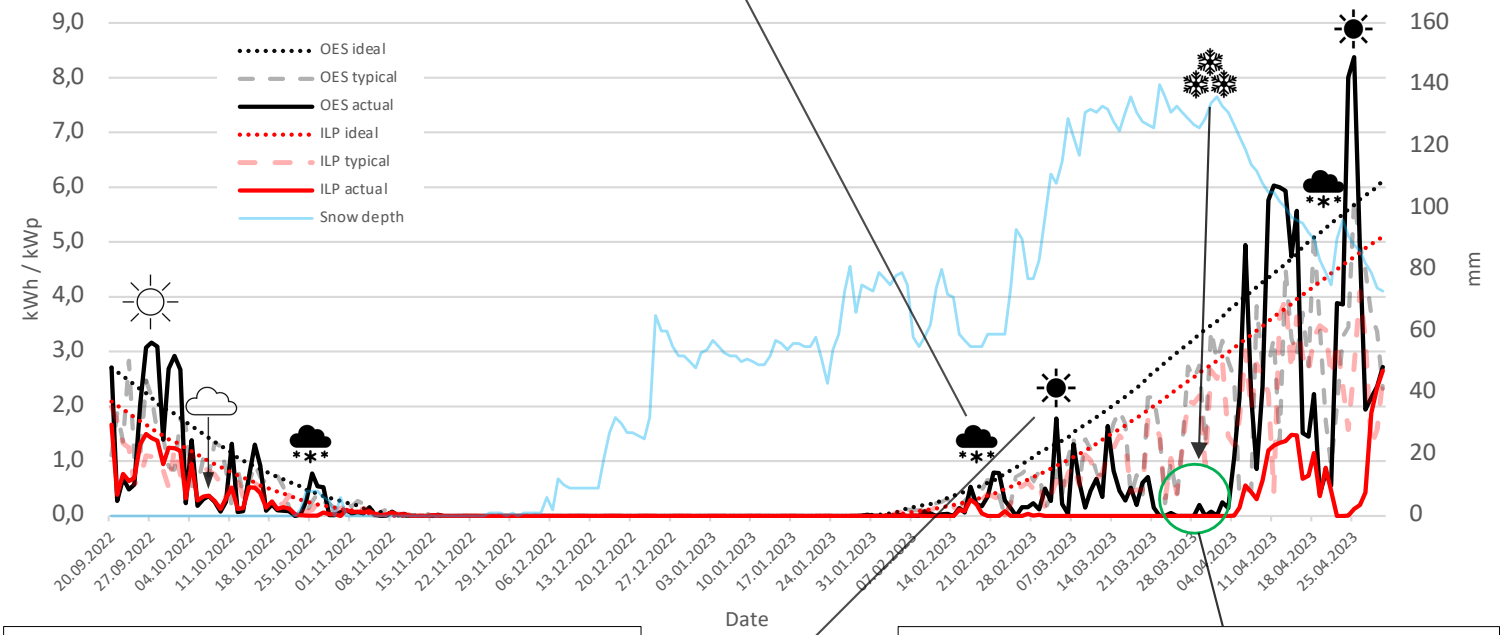

$\sum_{ILP} PR = 21.2\% << \sum_{OES} PR = 41.3\%$

$\sum_{ILP} CF = 0.83\% < \sum_{OES} CF = 2.73\%$

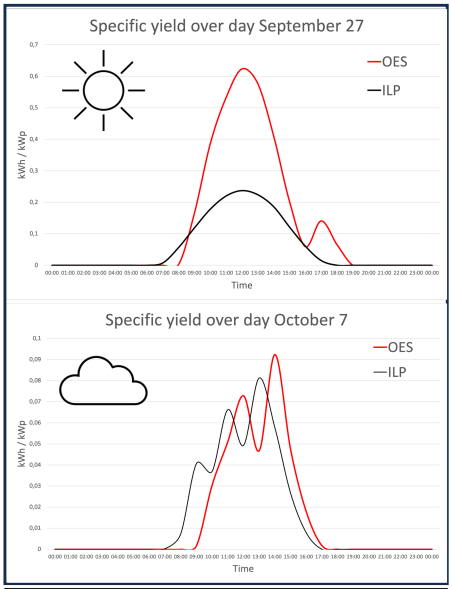

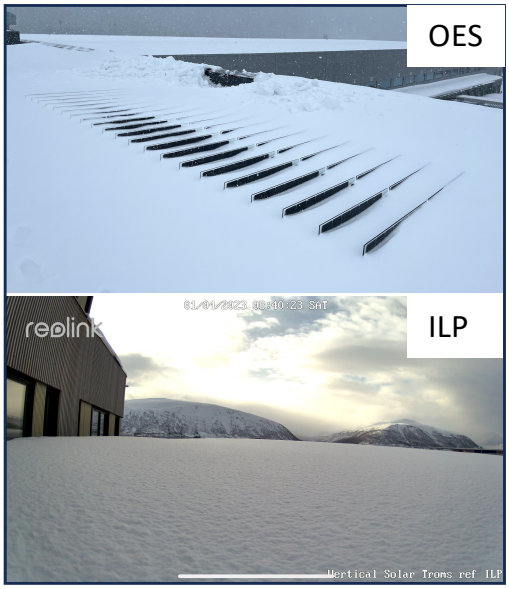

Specific yield on typical clear weather and cloudy days.

The systems on a clear weather day in March.

The systems at the peak of snow accumulation.

Acknowledgments

I want to thank the University of Tromsø and my classmates for five enriching and captivating years of education. I am also grateful to my supervisor, Igor Ezau, for pointing me in the right direction with my thesis and helping me along the way.

I would further like to thank Over Easy Solar's enthusiastic and professional employees for the opportunity to participate in this exciting project. It has been an absolute pleasure. Eirik Lockertsen (Solbes) and Rolf Skogan (Posten) have also been of massive help during the entire process, contributing to the success of this endeavor.

To my beloved family and friends, I cannot thank you enough for your support and encouragement throughout my academic journey. I must give a heartfelt mention to my fiancé, Ane, whose unwavering support and presence have been a true source of strength and inspiration for me.

Frank Martin Fossland
Tromsø, May 2023

List of Contents

List of Figures

List of Tables

List of Abbreviations

Abbreviation	Explanation
A	Availability
AM	Air Mass
API	Application Programming Interface
ARC	Anti-Reflection Coating
CF	Capacity Factor
EVA	Ethylene Vinyl Acetate
GHI	Global Horizontal Irradiance
HJT	Heterojunction Technology
ILP	*Institutt for Lærerutdanning og Pedagogikk* (Norwegian)
ITO	Indium Tin Oxide
KGPV	Köppen-Geiger-Photovoltaic
MPP	Maximum Power Point
MPPT	Maximum Power Point Tracker
OES	Over Easy Solar
PR	Performance Ratio
PV	Photovoltaic
STC	Standard Testing Conditions
SY	Specific Yield
TMY	Typical Meteorological Year

Fundamental constants

Symbol	Quantity	Value	Unit
c	Speed of light in vacuum	299 792 458	ms^{-1}
h	Planck's constant	$4.135\ 667 \ldots \cdot 10^{-15}$	eVs

Terminology

Term	Definition
Absorption	The interaction of incident electromagnetic radiation with the atmosphere, in which the receiving molecule converts the incident energy into internal energy, eventually transferring the energy to the surrounding gases [1].
Albedo	The fraction of light reflected by a surface, typically given as a percentage or a decimal number, where 1.0 indicates a perfect reflector and 0.0 indicates a perfect absorber [2].
AM 1.5G	A standardized global horizontal irradiance spectrum generally used for terrestrial solar cell research to measure the performance of solar cells under sunlight [3].
Bifaciality (factor)	The ratio of the rear side efficiency to the front side efficiency, often expressed as a percentage, stating to what degree a solar module is “bifacial” [4].
Bifacial PV system	A solar photovoltaic system manufactured to convert sunlight to electricity on the front and back of the PV modules [5].
Blackbody	A theoretical object in thermal equilibrium that absorbs all electromagnetic radiation incident upon it [6].
Diffuse solar radiation	Solar radiation that is absorbed, scattered, or reflected by an atmospheric constituent [7].
Direct solar radiation	Solar radiation intercepted uninterrupted in a direct line from the sun [7].
Global solar radiation	The sum of direct and diffuse solar radiation [7].
Linke turbidity factor	Measures incident solar radiation’s atmospheric absorption and scattering under clear skies [8].
Reflected solar radiation	Solar radiation reflected by the earth's surface [9].

Reflection	The phenomenon of light incident on a surface being scattered backward [10].
Refraction	The bending or “turning out of their way” of light incident on an interface at some angle [10]
Scattering	The interaction of electromagnetic radiation with particles or large gas molecules, causing it to be diverted from its original path, redistributing the energy of the incident radiation [1].
Soiling losses	Energy production losses due to material accumulation on the solar cells’ light-collecting surface [11].
Solar altitude	The sun’s angle relative to the Earth’s horizon, measuring the sun’s height in degrees [12]. In general, the solar altitude is highest at solar noon and lowest at sunrise and sunset.
Solar insolation	The solar energy incident in a given area over a specified time [13].
Solar irradiance	The solar power that reaches a surface per unit area (surface power density), typically measured in W/m^2 [14].
Solar irradiation	The sum of solar energy incident on a surface over a specific period per unit area, typically measured in kWh/m^2 [14].
Solar noon	The time when the sun reaches its highest point in the sky [15].
The angle of incidence	The angle at which a line (incident sunlight, for example) strikes a surface relative to the normal drawn at the point of incidence [16].

1 Introduction

The increasing global energy demand and the imperative to address climate change have sparked a search for sustainable and environmentally-friendly energy sources. Solar energy presents a compelling solution as the cleanest and most abundant resource available [17], taking advantage of the sun's vast energy resource. The amount of energy that reaches Earth from the sun in an hour exceeds the total global energy consumption in a year [18]. Among the various methods of solar energy harvesting, solar photovoltaic technology stands out as the most widely employed for electricity production, directly capturing solar radiation and converting it into electricity. Thus, it presents a versatile and adaptable energy source we can deploy on buildings, rooftops, open spaces, or building materials.

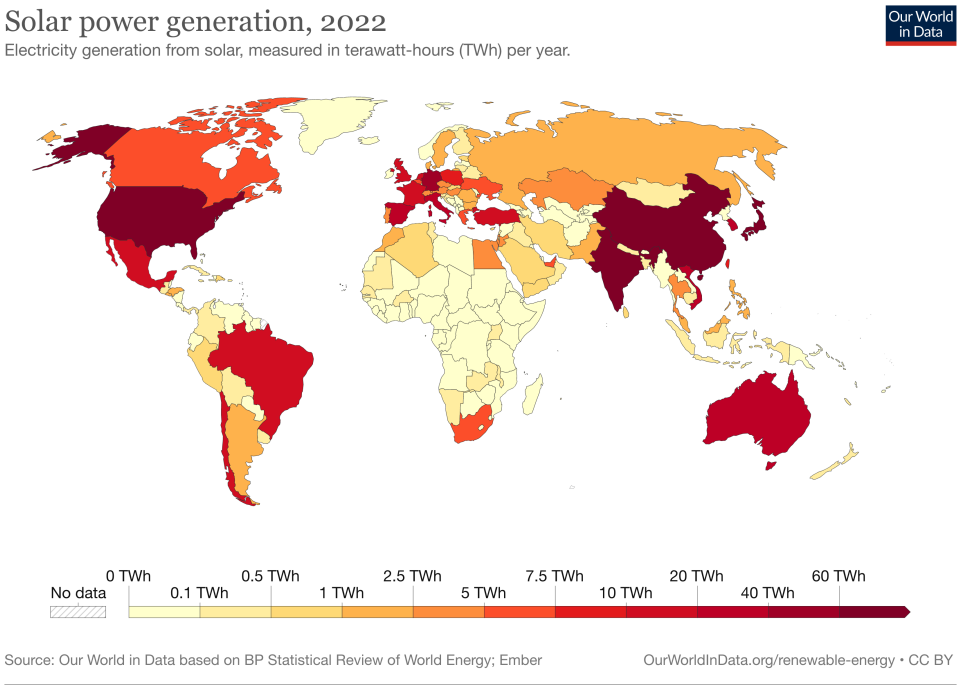

Fig. 1. Solar Power generation by country in 2022 [19]. CC BY 4.0.

Solar photovoltaic technology is rapidly becoming widely used globally, and projections indicate that by 2027, we expect it to surpass hydropower, natural gas, and coal as the most extensive installed electricity capacity worldwide [20]. However, the current worldwide installed solar photovoltaic capacity primarily concentrates in countries at lower latitudes where solar resources are abundant. China, the United States, Japan, Germany, India, and Italy had the highest installed capacities worldwide in 2021 [19]. Due to the perception of limited solar resources and harsh climates, researchers often overlook higher-latitude regions

for solar photovoltaic research and deployment. These regions cover a large area where the energy demands are substantial. It would be crucial to unlock the potential of solar photovoltaic technology in these regions to reduce the dependence on fossil fuels and contribute to energy independence on a mission to achieve a sustainable energy future.

Despite the vast potential and positive effects of solar photovoltaic deployment in high-latitude regions, there remains a significant gap in research on the performance and viability of different solar photovoltaic technologies in such environments. The potential of the technology in these regions has received increased attention in previous years, and researchers have worked to understand the effects of the harsh environment. However, we still need to address challenges for the technology whose effects on energy production require a more comprehensive understanding. The limited research hinders the widespread use of solar photovoltaic systems in these regions, slowing global progress toward achieving renewable energy goals.

By addressing the challenges of solar photovoltaic systems in these regions, we can suggest improvements to existing technologies or develop new ones specifically designed to operate effectively in these demanding environments. To identify improvements while adapting solar photovoltaic technology to new deployments, performing field-testing of new technologies is essential.

1.1 Objective of thesis

In this thesis, we seek to fill this research gap by evaluating the performance of Over Easy Solar AS's prototype solar photovoltaic system, specifically designed to excel in high-latitude conditions. With this purpose, we conduct a comparative analysis with a system consisting of a dominating technology on the market. We seek to assess the feasibility of the systems and aim to identify the strengths and weaknesses of each technology in the environmental conditions of high-latitude regions. Furthermore, we will provide insights into important factors that influence the performance of solar photovoltaic systems in high-latitude areas, such as the variability of solar radiation, low temperatures, and environmental conditions such as cloud cover and snow.

The research in this thesis should expand our understanding of solar photovoltaic performances in high-latitude regions and provide valuable insights to energy planners, policymakers, and stakeholders in the renewable energy sector. By shedding light on how the harsh climate affects the energy production of various technologies, our aim is that our findings can shape the future implementation of solar photovoltaic systems in the regions.

This thesis builds on the research paper "*Literature review of the use and performance of monofacial and bifacial solar modules in high latitude regions* [21]," written in the Fall of 2022. Without additional citation, we incorporate theory, findings, and insights from that research paper into this thesis.

1.2 Structure of thesis

Chapter 2 presents the fundamentals of solar energy harvesting through solar photovoltaics. First, we look at the properties of solar radiation and the interactions of light with matter in the atmosphere. Subsequently, we delve into the technical aspects of solar energy harvesting, including solar photovoltaic technology, the solar cell manufacturing process, and the components of solar photovoltaic systems. Moreover, we investigate factors that influence the energy performance of solar photovoltaic systems in Tromsø and introduce metrics to analyze energy performance. Finally, we present the PVSyst software, which we use to estimate both available solar energy and expected system performances.

Chapter 3 initiates the methodology, which presents the two solar photovoltaic systems we will analyze for their performance.

Chapter 4 is also part of the methodology and presents the simulation software and data of the thesis. We include an introduction to performing simulations in PVSyst and the simulation setups of each of the systems. Furthermore, we provide an overview of the data and the data collection and analysis methods. Lastly, we explain expected system performance variations.

Chapter 5 covers the limitations and uncertainty of the research.

Chapter 6 presents the results of the thesis.

Chapter 7 covers the discussion.

Chapter 8 contains the conclusion.

Chapter 9 proposes suggestions for future work expanding or improving the research.

Chapter 10 contains the bibliography.

2 Theoretical background

2.1 Solar radiation

2.1.1 Properties of solar radiation

We start by investigating the properties of solar radiation, which is the energy source of solar photovoltaic systems. The sun continuously emits solar radiation, which consists of electromagnetic waves. We understand electromagnetic waves in quantum mechanics as waves and particles, behaving like waves when traveling through space, but during emission and absorption, they also exhibit particle-like behavior [10]. When it comes to harvesting solar energy, our primary interest lies in the particle-like nature of the interaction between solar radiation and matter.

Electromagnetic waves consist of a flux of *photons* – quanta of the electromagnetic field, and the energy of a photon is given by:

$$E_{ph}(\lambda) = hf = \frac{hc}{\lambda} \tag{2.1}$$

Here, h is Planck's constant, and f is the electromagnetic wave frequency. In the extension of the equation, we use the relation:

$$f = \frac{c}{\lambda} \tag{2.2}$$

Photons serve as the fundamental energy source of solar photovoltaic systems, and we use the relation to quantify the energy of a photon using the speed of light in a vacuum (c) and the wavelength of the electromagnetic wave (λ). These equations establish that photons have a discrete amount of energy determined by their wavelength or frequency. Because of the importance of photons in our study, we look further into the various characteristics of photons.

We call the range of all types of electromagnetic waves, characterized by wavelength or frequency, the *electromagnetic spectrum* [22]. We illustrate the spectrum in Fig. 2. The

position of photons on the electromagnetic spectrum depends on their discrete energy. Photons with shorter wavelengths or higher frequencies have more energy than photons with longer wavelengths and lower frequencies. The radiation types in the electromagnetic spectrum consist of photons with energies within a specific range of wavelengths (or frequencies). The wavelengths determine their properties and how they interact with matter, making them suitable for different applications. Regarding solar radiation, the sun emits a wide range of wavelengths and frequencies, forming the solar spectrum together.

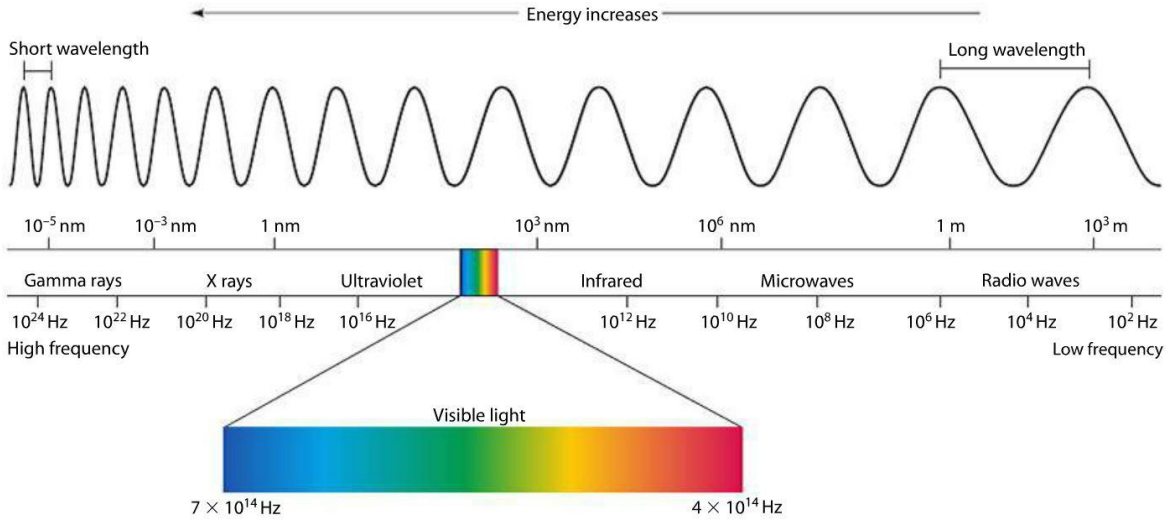

Fig. 2. The electromagnetic spectrum [23].

Fig. 3 illustrates the extraterrestrial solar spectrum, which shows how energy is distributed across all wavelengths as the solar radiation reaches the top of the atmosphere. We focus on understanding the spectrum because it lets us determine the available solar energy for power generation. The distribution of energy defines its shape and intensity. We divide the spectrum into three main regions: ultraviolet (UV), visible, and infrared (IR), with photon energies corresponding to 3-5 eV, 1.8-3 eV, and 0.5-1.8 eV, respectively [6]. Most extraterrestrial solar energy concentrates in the approximated 300-1100 nm range, corresponding to 1.1-4.1 eV photon energies. The peak energy is in the visible and near-infrared parts of the electromagnetic spectrum.

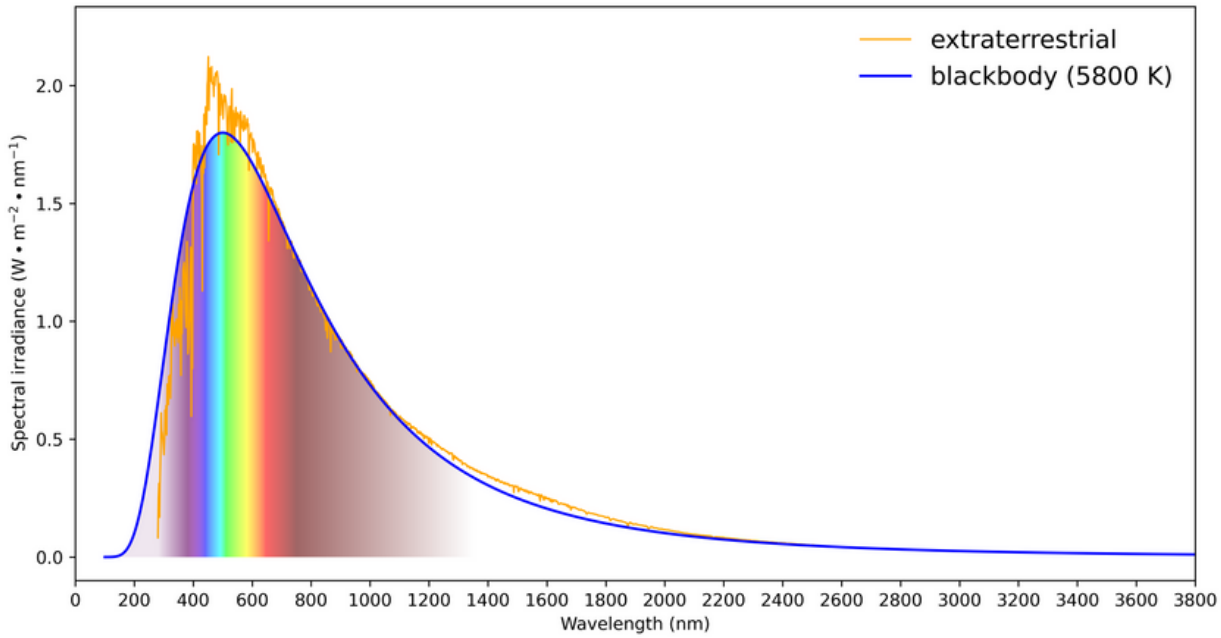

Fig. 3. The extraterrestrial solar spectrum compared to the ideal blackbody spectrum with temperature 5800K [6].

We assume that the solar radiation reaching Earth remains constant, despite its temporal variation caused by the 11-year cycles in solar activity. The constant value is called the *solar constant* and includes radiation across the entire electromagnetic spectrum. An average from decades of extraterrestrial measurements performed by satellites has derived the solar constant, and it serves as a measure of solar irradiance before it enters the atmosphere. We typically represent it as:

$$S = 1367\ Wm^{-2} \tag{2.3}$$

Extraterrestrial solar radiation is the energy we wish to harvest. We must explore the crucial interactions between solar radiation and the atmosphere to determine the solar radiation that reaches the solar cells in Tromsø.

2.1.2 Interaction of solar radiation with matter

The atmosphere plays a huge role in the differences between extraterrestrial solar radiation and the radiation that eventually reaches our solar cells on the ground. As solar radiation propagates through the atmosphere, atmospheric constituents such as particles and gases

redistribute parts of its energy through *scattering* and *absorption* [24]. These atmospheric effects reduce the intensity of solar radiation and change its spectral composition. Fig. 4 illustrates the differences between the extraterrestrial and terrestrial solar spectrums. Ozone (O_3) blocks electromagnetic radiation with wavelengths shorter than 300 nm from reaching the surface. On the other hand, water vapor (H_2O) and carbon dioxide (CO_2) mostly absorb electromagnetic radiation in the infrared part of the spectrum. We observe that photons with particular wavelengths (or energies) are absorbed to a greater extent than others, reducing the intensity of solar radiation at specific wavelengths, which we identify as the absorption bands in Fig. 4.

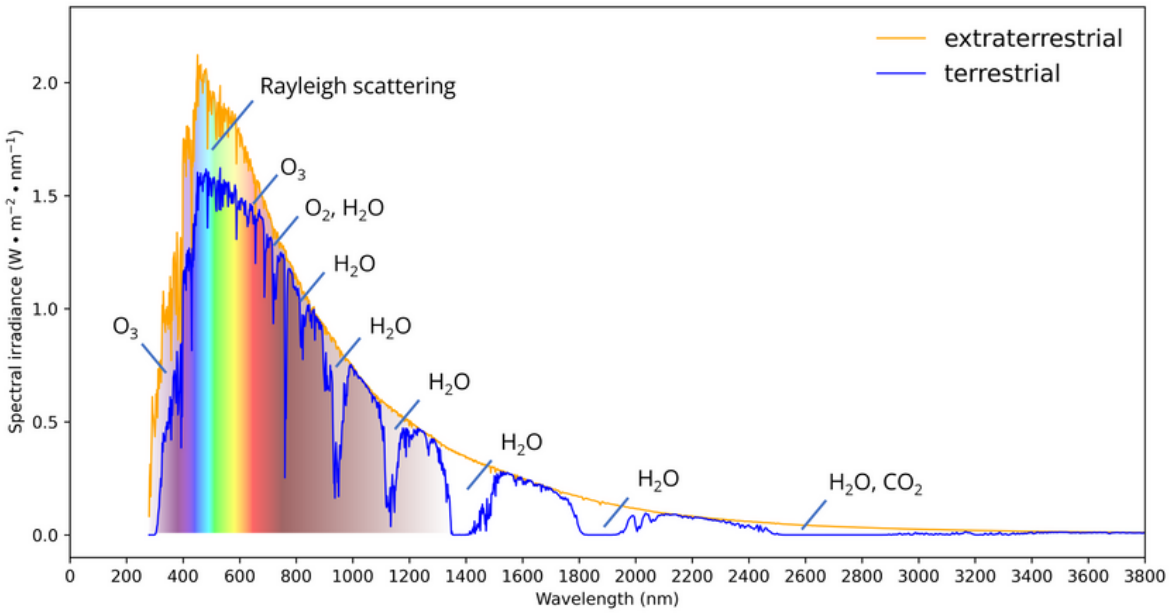

Fig. 4. The terrestrial and extraterrestrial solar spectrums compared [6].

The extent of scattering and absorption depends on several factors, including the energy of the incident electromagnetic radiation, the density of the particles or gas molecules in the atmosphere, and the distance the solar radiation travels through the atmosphere before reaching the surface [1]. Given Tromsø's high-latitude location, we focus on the path length, which we call *air* mass (AM). Air mass represents the distance solar radiation travels through the atmosphere, normalized to the shortest possible path. Fig. 5 illustrates this concept, with "X" as the shortest path and "Y" as the actual path. We calculate air mass using the zenith angle (θ) in the equation below.

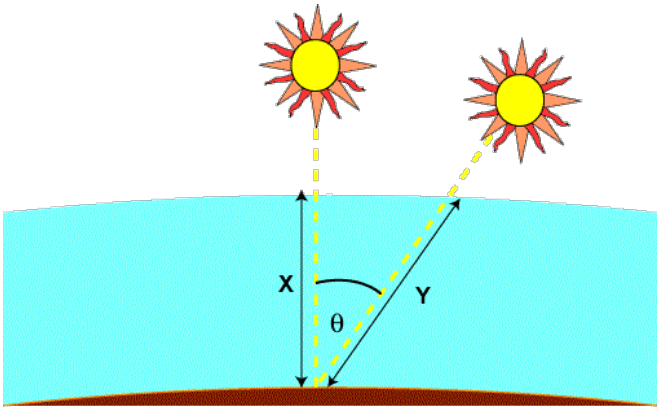

Fig. 5. Representation of air mass and the zenith angle θ [25].

$$AM = \frac{Y}{X} = \frac{1}{cos\,\theta} \tag{2.4}$$

Solar radiation takes its shortest path when the sun is directly overhead, where X=Y, resulting in an air mass of 1 (AM1). Beyond the atmosphere, we refer to the extraterrestrial solar spectrum as air mass 0 (AM0). As the air mass increases, the path length of solar radiation through the atmosphere becomes longer. Our study takes place in Tromsø, where the *solar altitude* reaches its maximum of around 44° during *solar noon* on the summer solstice, on June 21 [26]. A solar altitude of 44° corresponds to a zenith angle of 46° and an air mass of:

$$AM = \frac{1}{\cos(\theta)} = \frac{1}{\cos(46^\circ)} = 1.44 \tag{2.5}$$

This calculated value represents the minimum air mass at our location, which occurs when the sun is the highest, mid-summer. However, the solar altitude is much lower for most of the year, leading to significantly higher air masses. An increased air mass causes the atmospheric constituents to scatter and absorb more incoming solar radiation, reducing solar irradiance at the surface. Therefore, we assume that the high air mass at our research location leads to a considerable decrease in available solar radiation compared to extraterrestrial values. Moreover, as the energetic photons in the electromagnetic radiation propagate toward our solar cells, weather conditions further alter the scattering and absorption effects. We need to investigate these effects.

Generally, we assume that any obstacle between the sun and the surface reduces the amount of solar radiation reaching the solar cells. For example, increased atmospheric aerosols and increased humidity increase the extent of scattering and absorption. However, our main focus lies on clouds and snow, two highly influential factors for solar photovoltaic systems.

Clouds in the atmosphere scatter and reflect incoming solar radiation due to their composition and high albedo. As a general assumption, an increase in cloud cover leads to reduced absorption of solar energy on the surface. On average, clouds reflect approximately 20% of the incoming solar radiation, but the albedo can vary among different cloud types [27]. High cirrus clouds exhibit albedo values ranging from 0.1 to 0.3, while cumulonimbus clouds have albedo values ranging from 0.7 to 0.9 [28]. Thicker clouds tend to block a more significant amount of radiation. Therefore, the local cloud cover in Tromsø could significantly affect the available solar radiation for solar photovoltaic systems.

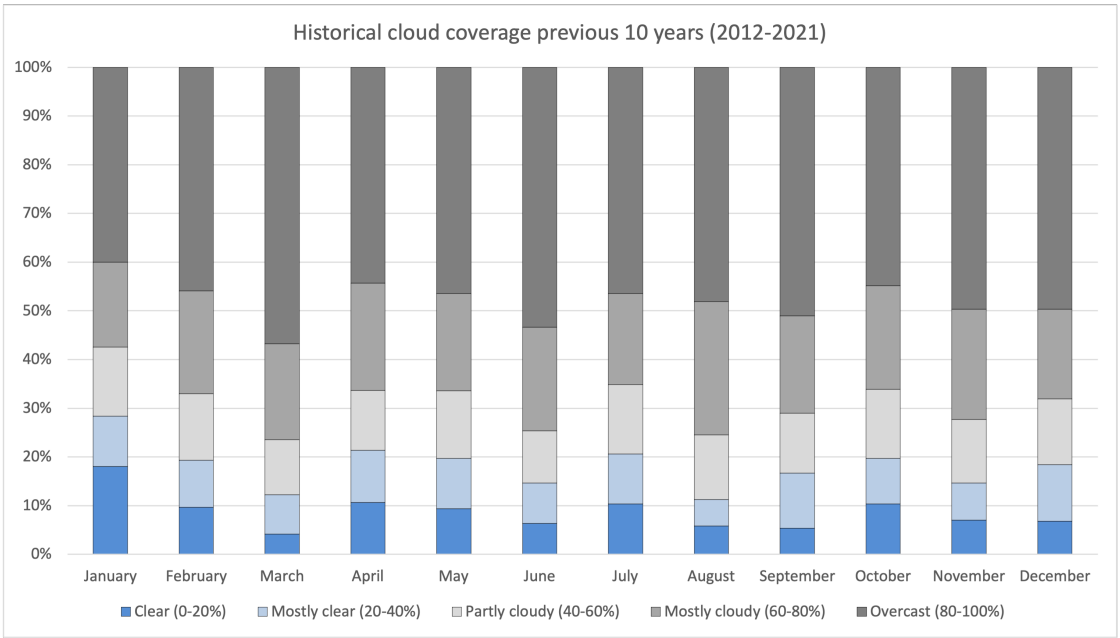

Fig. 6. Historically averaged distribution cloud cover for each month over the past ten years. Data source: https://seklima.met.no/observations/.

Fig. 6 shows the average cloud cover observed in Tromsø over the past ten years. The data suggests that January has the highest probability of clear skies. Conversely, March and August have the lowest chance of clear skies, with barely over 10% of days being clear or mostly clear and approximately 75% being mostly cloudy or overcast. Generally, except for January, more than 60% of days in each month experience mostly cloudy or overcast weather.

As a result, we expect that cloud cover will significantly reduce the amount of available solar radiation for our solar cells. Furthermore, we often associate clouds with precipitation, which we will look into next.

The expected precipitation form depends on the surface temperature, and Fig. 7 illustrates the average daily temperatures in Tromsø over the previous ten years (represented by blue and red lines). Generally, we divide the year into three parts: a cold period with daily temperatures below zero degrees Celsius, a transition in early April when temperatures rise above zero degrees, and then a return to sub-zero temperatures in late November. Considering that a significant portion of the year experiences temperatures below zero degrees Celsius, we anticipate parts of the precipitation to occur in the form of snow.

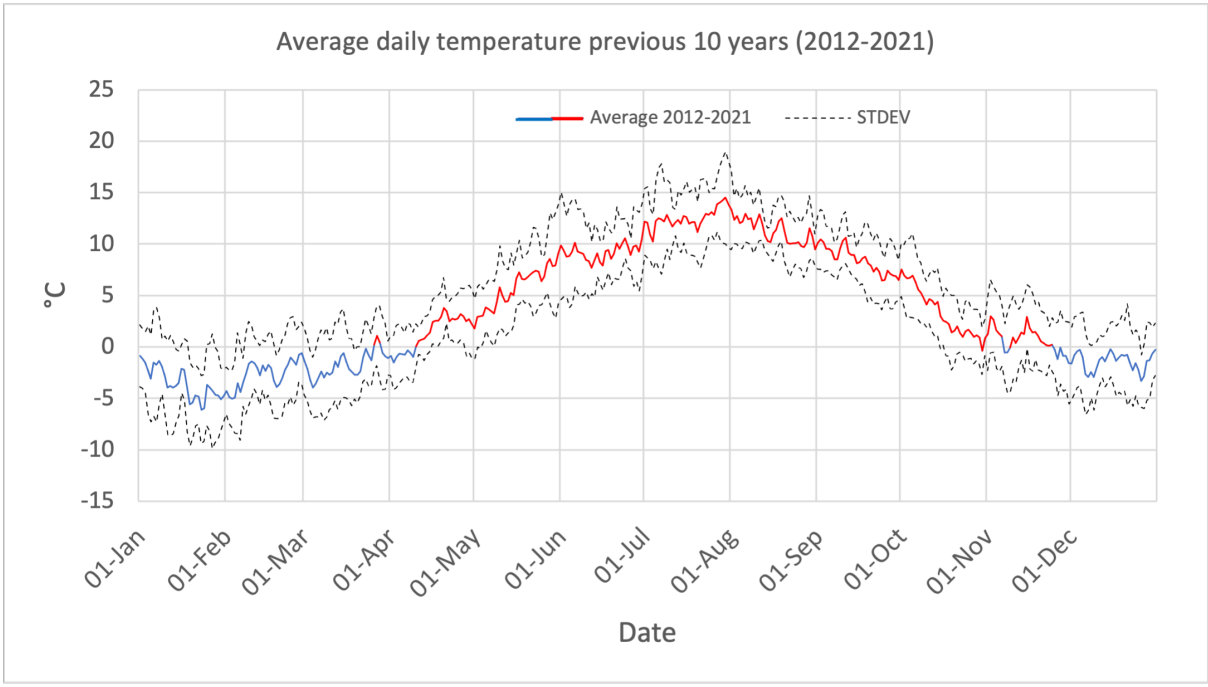

Fig. 7. Average daily temperature from the previous ten years (2012-2021)
Data source: https://seklima.met.no/observations/.

Snow appears optically white due to its high albedo across all wavelengths. As a result, snow effectively reflects incoming solar radiation. The precise value of the albedo of snow can vary over a year. Fresh snow typically has an albedo of 0.81 - 0.88, while older and melting snow has an albedo of 0.65 - 0.81, which is relatively high compared to other typical surfaces, such as asphalt (0.05 – 0.2), grass (0.25 – 0.3), or brick/stone (0.3 – 0.4) [29]. We illustrate the average depth of ground snow in Tromsø in the past decade in Fig. 8. Data shows snow

usually accumulates from the start of the year until it peaks around mid-April before decreasing to zero around June 1. After a break during the summer, snow accumulation resumes in late October, gradually increasing towards the end of the year. We expect the snow-covered ground to significantly decrease the solar radiation that effectively reaches the surface in Tromsø.

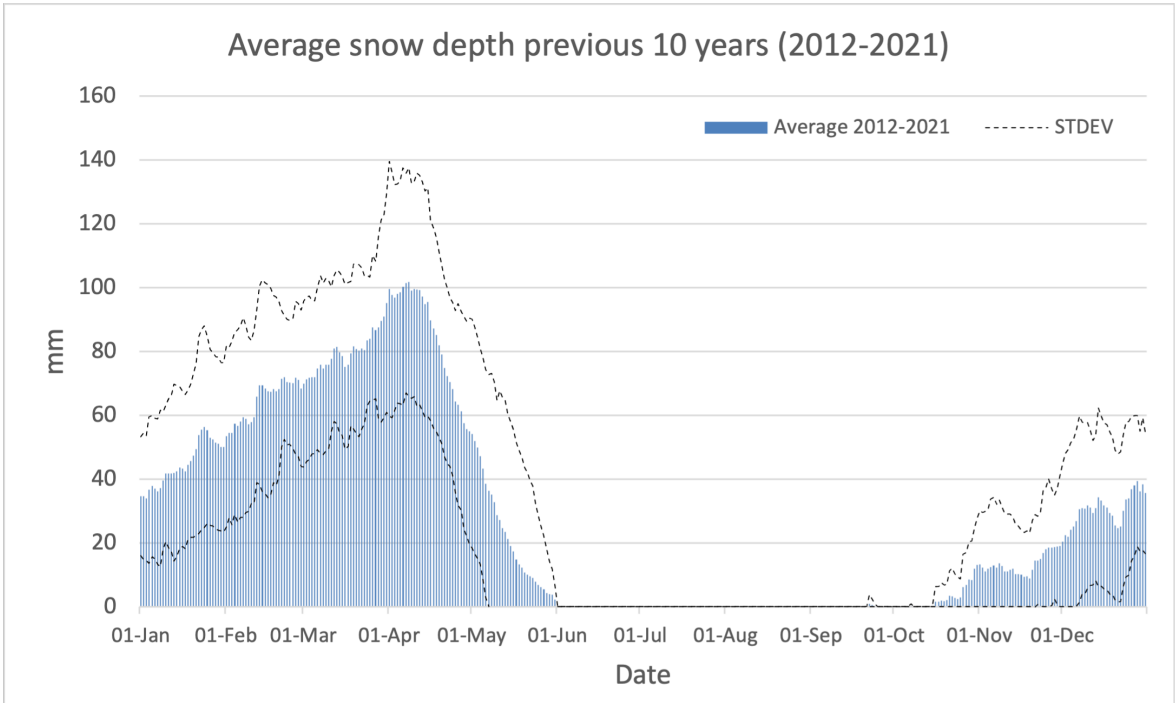

Fig. 8. Average snow depth in the previous ten years (2012-2021) in Tromsø, Norway. Data source: https://seklima.met.no/observations/

The mentioned atmospheric and ground interactions affect solar radiation on its way toward the surface, and it is natural to examine how much solar radiation reaches the ground.

2.1.3 Actual and standardized surface solar radiation

Absorption, scattering, and reflection lead to different components of solar radiation reaching the surface. We illustrate the components in Fig. 9. The quantity of each component of the solar radiation that reaches the ground is essential for solar photovoltaic systems.

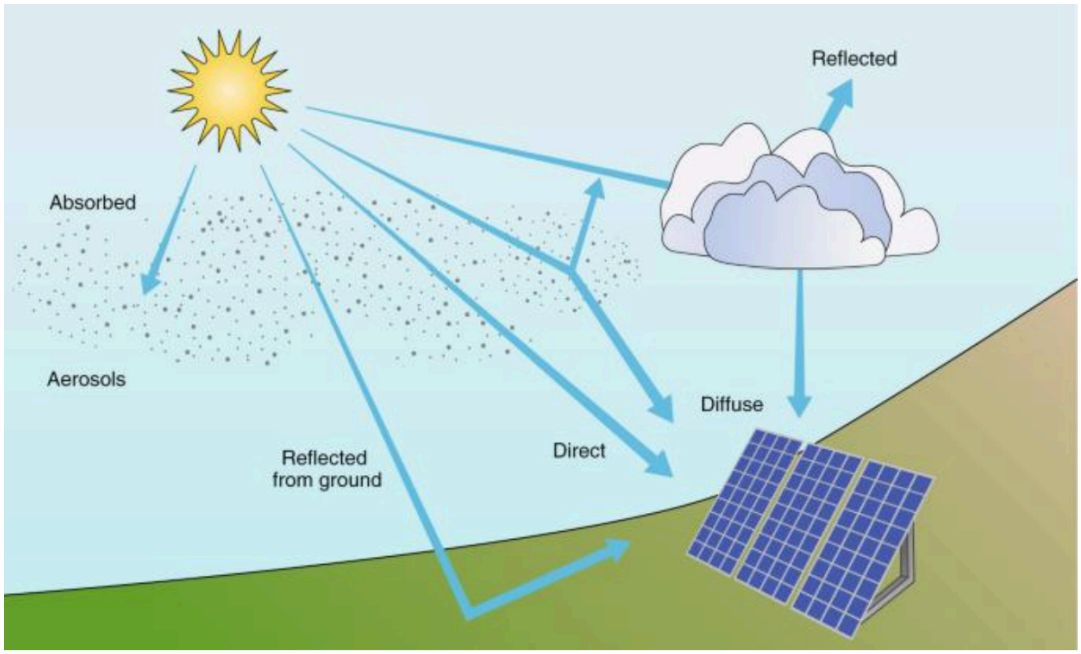

Fig. 9. The components of solar radiation [30].

On clear days, solar radiation includes *direct, diffuse*, and *reflected radiation*, with direct radiation being the main component. Atmospheric effects can reduce direct radiation by around 10% on clear days but up to 100% on days with thick clouds [7]. Consequently, cloudy days have significantly reduced direct radiation, leading to an increase in diffuse radiation. Therefore, we also expect reflected sunlight to be lower on cloudy days. Direct radiation is more energetic than scattered diffuse radiation, so the availability of solar radiation for power generation is considerably higher on clear days than on cloudy days. Given the typically cloudy weather conditions in Tromsø, we expect a significant reduction in the available solar radiation for power generation. We need to look at the climate in the region to understand what to expect in Tromsø over time.

We use the Köppen-Geiger-Photovoltaic (KGPV) climate classification, classifying regions based on climate and environmental factors relevant to the solar photovoltaic systems [31]. The KGPV classification divides the globe into twelve zones, sorted by temperature, precipitation, and irradiation. The twelve most relevant climate zones take form by combining TP-zones and I-zones, shown in Fig. 10 and Fig. 11, where the letters indicate temperature-precipitation and irradiation zones, respectively.

Our focus is on Tromsø, and the classification places the city in the EL (cold climate with low irradiation) climate zone, which is unfavorable for large-scale solar photovoltaic installations. The EL climate zone implies a cold climate with frequent snowfall, long winters, and a low amount of solar irradiation that reaches the surface due to a high air mass and the high reflectivity of a snow-covered surface. Tromsø is in the 30th percentile of locations receiving the lowest solar irradiation. Based on this classification, it is not considered an ideal installation location. However, we will need more specific numbers to describe the available resource at our location accurately.

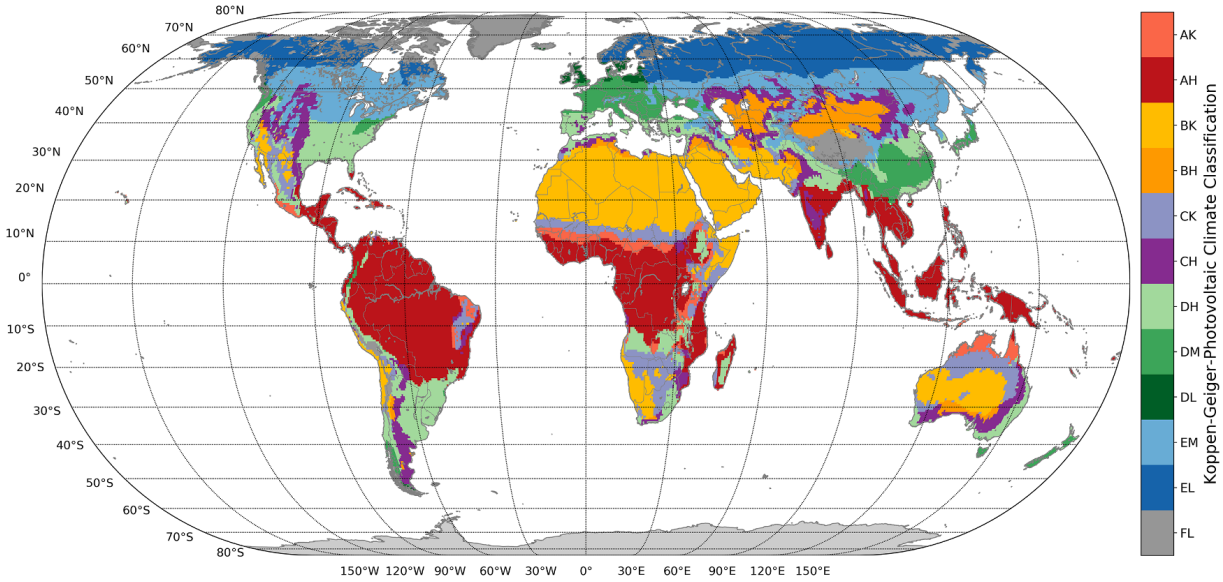

Fig. 10. The twelve most relevant climate zones in the KGPV climate classification with color coding on the right [31].

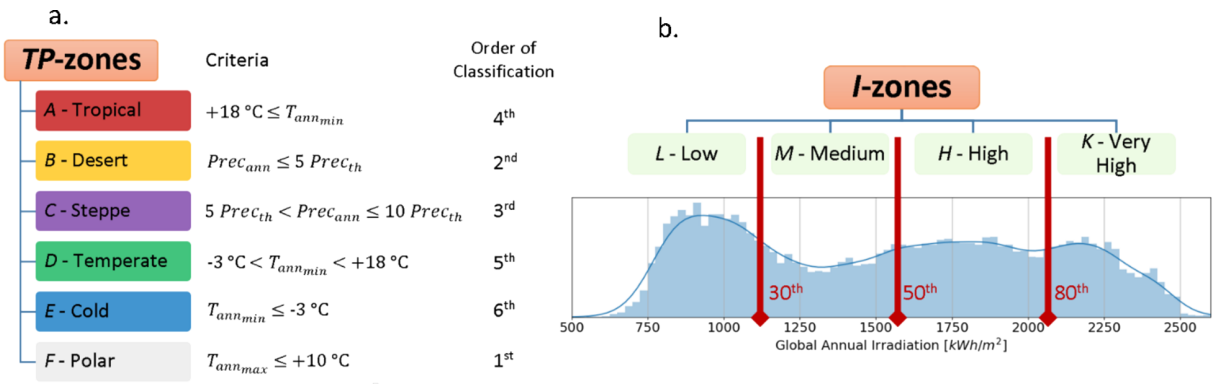

Fig. 11. Thresholds for the zones in a KGPV climate classification [31].

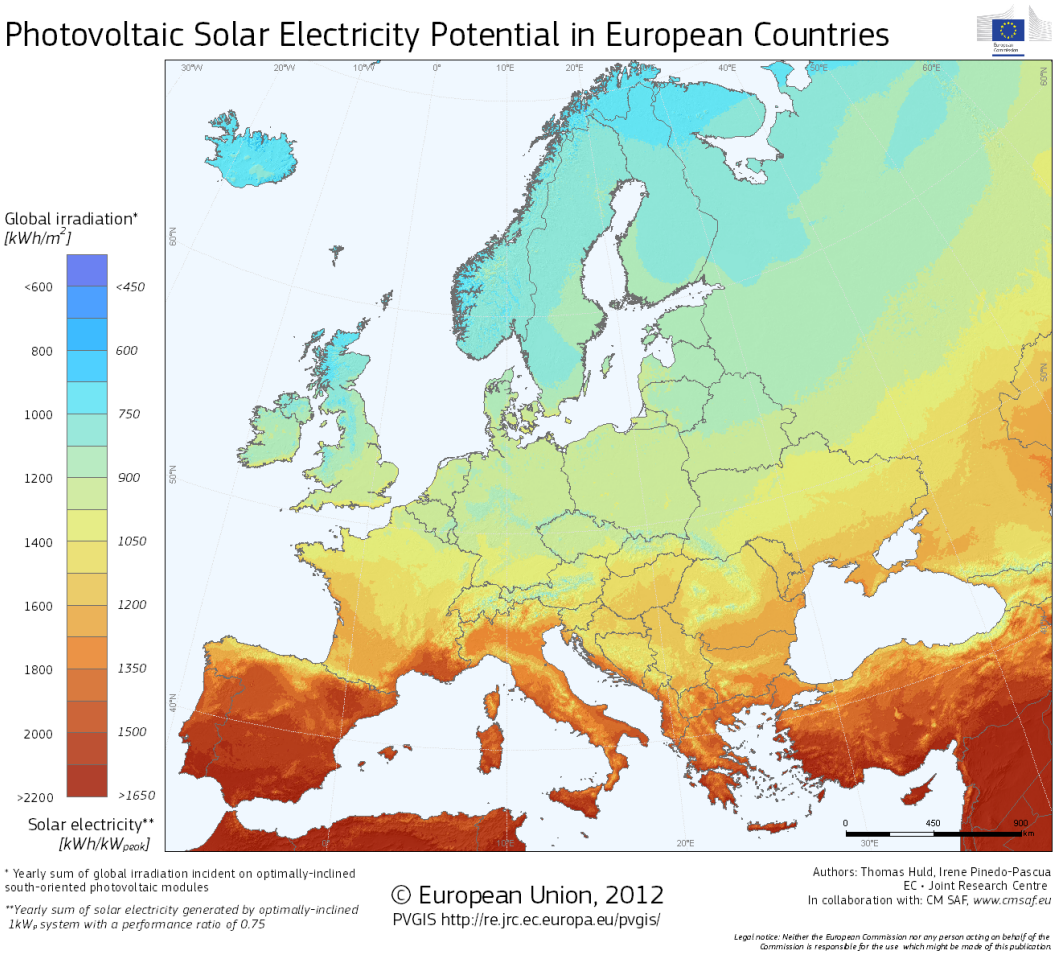

Fig. 12. Global irradiation values in Europe [32].

Fig. 12 estimates Europe's global irradiation values on an optimally inclined surface, where the differences in Europe are vast. Fig. 13 directs the focus on Norway and shows that Tromsø has an expected yearly sum of global horizontal irradiation in a range we estimate as 700-750 kWh/m^2. This value is low compared to Spain and Italy, two of the three European countries with the highest solar power generation in 2022 [19]. However, the European country with the highest solar power generation is Germany, whose global horizontal irradiation we estimate at 1000-1200 kWh/m^2 [33]. When we compare the global horizontal irradiation of Germany and Tromsø, the differences are not that vast.

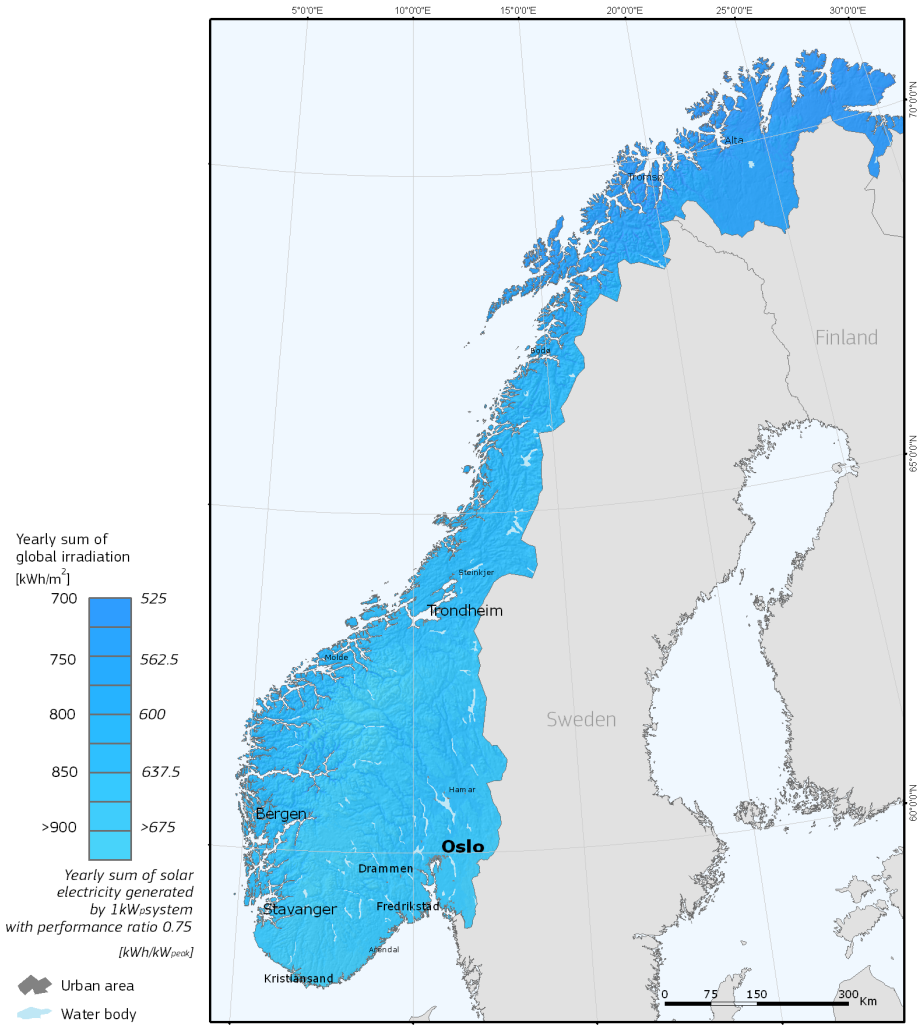

Fig. 13. Global horizontal irradiation values in Norway [32].

Solar irradiance is another measure of solar radiation on the surface and varies globally. At solar noon in the summer, the solar irradiance can vary from around 1000 Wm^{-2} at the equator to 500-600 Wm^{-2} in high-latitude regions [34]. We find that the atmospheric effects reduce the intensity of solar radiation significantly on its path through the atmosphere. Fig. 14 shows the global variations. However, it shows the global average annual solar irradiance, which includes nights and cloud coverage, based on three-year measurements. The black dots indicate areas where the potential for solar power is sufficient to meet the global energy demand as of 2006 [35].

We are particularly interested in the global average solar irradiance in Tromsø, which we estimate is 50-100 W/m^2. Similar to the global horizontal irradiation, the global average solar irradiance in Tromsø is significantly lower than in Spain and Italy, but compared to Germany, the values are more similar. The significant global variations make comparisons of

technologies and measurements made in different countries difficult, resulting in a need for a standardized value for solar irradiance.

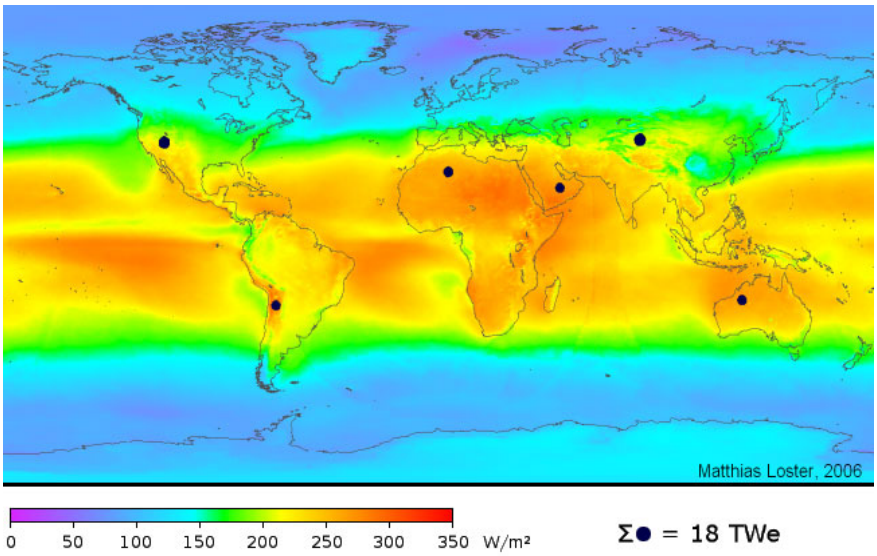

Fig. 14. Global average annual solar irradiance, measured in W/m² [35].

The problem related to the variable solar irradiance has led researchers to create a standardized solar spectrum called AM1.5G, which corresponds to a zenith angle of 48.2°, including direct and diffuse solar radiation. The AM1.5G spectrum represents the terrestrial spectrum in Fig. 4. We approximate the AM1.5G spectrum by reducing the extraterrestrial spectrum by specific percentages, accounting for the atmospheric effects [25]. The calculations give an irradiance of 970 Wm^{-2} for AM1.5G, normalized to 1000 Wm^{-2} for simplicity.

This standardized solar spectrum and a solar cell temperature of 25°C are conditions widely accepted as an industry standard for testing and performance evaluations of solar cells. These conditions are named *Standard Testing Conditions (STC)*. The STC is significant in this study because researchers have determined the ratings of the solar cells in our research under STC, and we will get back to them when we present the systems.

Solar photovoltaic systems can collect the energetic photons that eventually reach the surface, and we must examine how these systems can convert photon energies to usable electricity.

2.2 Solar photovoltaics

2.2.1 The photovoltaic effect, semiconductors, and solar cells

We first introduce the photovoltaic effect, the principle of solar cells, and why we can collect photons from the sun to produce electricity. The *photovoltaic effect* generates an electrical current or voltage when exposing a material to electromagnetic radiation, such as solar radiation [36]. Solar photovoltaics utilize the photovoltaic effect, and we define the term as converting solar energy directly into electricity using solar cells [37]. For this purpose, solar photovoltaic technologies utilize a specific type of material called a semiconductor.

Semiconductors are materials placed between conductors and insulators in conductivity [38]. With this property, they can conduct electricity, but not as easily as conductors. We can alter or control their electrical conductivity by varying the temperature, illumination, and chemical structure or introducing *dopants*, which we will explain shortly [39]. Due to this property, they help control the flow of electricity. Both solar photovoltaic systems in Tromsø use silicon, which is by far the most used semiconductor in the solar cell market [40].

The silicon atoms uniformly bond in a periodic crystal lattice structure, where each atom connects to eight electrons with four covalent bonds [41]. Each electron has two distinct energy states: either in a low energy state (valence band) in the covalent bonds or a high energy state (conduction band) [42]. In the conduction band, they are free to move in the structure and participate in conduction. In semiconductors, the electrons must obtain energy to reach the conduction band. The required energy is a distinct property of a semiconductor called the *band gap* [43]. Electrons can obtain this energy in more ways, but we will focus on how energetic photons in electromagnetic radiation transfer their energy to the atoms in the semiconductor.

Exposing semiconductors to electromagnetic radiation can excite electrons into the valence band [42]. Suppose a photon in solar radiation with energy that equals the band gap of the semiconductor excites an electron. The excited electron and its corresponding hole in the structure are called light-generated carriers or free carriers and can contribute to electrical conductivity. However, for the semiconductor to effectively conduct electricity, it needs a sufficient number of free carriers. If too few are present, the excited electron will quickly lose

energy and return to its original state in recombination. In this process, the electron recombines with a hole in the structure, thus releasing excess energy as electromagnetic radiation or heat. We need to increase the number of free carriers to avoid losing the energy of the incident photon, and for this purpose, we introduce the concept of doping.

Doping refers to introducing other atoms – impurities – into the crystal lattice structure, and we want to focus directly on the silicon crystal lattice structure using information from PVEducation [44]. Suppose we add a controlled number of atoms with one more or one less electron than silicon in their valence band, typically phosphorous or boron, respectively, to the silicon structure. In that case, we have excess electrons or holes, free carriers, in the crystal lattice structure, resulting in n-type or p-type silicon, respectively. The excess free carriers can contribute to conducting electricity. Therefore, doped silicon has an increased conductivity. However, light-generated carriers will eventually recombine and release their excess energy unless collected, leading us to p-n junctions.

According to PVEducation [45], when n-type silicon comes into contact with p-type silicon, excess electrons from the n-side diffuse to the p-side, and excess holes from the p-side diffuse in the opposite direction. The result is a region near the interface where the dopant atoms' fixed charges are exposed, and no free carriers exist. An electric field is formed in the region known as the depletion layer, quickly sweeping away free carriers. The electric field establishes a built-in potential difference between the two sides, and this potential is what gives semiconductors their valuable properties to solar cells. The composition of n-type and p-type silicon results in a p-n junction, and Fig. 15 illustrates the process. Without external input, the p-n junction is in equilibrium with no net current. We will next explore how creating a p-n junction affects the absorption of energetic photons from the sun.

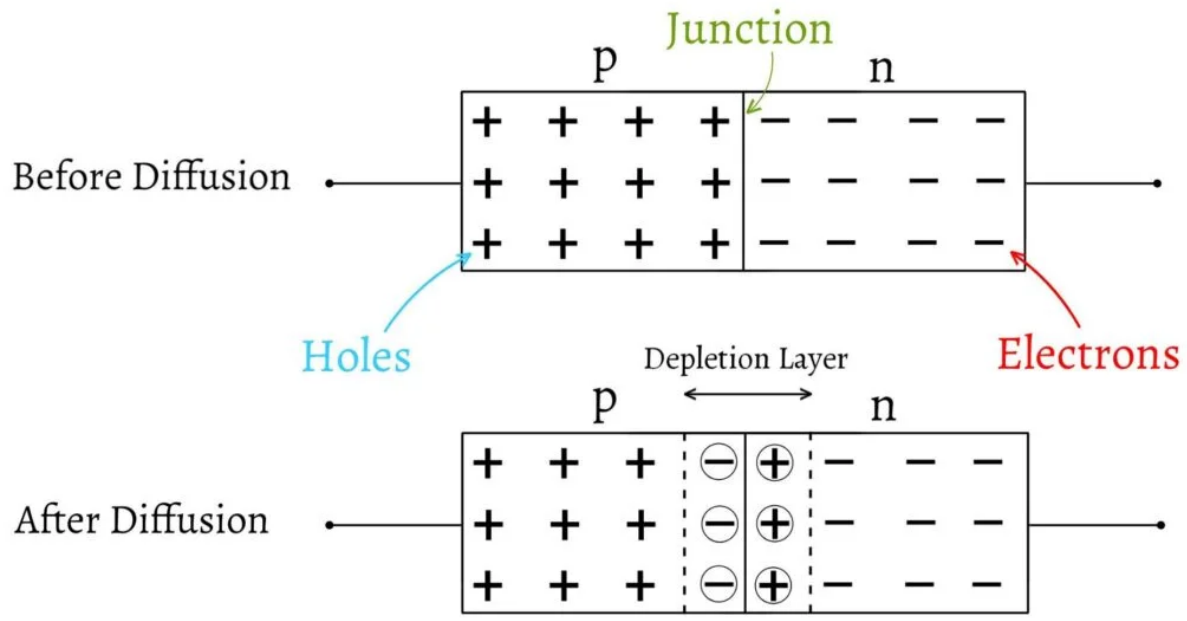

Fig. 15. The formation of a p-n junction [46].

When electromagnetic radiation with sufficient energy shines upon the p-n junction, it generates light-generated carriers. Instead of the excited electrons quickly losing their energies, which would result in their inability to contribute to the current or power generation, the electron-hole pair is separated. Due to the electric field in the p-n junction, electrons move to the n-side, and holes move to the p-side in a process called drift transport. The carriers in excess on each side of the junction are majority carriers, and those in the minority are minority carriers [44]. The light-generated minority carrier is swept across the junction to become a majority carrier. Now that the free carriers are separated to avoid recombination, there is a need for a way to extract the energy of the excited electron before it recombines.

As a simplified explanation, a solar cell introduces electrical contacts on the end of each side and an external circuit. The generated majority carrier flows through the external circuit and deposits its excess energy, corresponding to the potential difference between the sides, in the external load. It completes the circuit by meeting with its "partner" on the other side of the junction. We illustrate the components of typical monofacial and bifacial silicon solar cells in Fig. 16 and Fig. 17, respectively. Our research's ILP and OES systems utilize monofacial and bifacial solar cells. We introduce the concept of anti-reflective coatings in section 2.2.3.

The solar cell design allows energetic photons in solar radiation to transfer their energies to excite electrons within the p-n junction. The majority carriers then transfer their energy to an

external load, allowing us to extract the excess energy as electricity. However, not all photons can contribute to electricity production, which we will elaborate on next.

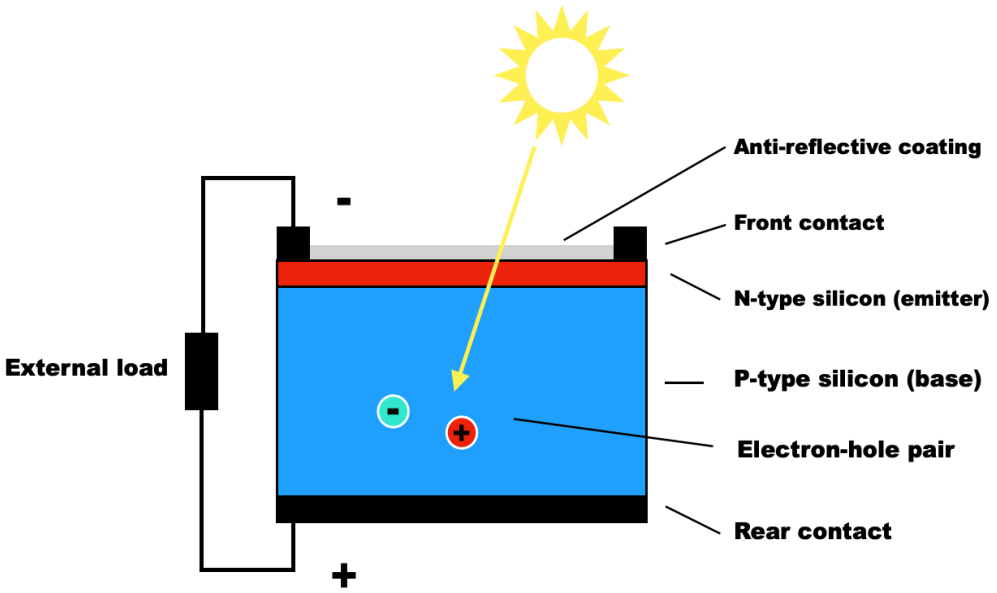

Fig. 16. Simplified cross-section of a typical monofacial silicon solar cell.

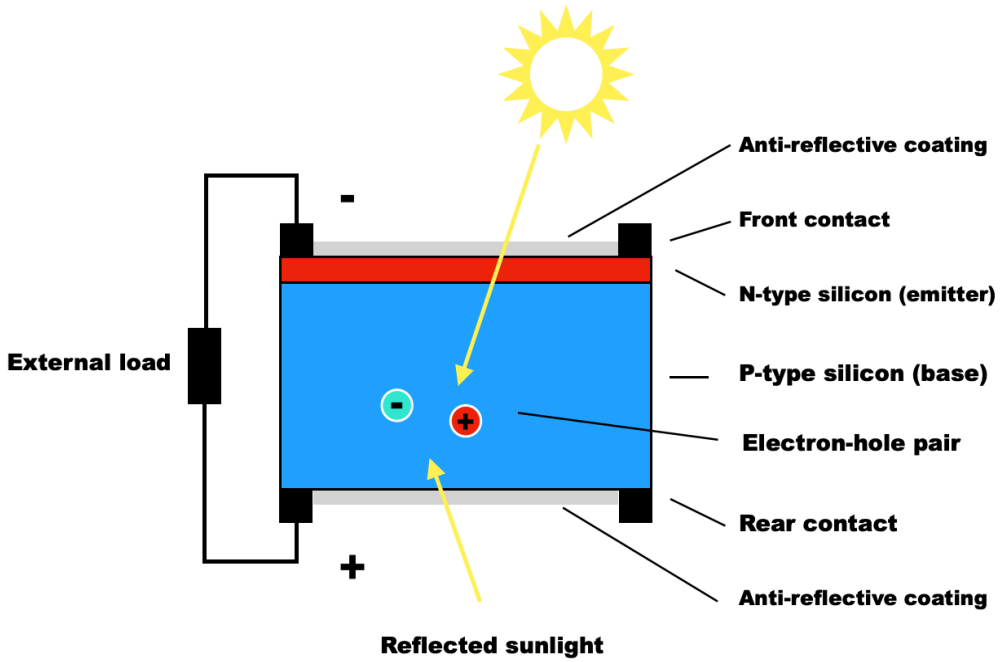

Fig. 17. Simplified cross-section of a typical bifacial silicon solar cell.

Photons reaching the surface of a solar cell undergo reflection, absorption, or transmission [47]. Reflected and transmitted photons do not contribute to electricity production and are thus considered losses. Photons with energy lower than the band gap of the semiconductor material have insufficient energies to create electron-hole pairs and are typically transmitted or reflected. On the other hand, photons with energy equal to or higher than the band gap can be absorbed, thus freeing electrons from their position in the structure. However, high-energy photons' excess energy (on top of the band gap energy) is wasted and does not contribute to electricity generation.

For silicon, the band gap is 1.12 eV, corresponding to photons with wavelengths of approximately 1100 nm. Silicon solar cells typically operate with wavelengths ranging from 1100 nm to 400 nm [48]. Photons with higher wavelengths than 1100 nm do not have sufficient energy to free an electron, while solar cells typically absorb photons with lower wavelengths than 400 nm near the surface, far from the p-n junction. In that case, the collection probability is low, meaning there is a low chance for the p-n junction to collect the electron-hole pair. Therefore, they cannot contribute to the light-generated current [49]. Fig. 18 demonstrates the part of the terrestrial solar spectrum that silicon solar cells effectively turn into electricity.

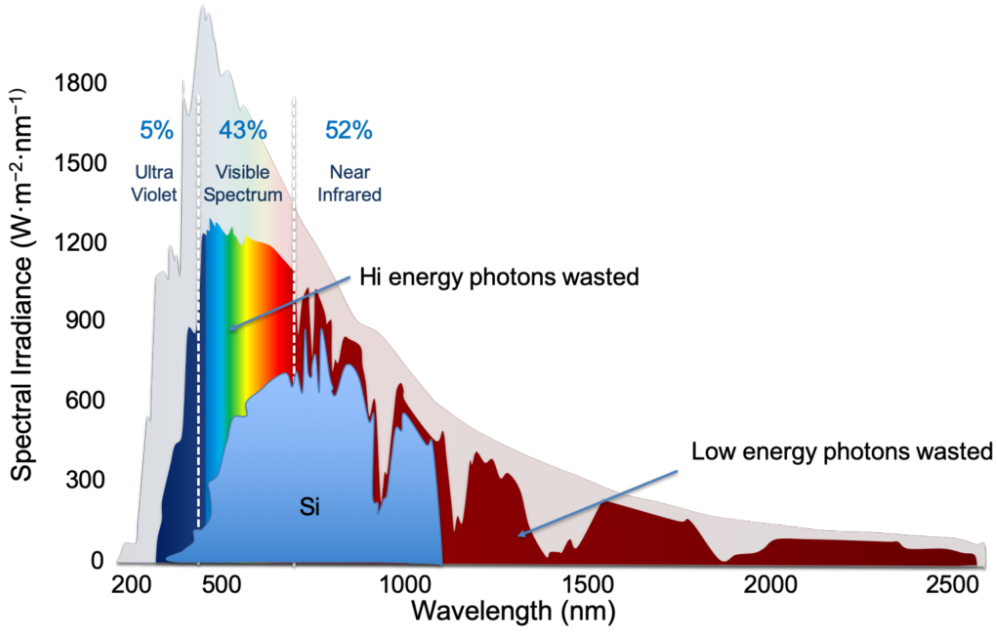

Fig. 18. The available solar radiation silicon solar cells turn into electricity [50].

Electron-hole pairs do not produce power alone. To generate power, we need both voltage and current. While the light-generated carriers give rise to current, the photovoltaic effect gives rise to voltage. The electric field in the p-n junction causes a voltage, representing an energy barrier for the carriers. The combination of light-generated current and the p-n junction voltage gives rise to power generation.

The energetic photon– the energy source of photovoltaic systems – thus travels from its starting point in the sun to the surface of a typical solar cell, exciting an electron and allowing us to produce electricity. We will now focus on the various solar cell technologies we can use.

2.2.2 Solar cell technologies

Both solar photovoltaic systems involved in this research use silicon solar cells, yet they have different technologies. The OES prototype solar photovoltaic system uses a combination of technologies, while the ILP system utilizes a first-generation technology. We want to look into the various technologies, with generations representing the stages of how the solar cell industry has evolved.

Crystalline silicon (c-Si) solar cells are the most dominant technology in the solar cell market [40]. We call them first-generation solar cells, and their popularity is partly due to the reasonable prices, the abundance of materials, and the maturity of the technology. Other advantages include durability and efficiency. We divide silicon solar cells into two subgroups: monocrystalline and poly/multi-crystalline. Monocrystalline cells use single silicon crystals, whereas poly/multi-crystalline cells have multiple crystals melted together. The ILP system uses polycrystalline solar cells. Monocrystalline cells are more expensive than polycrystalline ones but are also more efficient [51]. Fig. 16 illustrates the typical structure of first-generation solar cells.

Second-generation solar cells are thin-film (typically CdTe, CIGS, or GaAs) and amorphous silicon (a-Si) solar cells. They are made from fragile layers of semiconductor material deposited on a substrate such as glass, plastic, or metal foil, making them flexible and lightweight, which is ideal for specific installations [40]. Typical for these technologies is that they are low-cost compared to first-generation solar cells. The manufacturing also requires less energy and is easier to scale up for large installations. They are, however, less efficient than c-Si solar cells [51].

Third-generation solar cells are promising technologies that are yet to be fully commercialized. They use novel materials and designs to improve efficiencies or reduce costs. Out of the more developed technologies in this category, we find perovskite (thin film) solar cells, dye-sensitized solar cells, concentrated solar cells, nanocrystal-based solar cells (quantum dot, for example), and polymer-based (organic) solar cells [51]. These technologies offer benefits for various applications.

Over Easy Solar AS's prototype solar photovoltaic system uses heterojunction technology (HJT). The HJT technology combines c-Si and amorphous thin-film technologies, combining the best features of both technologies. Silicon HJT solar cells consist of thin amorphous silicon layers deposited on a c-Si wafer (typically n-type), and the a-Si layer acts as a passivation layer to reduce the recombination of light-generated carriers, particularly at the surface [52]. Surface recombination is an issue for c-Si solar cells, limiting their efficiencies. HJT cells improve this deficiency, and due to this property, the efficiency of an HJT cell is high compared to standard crystalline silicon cells [53]. We can design HJT cells for both monofacial and bifacial usage. When created as a bifacial module, they have an exceptionally high *bifaciality.*

There are many different technologies within the solar photovoltaic industry, and the two systems in this study utilize two different ones. We will briefly examine how the production method differs between these two technologies to improve our understanding.

2.2.3 Production of the solar cell technologies

The manufacturing process of a solar cell varies depending on the technology and the material used, but many of the main steps are the same. In our study, the material in focus is silicon, and the technologies are c-Si monofacial and HJT bifacial solar modules.

The first step for both technologies includes the purification of silicon. The manufacturers form pure silicon from silicon dioxide (silica, SiO_2), the most abundant material in the earth's crust and naturally found in quartzite gravel or crushed quartz [54]. For use in solar cells, they purify silicon to electronic-grade silicon (>99.9 % pure) through multiple chemical reactions. The method for growing a silicon ingot depends on the desired grain size of the crystals. Table I shows the terminology for the classification based on grain sizes. From here onwards, the manufacturing processes take different turns.

TABLE I

TERMINOLOGY FOR CRYSTALLINE SILICON [55]

Descriptor	**Symbol**	**Grain size**
Single crystal	sc-Si	> 10 cm
Multicrystalline	mc-Si	1 mm – 10 cm
Polycrystalline	pc-Si	1 μm – 1 mm
Microcrystalline	μc-Si	< 1 μm

We base this paragraph on information from MadeHow [56]. The first step of conventional c-Si solar cell production is that the manufacturer saws cooled silicon ingots into wafers and then polishes them to remove saw damage. Then, they add impurities and create a p-n junction by joining p-doped and n-doped silicon, typically doped with boron and phosphorous, respectively. Next, they texture the surface to ensure the refraction of incident electromagnetic radiation to maximize light absorption, and they further deposit a thin layer of metal on the wafer's surface to create an electrical connection. The metal contacts are etched to allow solar radiation to reach the p-n junction. They apply an *anti-reflection coating* (ARC) to the silicon wafer to minimize reflection losses and maximize light absorption. After that, the silicon wafers are encapsulated in a protective material, typically an ethylene vinyl acetate (EVA) film, to enhance durability and protect the cells from the environment. Next, they place the encapsulated solar cells in an aluminum frame with a glass cover and a Tedlar back sheet. Finally, the manufacturers test the solar cells to ensure they meet the performance and quality requirements.

The exact technology of the HJT solar cells in this research is unavailable because the Over Easy Solar AS system is a prototype. However, we utilize information from Solar Magazine [53] to describe the production process of a typical HJT solar cell. Still, the accurate method may vary depending on the specific design and manufacturer. Typically, first, the manufacturers slice the silicon ingots with a diamond-based saw into high-quality wafers before they clean and texturize them to increase light absorption. Next, they remove impurities in the wafer (typically n-type) with wet-chemical processing before deposing hydrogenated amorphous silicon (a-Si:H) layers on both sides of the wafer as passivation layers to reduce surface recombination. As a second part of the deposition process, they

deposit indium tin oxide (ITO) as a transparent conductive oxide (TCO) on both sides, acting as the front and rear contacts of the solar cell. They add metallization to the contacts to facilitate the flow of electricity. Next, they encapsulate the bifacial HJT solar cell in a protective layer to protect it from the environment. Fig. 19 illustrates a typical structure of an HJT solar cell.

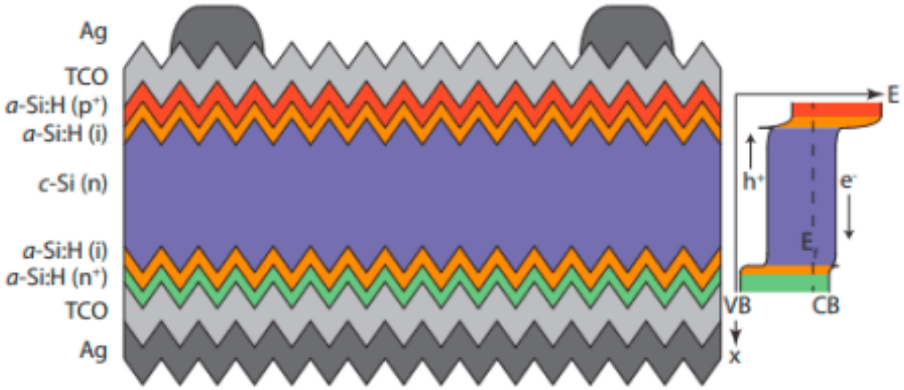

Fig. 19. Typical structure of a silicon HJT solar cell [52].

After briefly examining the main steps in the production methods for the two types of solar photovoltaic cell technologies, it is logical to explore how we can assemble an operational solar photovoltaic system. While the solar cell technologies are different, the system components are typically the same. The components are crucial for solar photovoltaics to be viable in Tromsø.

2.2.4 Solar photovoltaic system composition

A solar module comprises multiple solar cells electrically connected with wires [37]. Solar cells are thin and delicate, making them vulnerable to mechanical damage. Therefore, typical solar modules have protective measures such as an aluminum frame, protection glass, and an EVA film for transparent encapsulation [57]. Monofacial solar modules have a back sheet to protect the rear side, while bifacial modules require an additional layer of protection glass. These measures safeguard the modules from harsh environments and prevent water from penetrating them.

We connect solar cells in a module in series to increase power and voltage beyond what a single solar cell can provide [58, 59]. The voltage from each cell forms the total voltage when we connect them in series. However, the current in the string cannot exceed the current flowing through each cell, causing the total current in the string to equal the lowest current in a single cell. Therefore, the weakest cell in the string determines the total current. Suppose an object completely shades one cell in a string. In that case, the power output of the entire string drops to zero, leading to hotspot heating. Hot spot heating occurs when the excess power in all other cells flows through the shaded cell, causing overheating and potential damage.

Bypass diodes are connected parallel to the solar cell but with opposite polarity to prevent hot spot heating. During regular operation, when the solar cell is unshaded, it is forward-biased, while bypass diodes are reverse-biased and act as open circuits. However, a shaded cell becomes reverse-biased when excess power passes through it, causing the bypass diode with opposite polarity to conduct. Excess power can flow through the bypass diode rather than the shaded cell, preventing hot spot heating [60]. Ideally, each solar cell in a module should have a bypass diode. However, installers typically use one bypass diode across multiple solar cells in real installations for economic reasons.

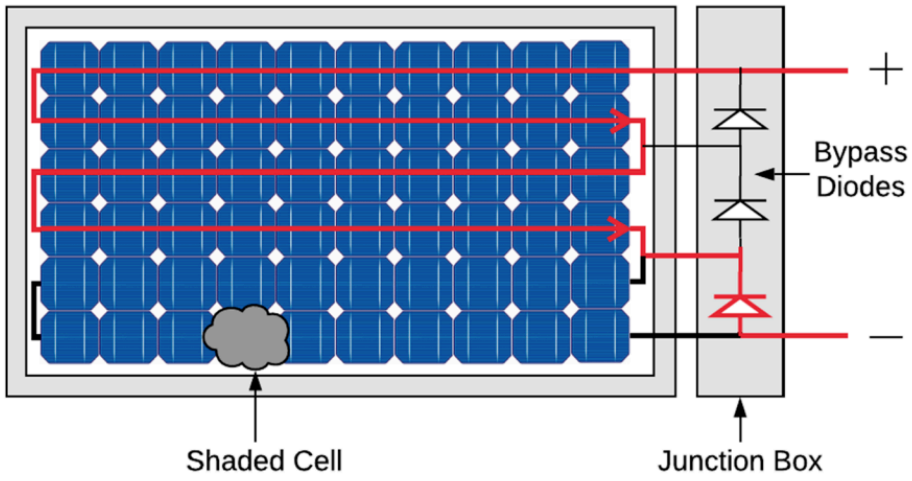

Fig. 20. Example of how a bypass diode can be used with a shaded cell [61].

Fig. 20 shows how we can use bypass diodes in a solar module. The module consists of three strings of 20 cells, with one bypass diode installed for each string. Suppose we expose a cell in the bottom string to shade. In that case, the string is isolated, allowing the solar module to continue producing electricity at a lower voltage rather than not at all. As our study takes place in Tromsø, it would be reasonable to assume that parts of each module can be snow-

covered. Installing the solar module horizontally (as in Fig. 20) ensures that the two top strings continue to produce electricity, thanks to the bypass diodes. In contrast, if the module is vertical, some cells in each string would be shaded, causing a low power output.

Solar modules produce direct current (DC), whereas electricity grids and households require alternating current (AC). Inverters play a crucial role in making the generated electricity usable by converting it from DC to AC. The size of the solar PV system determines the number and size of the inverters we require. Still, ideally, the inverter(s) should have a capacity that matches or exceeds the system's capacity to avoid any avoidable losses during periods of high power generation.

The role of power optimizers in the system is critical to maximizing energy production [62]. They are DC/DC converters with a Maximum Power Point Tracker (MPPT) technology, which we attach to the solar cells (usually at the back) to track their peak output and adjust the voltage in real time so that we can extract the solar module's maximum power output. The power optimizers optimize the electricity produced in each panel before it flows to the inverter to ensure the system generates as much electricity as possible at any given time.

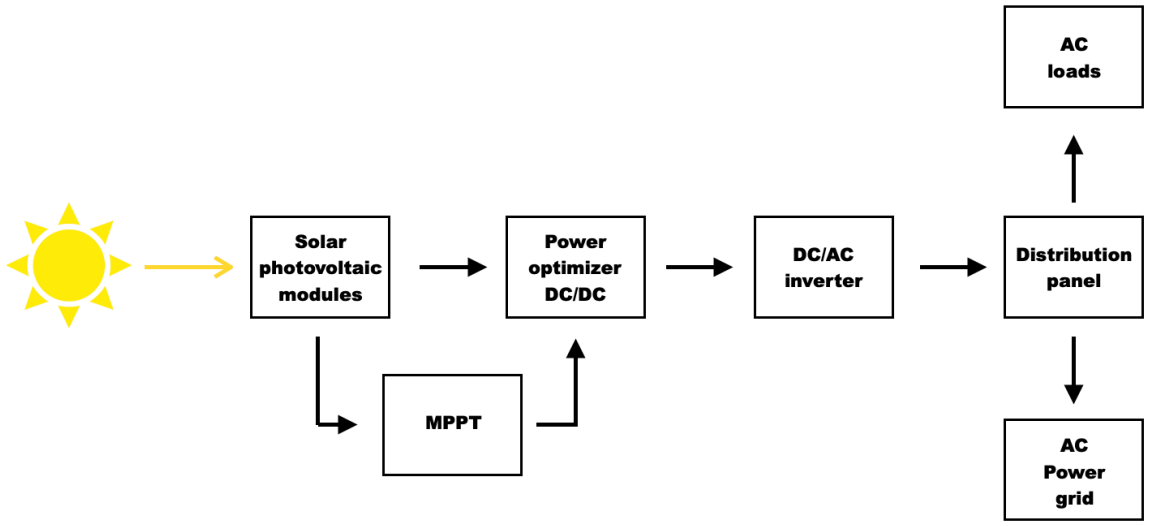

Fig. 21. Simple block diagram of a grid-connected solar PV system.

Fig. 21 demonstrates a typical grid-connected solar PV system, showing the system's key components. We assume that both the OES and ILP systems are assembled similarly. Next, we will look at the energy performance of solar photovoltaic systems and identify factors that influence their performance in high-latitude regions.

2.3 Energy performance

2.3.1 Energy performance of solar photovoltaic systems in Tromsø

We use the term energy performance of a solar photovoltaic system to measure the system's effectiveness and efficiency in converting incident solar radiation into usable electrical energy. Although we measure the performance rating of such systems under STC, the actual performance of the cells will vary due to factors such as the variability of solar irradiance and changing module temperatures. The performances of real systems are affected by system size, orientation, tilt angle, efficiency, design, geographical location, and climate at the installation site. We delve into factors that are important for our systems in Tromsø.

We must consider the availability of solar radiation when designing solar photovoltaic systems that are effective and efficient. In the context of system design, we consider the shading mask. The *shading mask* indicates portions of the sky that is visible or obstructed from the system. Nearby structures, trees, hills, and mountains can shade the solar modules, lowering energy production. We thus need to consider nearby sources of shading. However, the most critical factor in solar radiation availability is solar altitude.

Latitude and solar altitude have a changing relationship throughout the year, leading to significant variations in day length associated with the seasons in high-latitude regions. Beyond the Arctic Circle, two unique phenomena occur. These phenomena include polar day, when the sun never sets, and polar night, when it never rises, with the duration of each period increasing with latitude [63]. Tromsø, located at 69°N above the Arctic Circle, experiences both phenomena. The sun remains below the horizon from November 27 to January 15 at this latitude. However, due to the mountain ranges surrounding Tromsø, the polar night phenomenon is extended locally from November 21 to January 21 [64]. On the other hand, the polar day (or midnight sun) occurs from May 20 to July 22 [65].

Fig. 22 shows the hours of daylight and sunrise and sunset times in a year in Tromsø. Related to this, the solar altitude remains relatively low throughout the year, peaking at approximately 44° at solar noon on the summer solstice, occurring on June 21 [26]. We expect the energy performance of the systems to be affected significantly by the low availability of solar radiation in the research period, which extends from September 20 to April 30.

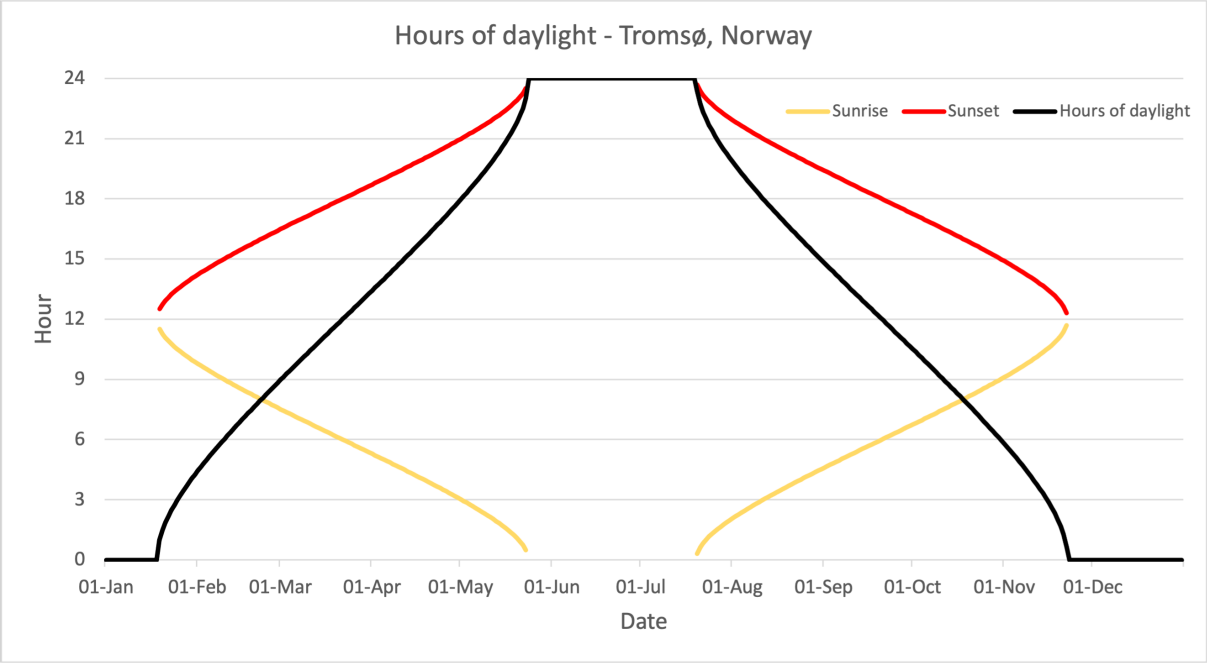

Fig. 22. Hours of sunrise, sunset, and daylight in Tromsø. Data gathered from: https://www.pveducation.org/pvcdrom/properties-of-sunlight/calculation-of-solar-insolation

The temperatures in Tromsø in the past decade suggest that low temperatures can be a concern for electrical power systems in the region. Studies show that the working temperature of a solar cell has a significant effect on its efficiency. However, a lower temperature benefits solar photovoltaic systems, as temperature and efficiency have an inverse relationship. The efficiency of a solar cell is estimated to decrease by 0.45 % for every degree Celsius increase in temperature [66]. When determining the rating of solar modules, they test them under STC, which involves a 25 °C module temperature during testing. As a result, we expect that with the generally low temperatures in Tromsø, the solar modules can perform better than their rated power. However, low temperatures introduce the risk of snow and ice, which we know is a significant factor in Tromsø.

Snow and ice are terms used interchangeably, but in the context of solar photovoltaic technology, they have different optical properties. For that reason, we need to separate these terms. Snow is highly reflective, whereas ice is mostly transparent to solar radiation [67]. For solar cells, these properties make a difference. A study suggested that an accumulation of rime ice on a solar module could increase its efficiency due to its transmissivity and the

cooling capability it presents [68]. In contrast, keeping a snow cover on top of the solar modules is no net benefit.

Fig. 23 shows the significant number of days a year with snow cover in high-latitude regions. Based on the illustration, we approximate the expected number of days with a ground snow cover in Tromsø is 150-200. Hence, we need to consider the effect of snow and ice on the energy production of a solar photovoltaic system. For solar photovoltaics to be a viable option for energy production, we must take measures to deal with the challenges snow and ice represent.

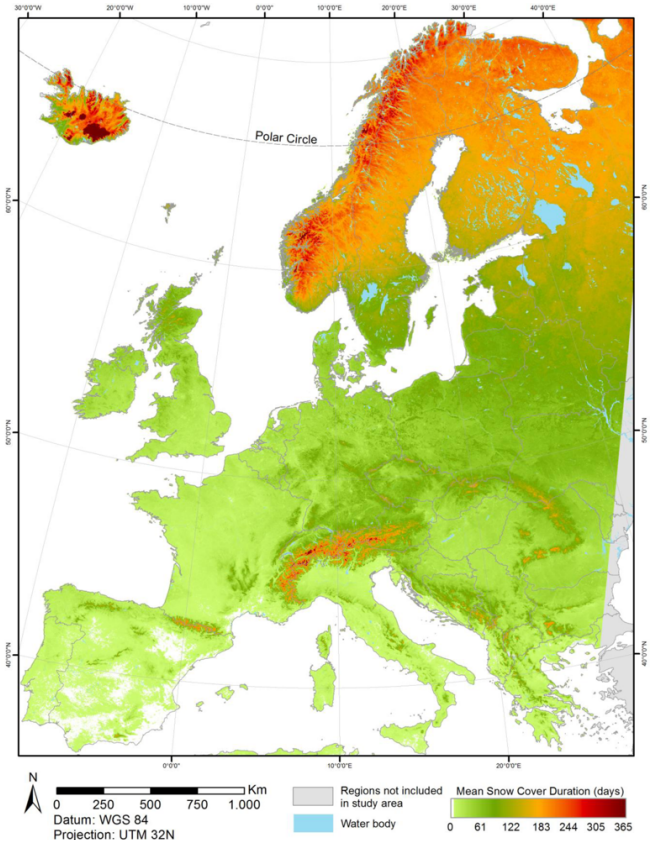

Fig. 23. Mean number of days with a snow cover in Europe from 2000 – 2011 [69].

First of all, the reflectivity of snow can enhance energy production. In an area with snow cover, the snow is a natural reflector of solar radiation. Solar radiation that would otherwise be lost can be reflected onto the solar cell, increasing the absorption of solar radiation. We estimate that the incoming reflected solar radiation from the surroundings of the solar cell is 3-6 times higher when the surroundings are covered in snow [67]. This effect applies to both bifacial solar cells' front and rear sides. An additional benefit for bifacial cells is that snow can reflect transmitted radiation into the rear side cell. The increased albedo is a benefit with a

considerable number of days with snow cover in Tromsø. That is, if the solar cells are not snow-covered themselves.

Snow can accumulate on the solar cell, obstructing the solar radiation from reaching the cell, and we base this discussion on information from research performed by Andenæs et al. [67]. Partial and full (uniform) shading have different consequences. Uniform shading, typically caused by overcast weather or a full snow cover, significantly reduces the cell's power output. Even a super thin snow cover could reduce the energy production of a solar cell to almost nothing. A 2 cm layer of snow on top of a solar cell can reduce the transmission of solar radiation by 90%, and a 10 cm layer of snow implies zero electricity production regardless of the available solar radiation.

On the other hand, nearby sources of shading or a partial snow cover can cause partial shading, which can have complex effects on the electric currents. Issues due to partial shading are the reason for the introduction of bypass diodes. Partial shading of the solar cell can lead to a significant reduction in energy production, and the reduced energy production rate is disproportional to the shaded area. We expect the issues of full and partial shading to be of significant importance in this study due to snow. Furthermore, unless removed, an accumulated layer of snow on the surface of the cells could persist for an extended period before it melts away.

An accumulated layer of snow further introduces the risk of physical damage due to the added weight on the surface. Typical damages for solar cells include glass cracking and delamination. For this reason, a solar photovoltaic system needs to be robust and adapted to its environment. Furthermore, manually removing snow or ice could lead to more damage than the snow itself. Forcibly removing the snow can lead to glass cracking, panel breaking, or abrasion damages. In this study, we will not manually remove any snow or ice from the systems.

Snow also introduces the risk of mechanical damage or dislodging from the installation points in extreme weather conditions. However, solar photovoltaic systems generally are sturdy and can withstand heavy weather. Installers should adapt each system to the weather and its corresponding challenges on the installation site. Rain and moisturization do not generally threaten the modules due to the encapsulation. However, it can harm other electrical equipment [67]. Unexpectedly, rain can improve the performance of solar modules by

removing dirt and debris from the modules that may have accumulated over time. In that way, the rain naturally cleans the solar modules. Wind can have the same effect, in addition to cooling down the solar modules. On the other hand, wind could also blow dust and sand onto the cells.

Now that we have identified and addressed significant factors that affect the energy performance of solar photovoltaic systems in general and Tromsø, we will move on to some commonly used energy performance metrics to analyze the systems' performances in this research.

2.3.2 Energy performance metrics

The solar photovoltaic industry commonly uses several metrics to measure energy performance, including efficiency, energy yield, specific yield, availability, performance ratio, and capacity factor. These metrics provide different information regarding a system's performance.

The I-V characteristics of a solar cell describe the relationship between current and voltage under different sunlight and temperature conditions. It measures energy performance in the form of efficiency and power output. Fig. 24 shows a solar cell's I-V (current-voltage) curve and a P-V (power-voltage) curve and marks and labels relevant points. The maximum current, the short-circuit current (I_{SC}), is produced when the module is shorted (no resistance) and the voltage is zero. The maximum voltage, the open-circuit voltage (V_{OC}), on the other hand, occurs when the resistance is infinite and the current is zero. The two extremes in resistance are on each end of the I-V curve below, and other possible combinations of current and voltage are in between these points.

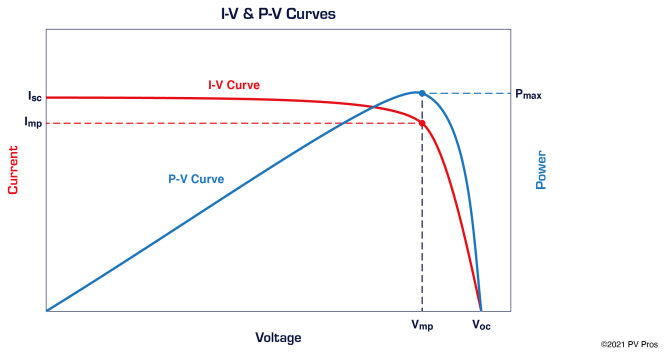

Fig. 24. Current-voltage (I-V) and power-voltage (P-V) curves for a solar cell [70].

The maximum power point (MPP) is in the "knee" of the I-V curve, where the product of the voltage and current is the highest. The system's power output is the highest at the MPP, hence the optimal operating point for a solar cell. The role of power optimizers in solar photovoltaic systems is to keep the I-V relationship at the MPP at all times during production. Hence, they adjust the voltage in real time depending on the current generation in the cell to maximize the system's power output. We define the maximum power output of a solar cell as:

$$P_{max} = V_{mp} \times I_{mp} \quad (2.6)$$

V_{mp} and I_{mp} represent the voltage and current at the MPP. To achieve the highest possible efficiency of a solar cell, it must operate at the MPP. We define the efficiency of a solar cell as the ratio of the produced energy of the solar cell to the received solar energy [59], written as:

$$\eta = \frac{P_{max}}{P_{in}} \quad (2.7)$$

P_{max} is the solar cell's maximum power output, and P_{in} is the input energy from the sun. The higher the maximum power output of the solar cell, the higher the conversion efficiency and energy yield. We will not further investigate the I-V and P-V relationships in this research. However, we included the introduction to understand better the power optimizer's role and the relationship between the current and voltage in a solar cell.

The *energy yield* of a solar photovoltaic system is the electricity produced by the system over a certain period, usually measured in kilowatt-hours (kWh). It reflects the total amount of energy the system has produced. An additional important performance metric is the *specific yield* of the system, which we typically measure in kilowatt-hours over kilowatt-peak (kWh / kW_p). It is the energy yield divided by the system's installed capacity over a period. Because it includes the system's capacity, the specific yield is suitable for measuring the *energy production efficiency* of systems, regardless of their sizes, making it particularly interesting for comparisons of systems. We will use it when we compare the systems' performances.

We also want to address the *availability* of systems, which we define as the measured hours of energy production divided by the operating time [71]. It measures the time the system is operational and available for power generation, considering downtime and weather events, including snow cover. We mark an hour as unavailable when the system's energy output is zero. A higher availability implies a more reliable system. We consider this metric essential because it gives us an idea of how snow and the availability of solar radiation affect the systems. This metric will reveal if snow completely covers a system in the research period. We want to look at it in conjunction with other metrics to reveal the characteristics of the systems.

We define the performance ratio as the measured production divided by the modeled production [71]. The metric is a measure of the actual output of a system relative to its theoretical maximum output. The calculation considers the effects of shading, temperature, and other losses. A higher performance ratio implies a more effective system. This metric will reveal how well the systems utilize the available solar radiation.

The capacity factor is the final metric we include in the study, which we define as the annual average energy production relative to the theoretical maximum output, assuming it operates at its rated capacity every hour of the year [72]. We can also calculate the metric over shorter periods than a whole year. Researchers typically use the capacity factor to compare the performances of solar photovoltaic systems or to assess the potential energy output of a system in a new particular location. A higher capacity factor implies that the solar photovoltaic system generates more energy per rated capacity.

We have identified energy performance metrics and factors affecting them in Tromsø. As the final part of our theoretical framework, we will introduce the PVSyst software, which we will use to predict the expected and maximum performances of the systems in the data analysis.

2.4 PVSyst software

PVSyst is a software program to analyze, design, and optimize solar photovoltaic systems [73]. Researchers, engineers, and solar energy companies widely use the software to analyze and perform simulations of the performance of solar photovoltaic systems. The software allows the user to input different parameters of a solar photovoltaic system to model its performance. These parameters include geographical location, PV system characteristics and composition, and climate data. The software uses advanced algorithms to calculate the system's performance under different conditions, where the software considers local weather and potential shading. The result includes a detailed financial analysis to investigate the system's economic viability. The software interface is also user-friendly, allowing users to access and manipulate data easily. Detailed graphs and output reports are available.

An accurate approximation of solar irradiance and irradiation is crucial when we evaluate the performance of the solar photovoltaic systems in simulation models. We will utilize two commonly used methods when conducting our research: clear sky models and Typical Meteorological Year (TMY) models. Clear sky models use geographical location and atmospheric conditions to perform theoretical calculations. They consider absorption and scattering but not the effect of weather. In contrast, TMY models use historically averaged weather and climate data from the installation location to simulate a typical year at the installation site. Designed for different applications, we use clear sky models to theoretically analyze an ideal situation, whereas TMY models are better for practical applications such as energy yield forecasting. Comparisons of the predicted solar irradiance performed by the two models provide valuable insight into the difference between ideal and actual conditions on-site. Due to each model's valuable characteristics, we will use both in this research.

3 Methodology

Fig. 25 illustrates the locations of the systems we will analyze for their performance and the distance between them. The difference in altitude between the system buildings is approximately 40 m, whereas the ILP system building is higher in the terrain.

Fig. 25. Relative locations of the solar photovoltaic systems illustrated in QGIS.

3.1 Over Easy Solar (OES) system at Posten, Tromsø

The OES system is a grid-connected prototype of Over Easy Solar AS installed on the top of the Posten AS headquarters in Tromsø, Norway (69.68°N, 19.00°E). The building is 10 m tall with a flat roof with PVC/foil-type roofing. The commission date of the system is June 28, 2022, and Fig. 26 shows pictures of it.

Fig. 26. The pilot system of Over Easy Solar AS.

The system consists of vertically installed bifacial modules facing east-west in two columns of 7 units, where each unit consists of 3 solar modules of 7 solar cells (21 solar cells in total per unit). The distance between each row is 40 cm, and the height of each module is 23.8 cm (20.6 cm is glass, and the rest is mounting support). Fig. 27 illustrates the layout and measurements of the system.

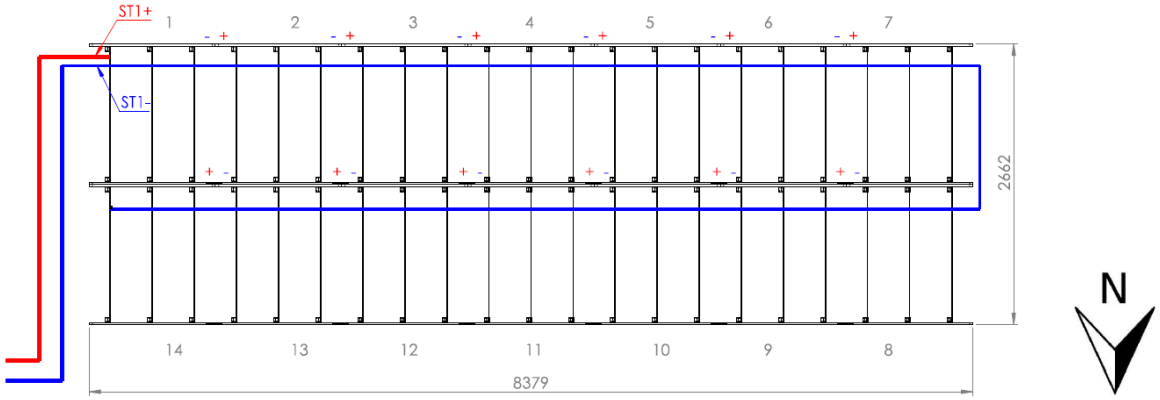

Fig. 27. Layout and string diagram of the system with dimensions in millimeters. Scale 1:33. Figure courtesy of Over Easy Solar AS.

The solar cells are of silicon heterojunction technology (HJT) and have dimensions of 157 x 157 mm (area of 246.5 cm^2). They are busbarless with SmartWire Connection Technology ($SWCT^{TM}$), patented by Meyer Burger. This technology replaces standard busbars with copper micro-wires, reducing the cells' shading and enhancing the active surface area for energy conversion due to the possibility of placing the wires closer together. The modules have thermally toughened protective glass and an aluminum frame. The system's inverter is a Sunny Boy SB 1.5-1 VL-40, with a rated power of 1.500 kW. We will provide the inverter's specifications in section 4.2.1. Table II and Table III summarize the specifications of the system and the electrical data of the solar panels, respectively.

TABLE II

OES SOLAR PHOTOVOLTAIC SYSTEM SPECIFICATIONS

Component Or Parameter	**Name Or Value**
Latitude	69.68 °N
Longitude	19.00 °E
Solar PV system capacity	1.362 kW_p
Inverter capacity	1.500 kW
No. of inverters	1
Type of PV module	Silicon bifacial heterojunction technology (HJT)
Solar module orientation	E-W (fixed)
Solar module tilt angle	90°
Active area of PV modules	14.5 m^2 (7.25 m^2 on each side)
Total roof area covered	22.3 m^2

TABLE III

ELECTRICAL DATA OF THE OES SOLAR PANELS UNDER STC

Parameter	Value
V_{OC}	5.12 V
I_{SC}	8.40 A
P_{MPP}	32.44 W
V_{MPP}	4.09 V
I_{MPP}	7.92 A
Efficiency (η)	23.70 %
Bifaciality	90.20 %

Fig. 28 illustrates the system and its surroundings, showing there are few nearby potential sources of shading for the system.

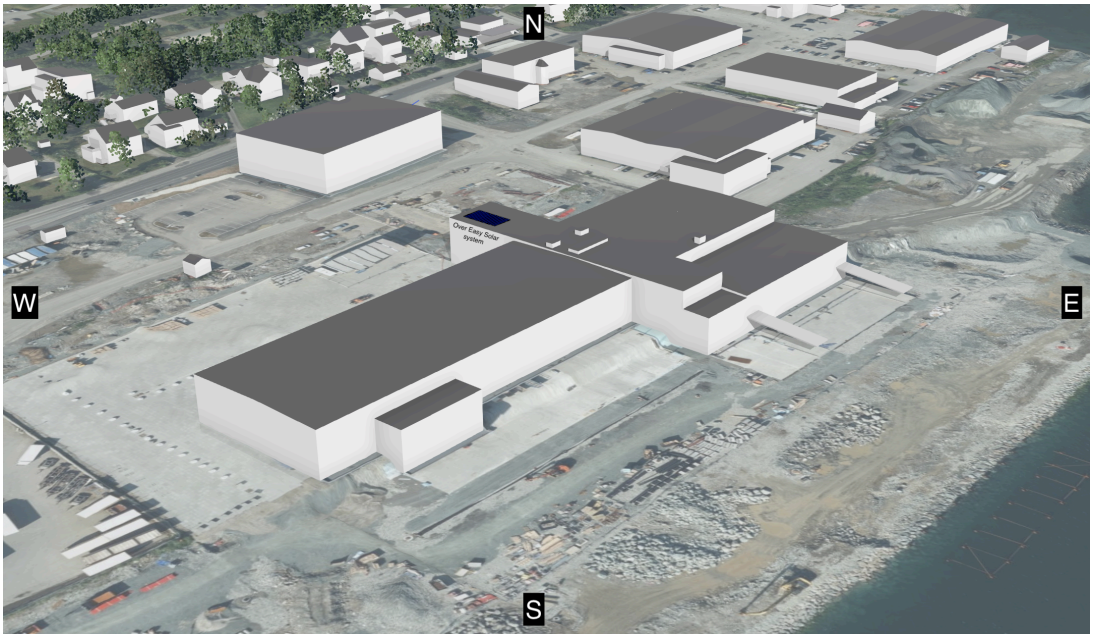

Fig. 28. Overview of the OES system at the top of Posten headquarters with its surroundings. Modification self-composed on 3D model: https://tromso.maps.arcgis.com/apps/webappviewer3d/index.html?id=c2d9b47b22134ea5ac8f3a8c83bbbdc8.

3.2 ILP system at UiT – The Arctic University of Norway

The ILP system is also grid-connected and is located on the flat roofs of "*Institutt for Lærerutdanning og Pedagogikk" (Institute of Teacher Education and Pedagogy)* – ILP – at UiT – The Arctic University of Norway (69.68°N, 18.97°E). Statsbygg owns the system, the largest system in Northern Norway. Solbes AS installed the system in May 2019, and they distributed the solar modules across four PVC/foil-type roof levels, ranging from 10 m to 24 m tall. They commissioned the system in 2020, and Fig. 29 shows pictures of it.

Between the installation and commission, the weight of snow crushed 40-50 of the 720 solar modules during winter. The installer has since replaced the crushed cells and reinforced the whole system.

Fig. 29. The ILP solar photovoltaic system. The left picture is property of Solbes AS.

The system consists of 720 REC 290 TP2 (TwinPeak 2) monofacial polycrystalline silicon modules (pc-Si), which have dimensions of 1675 x 997 mm (area of 1.67 m^2). There are two solar modules per power optimizer, resulting in 360 power optimizers for the system. The panels are all tilted by 10° to maximize the absorption of solar radiation over a year. They have four different orientations: azimuth 39° (NE), -141° (SW), 129° (SE), and -51° (NW). The solar modules spread across four parts with heights of 10 m, 13m, 20 m, and 24 m. The lowest roof has three separate sections: south (244 modules), east (54 modules), and north (54 modules). The second lowest, second highest, and highest roofs have 36, 220, and 112

modules, respectively, adding up to 720 modules. Fig. 30 shows an overview of the system. Solbes have installed two inverters of type SE82.8K-RW0P0BNU4, each with a rated power of 82.8 kW. The inverters have nine strings with 20 power optimizers (40 modules) per string. Table IV and Table V show the ILP system's specifications and the electrical data of the solar cells, respectively.

TABLE IV

ILP SOLAR PHOTOVOLTAIC SYSTEM SPECIFICATIONS

Component or parameter	**Name or value**
Latitude	69.68 °N
Longitude	18.97 °E
Solar PV system capacity	208.8 kW_p
Inverter capacity	165.6 kW
No. of inverters	2 (each of 82.8 kW)
Type of PV module	Monofacial polycrystalline silicon (pc-Si)
Solar module orientation	NE-SW (fixed), SE-NW (fixed)
Solar module tilt angle	10°
Active area of PV modules	1114 m^2
Total roof area covered	1250 m^2

TABLE V

ELECTRICAL DATA FOR THE ILP SOLAR CELL UNDER STC

Parameter	**Value**
V_{OC}	38.8 V
I_{SC}	9.71 A
P_{MPP}	290 W
V_{MPP}	32.1 V
I_{MPP}	9.05 A
Efficiency (η)	17.4 %
Bifaciality factor	N/A

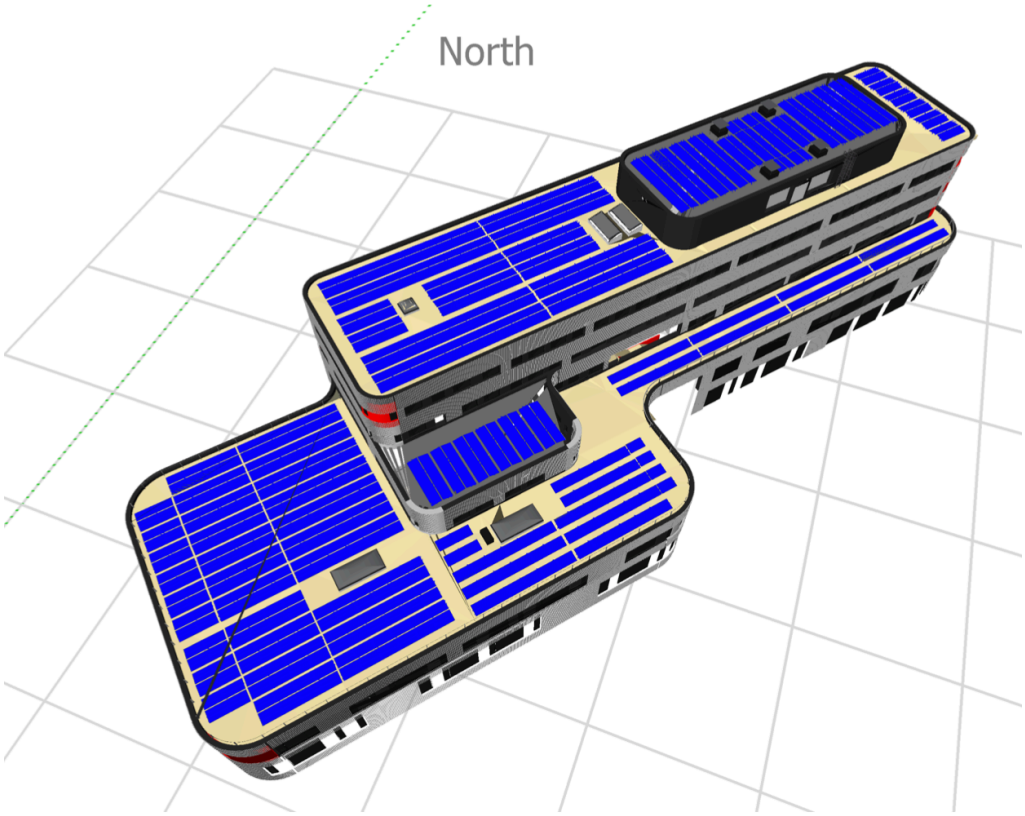

Fig. 30. Overview of the ILP system. Figure courtesy of Solbes AS.

4 Simulation software and data

4.1 Modeling a grid-connected system in PVSyst

We want to perform simulations of the system performances to compare the actual performances of the systems to their theoretical performances. A license is required to use PVSyst, so we bought a full-year student license to perform the simulations.

For our purpose, we need to look at how to model a grid-connected system in PVSyst before we demonstrate how we model the systems of research. We base the explanation of the required inputs on a PVSyst user manual [74], where we also use some of the instructive pictures.

After opening the software, we press the "Grid-Connected" button under project design and simulation, as Fig. 31 illustrates, to initiate a grid-connected system project.

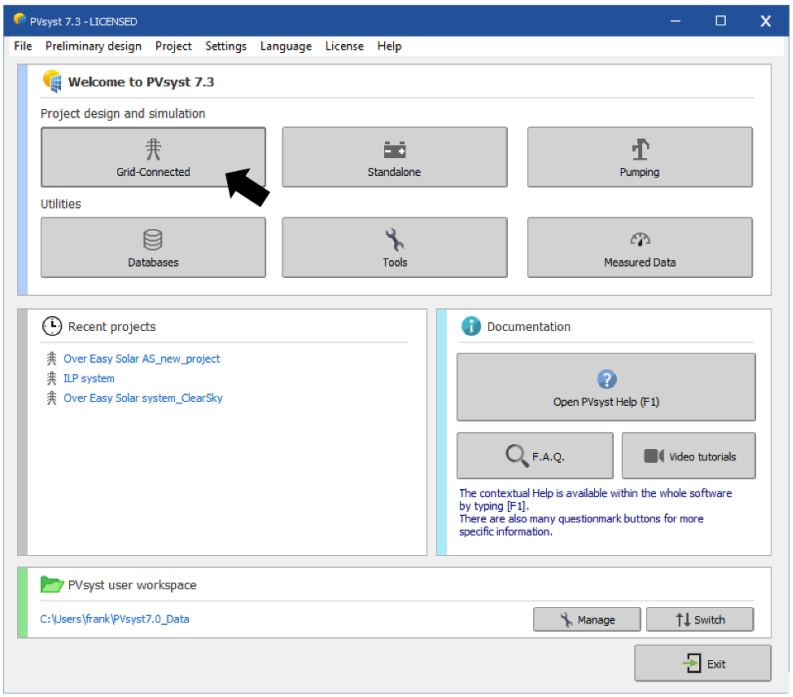

Fig. 31. Initiating a grid-connected project design.

After initiating the project, we see a dashboard for the management of the project (Fig. 32). It contains the basic definitions of the project and system variants. We proceed to give the project a name and start defining the project. The first step is to add a site file.

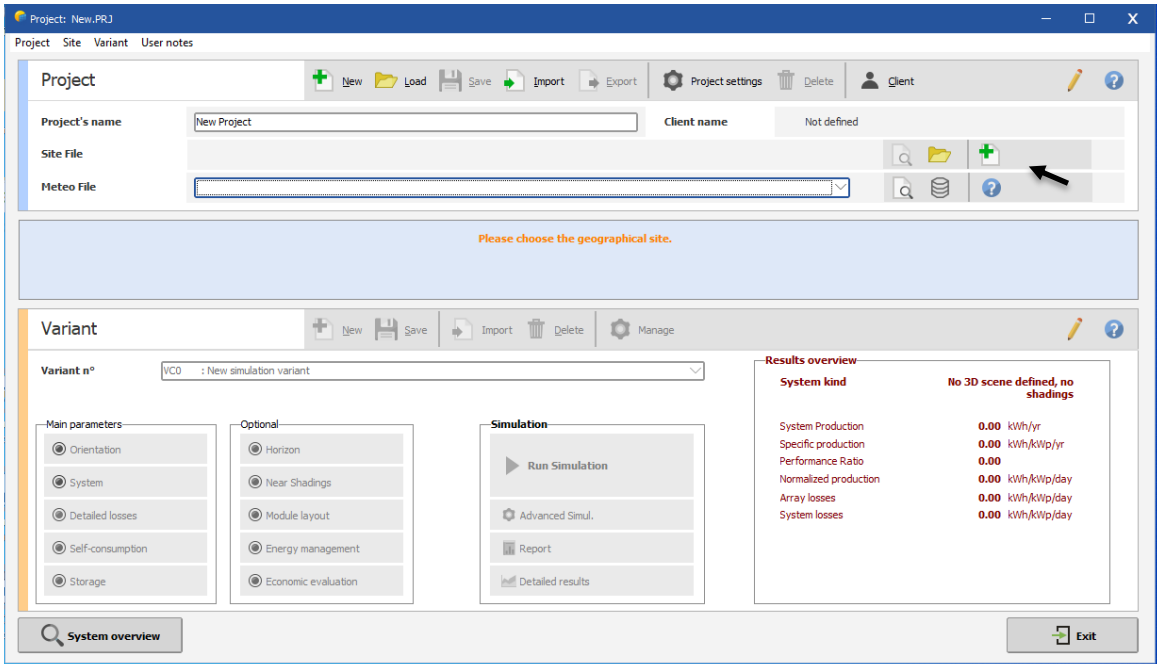

Fig. 32. Dashboard of a grid-connected system.

4.1.1 Implementing geographical and meteorological data

When choosing the installation site of the system, we can choose from around 2550 preset locations or specify the locations of the system using an interactive map or by specifying its exact coordinates.

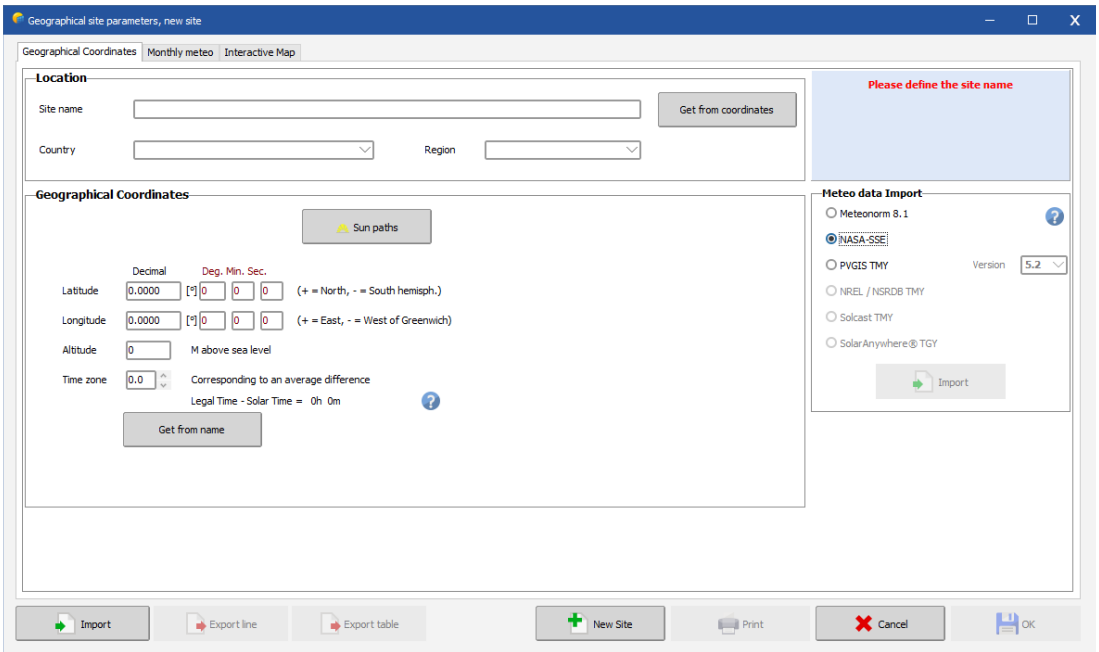

Fig. 33. Geographical site parameters and meteorological data.

Upon choosing the geographical location of the system, we can generate a file containing averaged hourly meteorological data at the location. We base the simulation on these data, which we can generate in the “Meteo data import” section on the right side, choosing the desired data source. We can save the meteorology file associated with the location and use it as a basis for the simulation. When saving the user input on this page, we can choose the desired meteorology file from the dashboard. The meteorology file we generated bases its content on a TMY. However, it is also possible to generate a custom meteorology file. For example, we will create a clear sky file, where every hour exhibits clear skies, to simulate ideal meteorological conditions. We perform this by the steps Fig. 34 illustrates, where the user must input the installation location and specify the Linke turbidity factor, which measures the atmospheric absorption and scattering of incident solar radiation under clear skies. The factor typically ranges from 1 to 10, where 1 indicates an arid and clean atmosphere [8], and it typically increases during summer and decreases in winter. The software suggests default values of the factor.

We choose the desired meteorology file on the project dashboard and save the project.

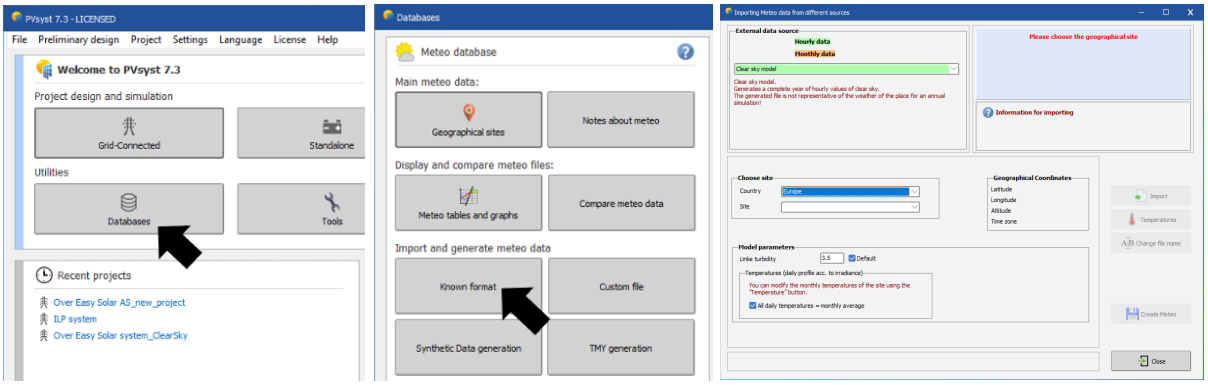

Fig. 34. The steps to create a clear sky meteorology file.

4.1.2 Defining the system

Next, we need to specify the system variant. Two of the main parameters are marked in red, meaning that the software requires additional input before we can run a simulation. The two main parameters needed to perform any simulation are the orientation, type, and model of the solar photovoltaic modules and the inverter. We will proceed with defining the system’s orientation.

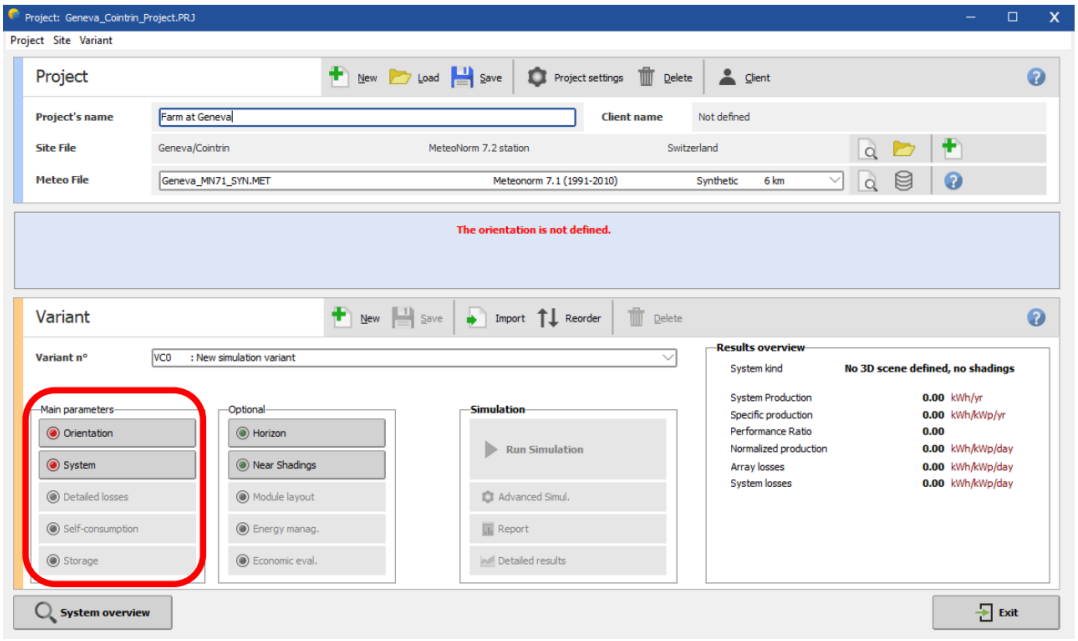

Fig. 35. Defining the system. Figure from the PVSyst user manual.

When we define the system's orientation, we will need to input the field type for the installation in addition to the tilt and azimuth of the solar modules. The field type includes fixed tilts and unlimited sheds, which we will utilize, among several other options. When we save the orientation definition, the orientation button will turn green. Now, we will define the system.

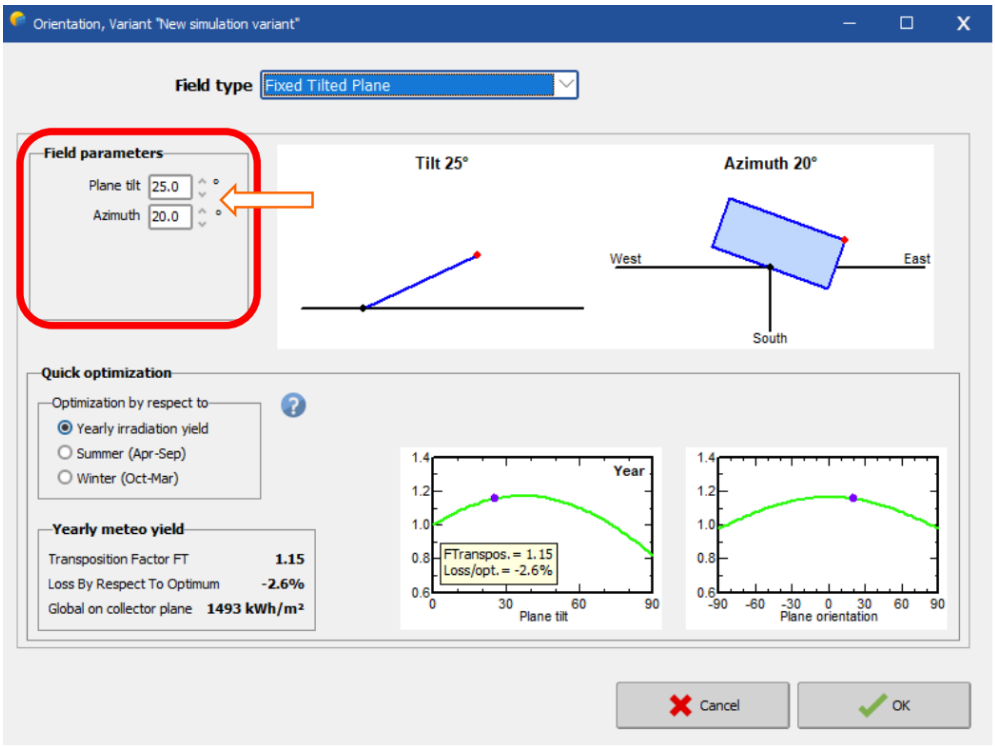

Fig. 36. Defining the orientation of the system. Figure from the PVSyst user manual.

Fig. 37 shows the dashboard of the system design. In this dashboard, we will need to select the PV modules and inverters in use and design the system based on *solar arrays*, which are collections of connected solar modules. PVSyst has a variety of solar module and inverter technologies to choose from in the drop-down menus, but we can also add new technologies manually. We can add new solar photovoltaic modules and inverter technologies by following the steps in Fig. 38. After we have created and saved new technologies, they will be available from the drop-down menus in our system definition.

We must create each subarray individually and specify the number of strings per subarray and the number of modules in each string connected in series. Additionally, we must specify their orientations if we have multiple orientations. After we have defined the system, we can save and close the system definition, and both the orientation and system buttons should be green. We have now completed all the mandatory user inputs to perform a simulation, but we will add more information about the systems to improve the accuracy of the simulations.

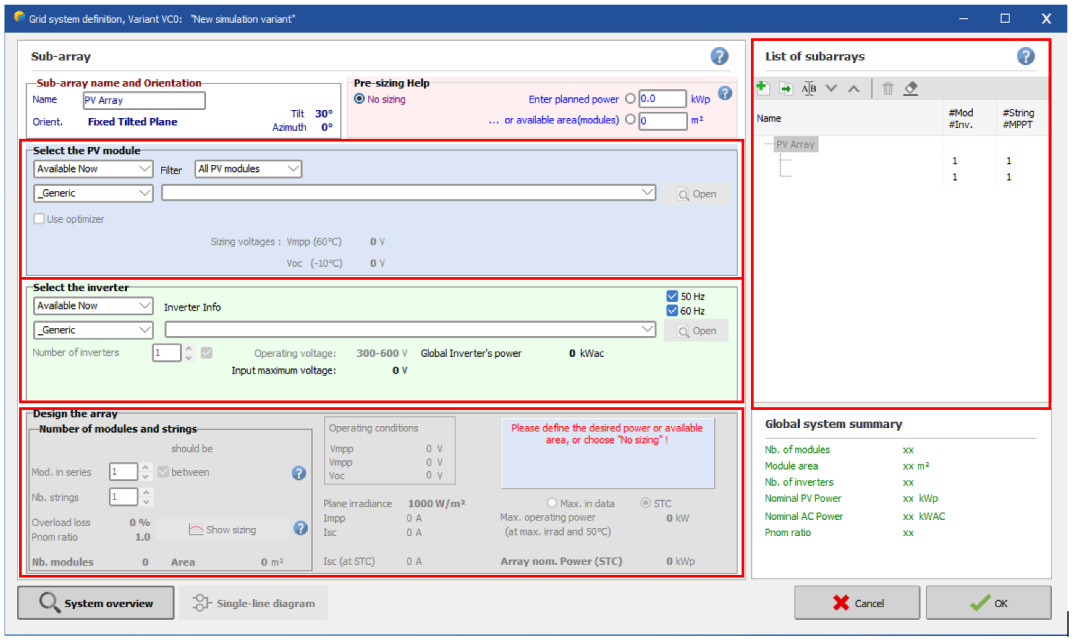

Fig. 37. Defining the system.

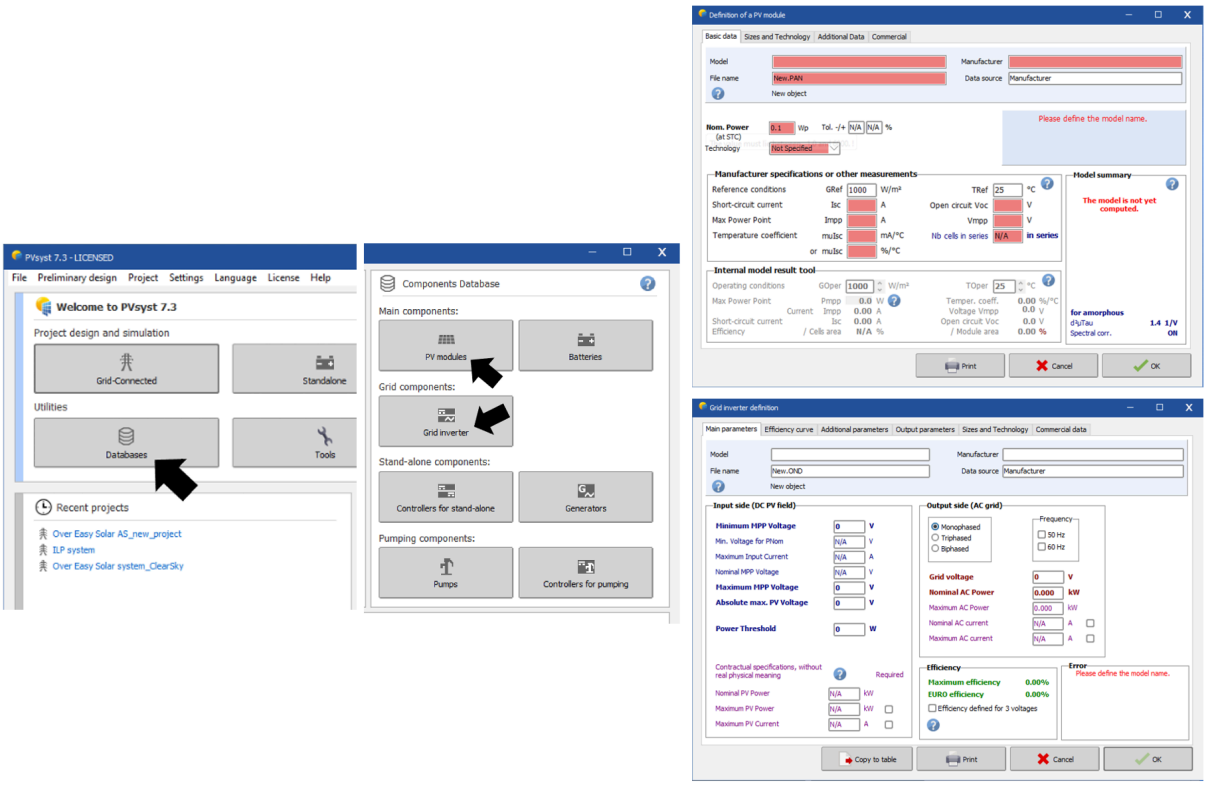

Fig. 38. Manually adding new module and inverter technologies to the software.

4.1.3 Defining horizon and near shadings

We access the horizon specifications, where we can add a horizon profile for the system indicating the shading objects that are far away. The shading objects include mountains and hills and indicate shadings that affect the entire system equally. Upon opening the horizon tab, we will see the sun paths for the site in a year. We can press the read/import button in the top left (bottom left on older versions) corner to import a horizon profile or far shading mask from external sources. Fig. 39 illustrates the choices we have. The result should be a horizon line drawing added to the sun paths of the location. Fig. 40 illustrates an example of how it can look. After defining the horizon profile, the horizon button on the dashboard should turn green.

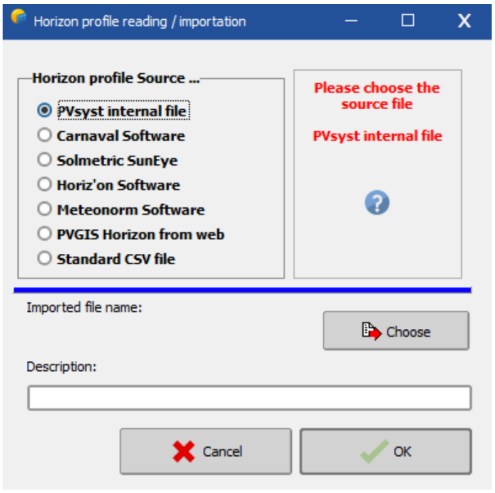

Fig. 39. Importing a horizon profile from an external source. Figure from the PVSyst user manual.

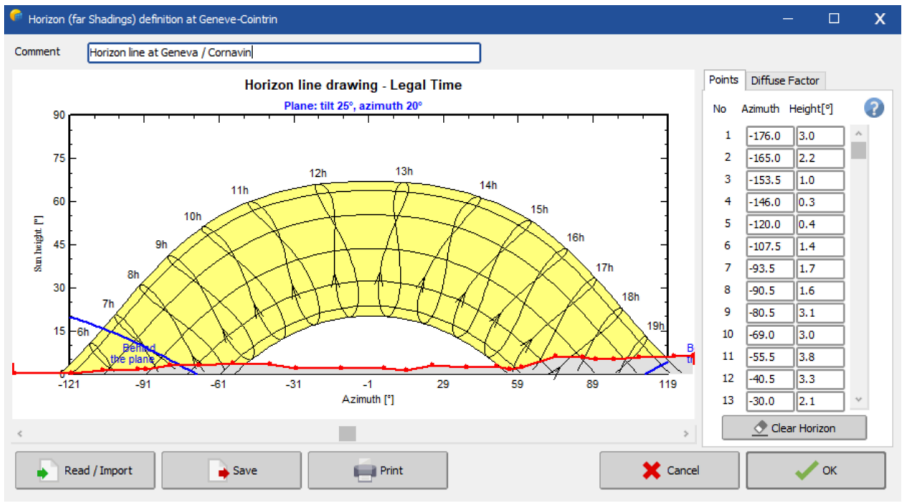

Fig. 40. Sun paths and horizon line profile. Figure from the PVSyst user manual.

Furthermore, we want to define the near shadings (buildings, trees, self-shading) of the system if we expect the shadings to significantly affect the system's energy production. We access the near shadings tab, which allows the user to create a 3D shadings scene to simulate the actual shading conditions in the installation site, including factors that affect the system components unevenly. Instead of creating the shading scenes in PVSyst, we can also import them from external sources (DAE, 3DS, PVS, or SHD formats) if we want to create them elsewhere or if they are available. Fig. 42 shows how to import a 3D shadings scene into PVSyst software. After the import, the scene will be available from the import button in the "near shadings" definition, visible in Fig. 41. The software then approximates the effect of the shadings on the system energy production based on the 3D shadings scene.

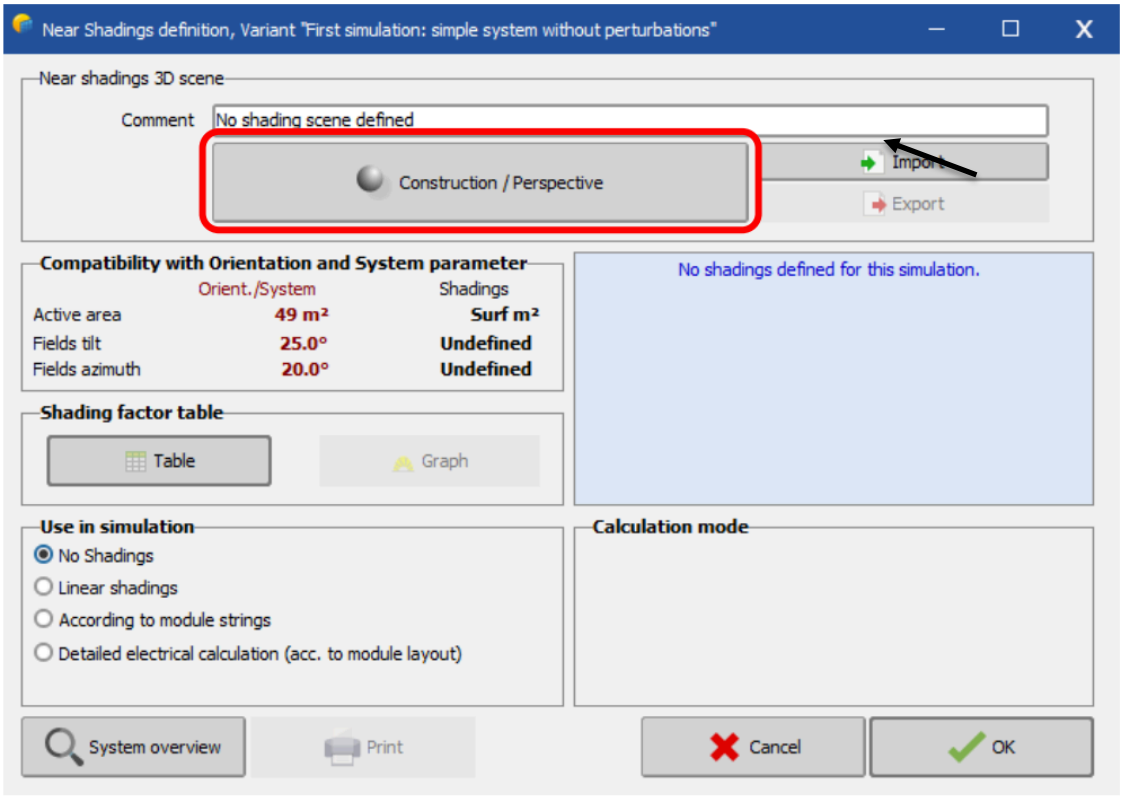

Fig. 41. The definition of the "Near Shadings". Figure from the PVSyst user manual.

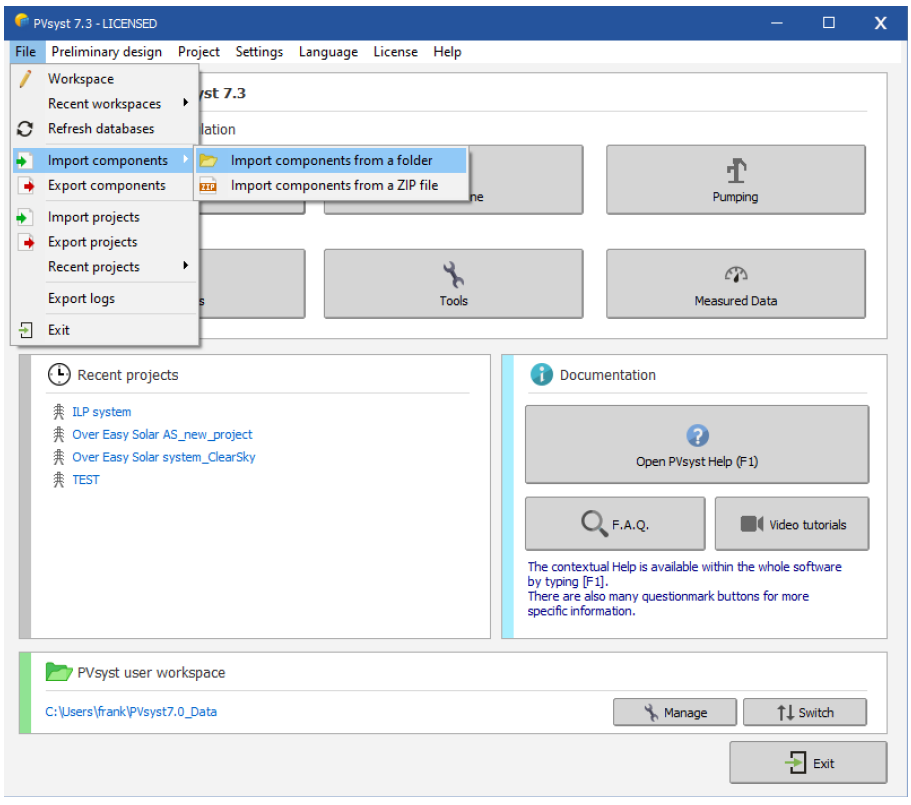

Fig. 42. Importing an external 3D shadings scene.

4.1.4 Project settings and detailed losses

We want to keep most of the other settings at the default values in the software to avoid making changes with unknown or unwanted effects on the results. However, we note the possibility of changing the ground albedo in the project settings, available from the project dashboard. We can change albedo values monthly. In addition, we can specify the expected losses we want to include via the detailed losses. Soiling losses are significant in this research due to snow, and we recognize the possibility of varying this factor monthly. We illustrate the possibility of modifying the albedo and soiling losses in Fig. 43.

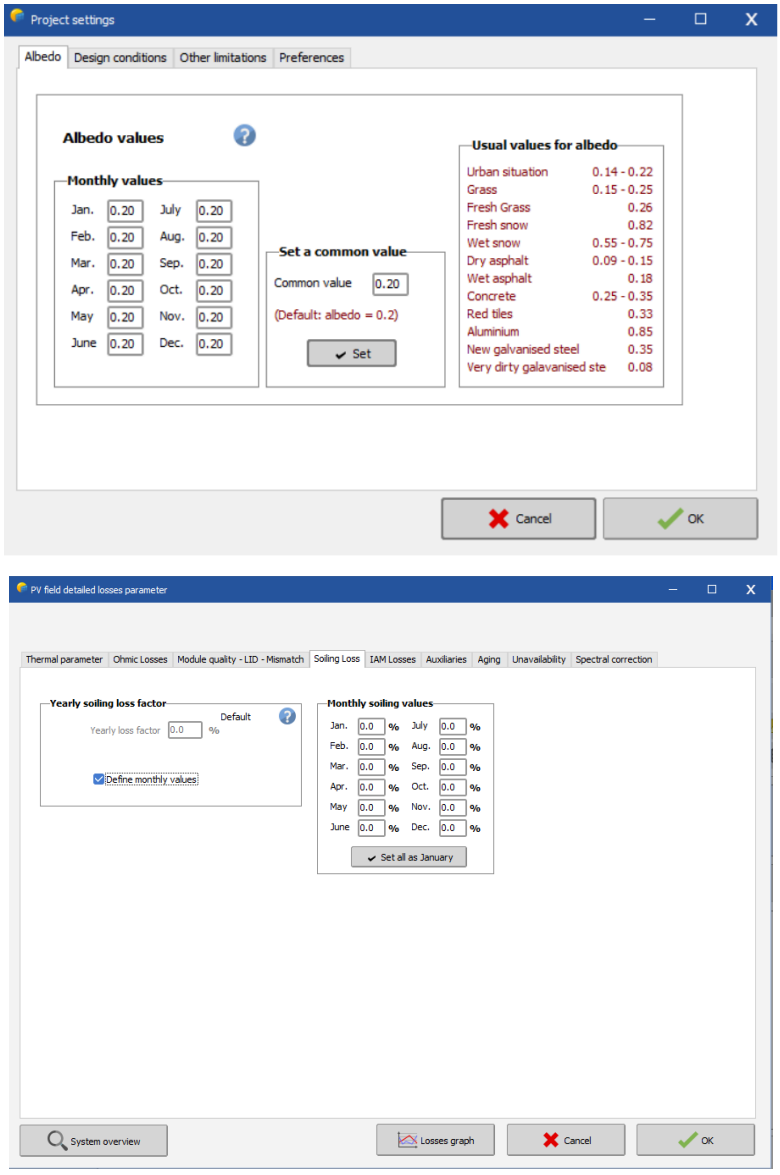

Fig. 43. Albedo and soiling losses modifications.

4.1.5 Running the simulation and output data

We have modified the most important input parameters to estimate the system performance. Now, we can simulate the system's annual performance via the "Run Simulation" button on the project dashboard. After the simulation, a report showing the most important findings is available.

In addition, we can obtain output CSV files with hourly, daily, and monthly resolutions for the variables we need. To obtain these files, we access the advanced simulation button on the project dashboard and press the output file button in the menu that appears. Fig. 44 illustrates the process of how to obtain these files. In this menu, we can format the desired data and choose where it should be stored locally. When we perform a new simulation, the software stores the data in the location of our desire. We perform the process three times to retrieve hourly, daily, and monthly data.

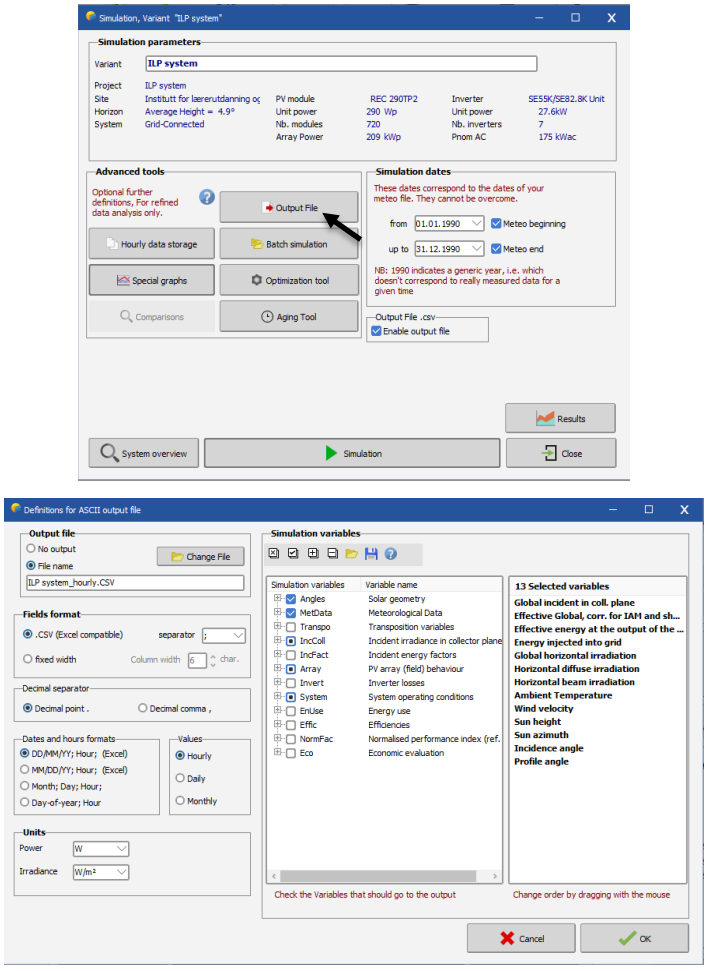

Fig. 44. Obtaining output files from a simulation.

4.2 Modeling the systems of research

We have established the simulation method we want to use to collect data for our application, and we want to apply this method to the two research systems.

4.2.1 Modeling the OES system

We start by implementing geographical and meteorological data. We will perform two simulation variants of the OES system, but the only parameter separating them is the meteorological data. Therefore, we present the difference between the simulation variants first. The rest of the implementation will be identical for the variants, and we thus only present it once.

While both variants use the geographical location shown in Fig. 45, the first variant uses imported meteorology data from the NASA-SSE external source. The imported file is named "NASA-SSE satellite data 1983-2005", which consists of monthly data averaged from 1983-2005 from satellite measurements. The imported file represents a TMY at the installation site. The meteorology file has a 1° x 1° resolution worldwide [75]. The choice of meteorology data is somewhat arbitrary, but it is a good fit for the study because it provides the necessary information on solar irradiance. Researchers have used it in numerous studies within the solar industry, and we thus consider it reliable. However, we acknowledge that there could be other available datasets that could provide more accurate data.

The second simulation variant uses a clear sky model with a Linke turbidity factor 2.8. In Tromsø, we estimate the Linke turbidity factor to range between 2-3 [8]. PVsyst suggested a value of 2.8, and we accepted this value. Fig. 46 illustrates the creation of the clear sky meteorology file.

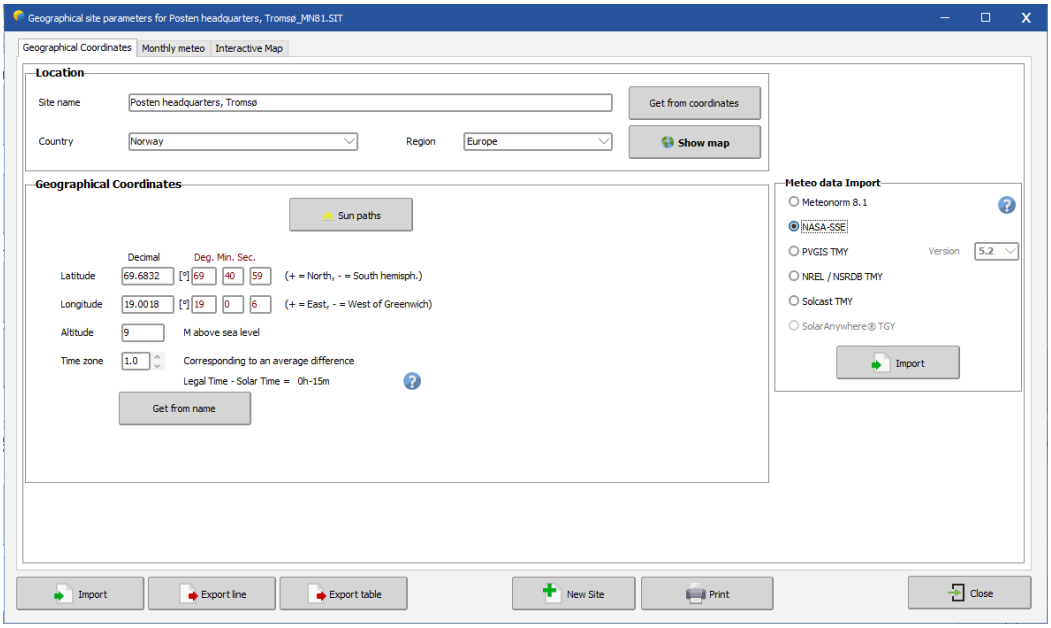

Fig. 45. The implementation of geographical and meteorological data.

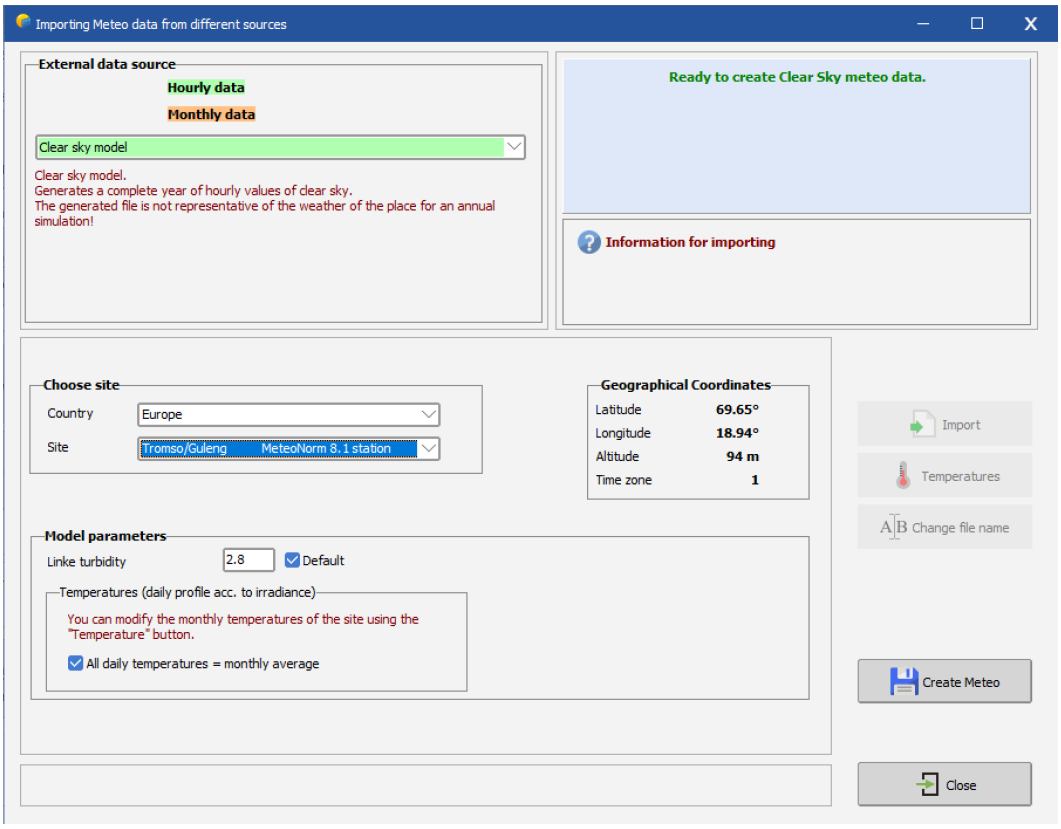

Fig. 46. The creation of a clear sky meteorological file.

Next, we must input the orientation of the system. We choose the system field type as unlimited sheds to account for self-shading from the rows of modules, as seen in Fig. 47. The module tilt is 90°, and the orientation of the modules is azimuth 90° (E). There are 21 rows of modules, and the distance between each row is 40 cm. We use information from Over Easy Solar's system documentation to input the modules' height and active parts.

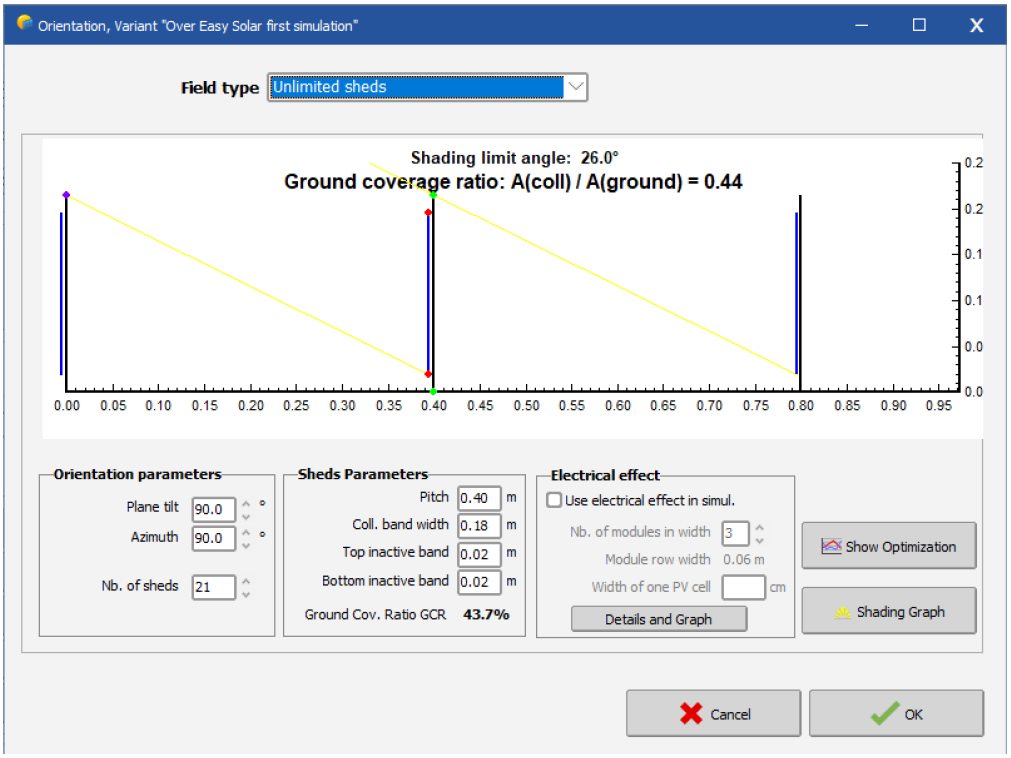

Fig. 47. The field of the solar modules modeled.

The next step is to design the system. Because the solar photovoltaic technology is a prototype and thus not registered in the software, we have to manually ingest the technology into the database. We show the process in Fig. 48 and Fig. 49. The data from Table III is necessary for the implementation. We face an issue in the implementation because the HJT technology is not available in PVSyst, which could be due to it being a technology recently gaining momentum.

For this reason, we register the technology as a HIT (Heterojunction with Intrinsic Thin-layer) technology. Both technologies use a high-efficiency heterojunction structure with amorphous and crystalline silicon. Therefore, we accept HIT as a substitute for HJT in the implementation because the technologies are somewhat similar. However, we acknowledge that this choice will result in inaccurate results due to their distinctive features and

performance characteristics. This choice makes it crucial to validate the simulation results by comparing them to the production data. We emphasize the importance of checking the box stating that the module is bifacial and specifying its bifaciality, which is visible in Fig. 49. The name of the technology in the database is “OES Panel 32.4 Wp”.

We also have to manually ingest the inverter technology into the database, as per Fig. 50. We base the technical data of the inverter on information from Over Easy Solar AS in combination with product specifications directly from the producer [76]. We name the technology “SMA SunnyBoy SB1.5-1 VL-40” and register SMA as the manufacturer of the inverter.

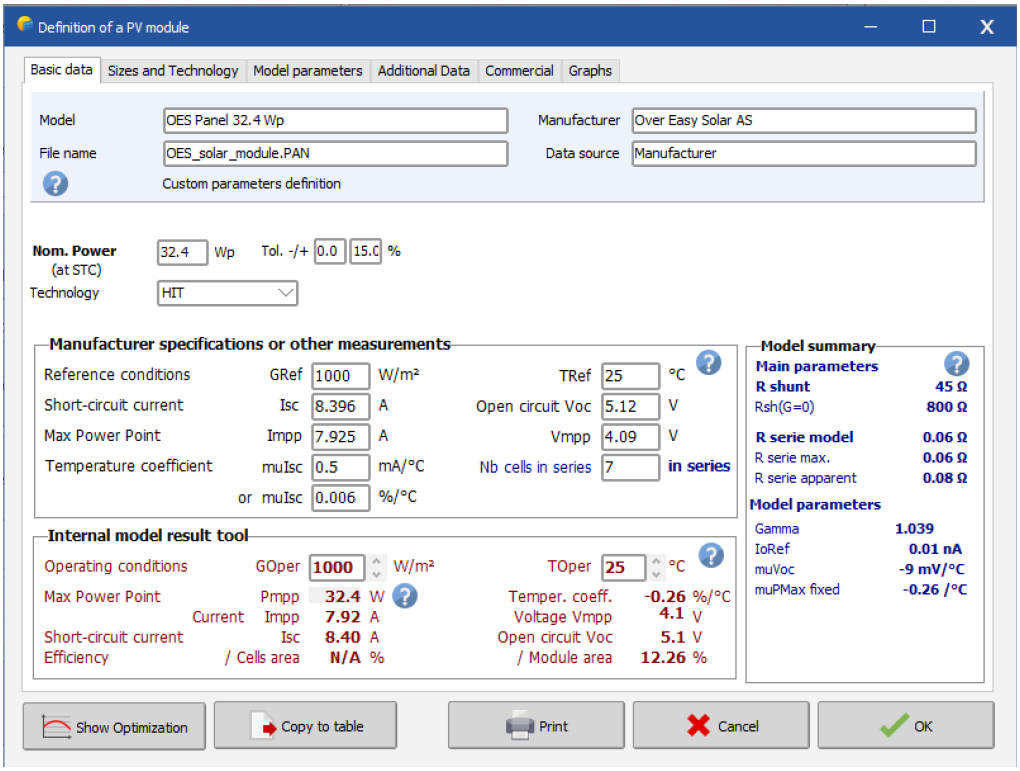

Fig. 48. Basic data of the solar module in the software.

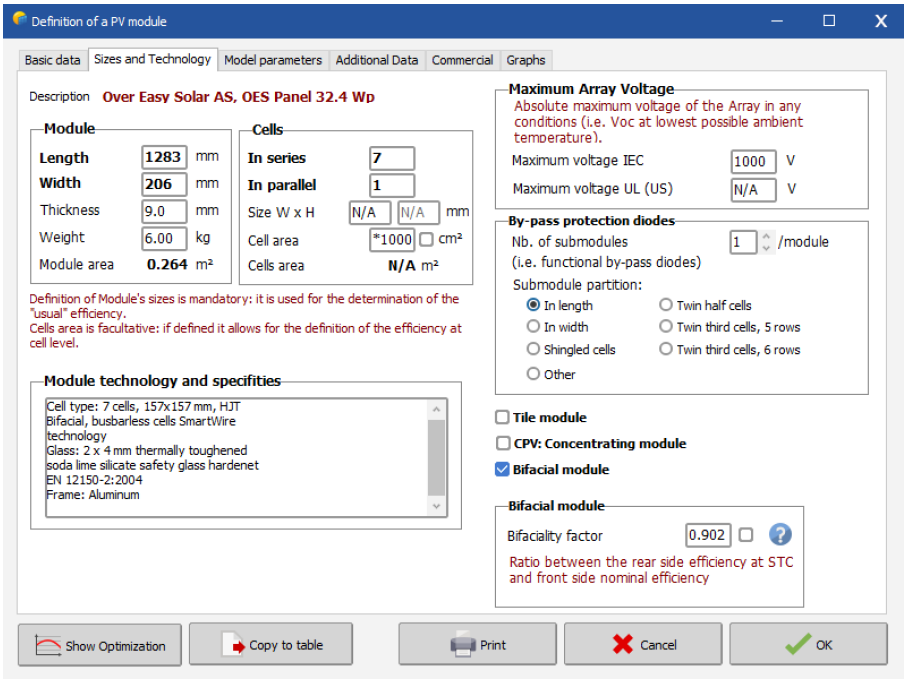

Fig. 49. Module sizes and technical specifications in the software.

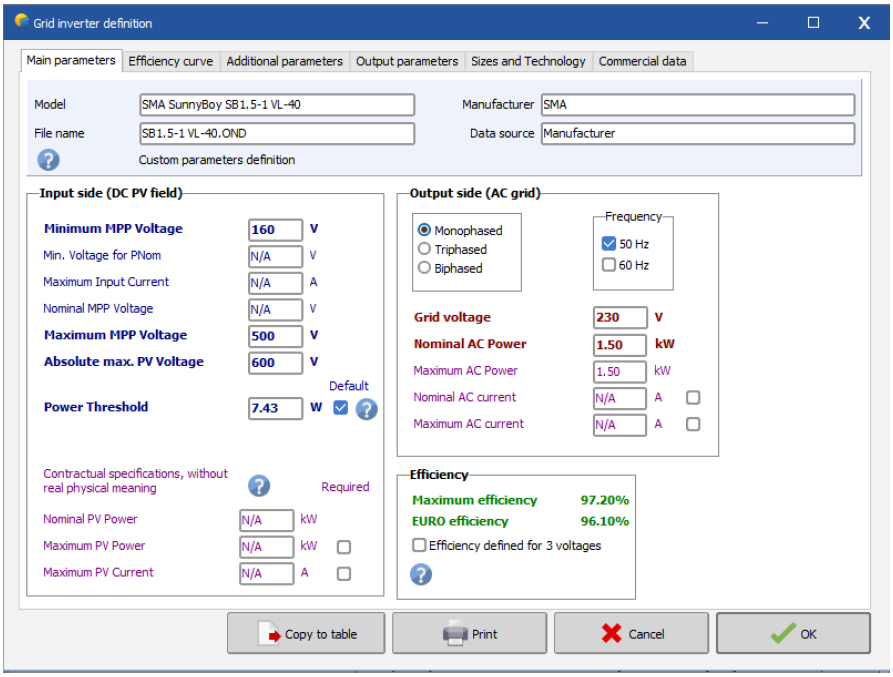

Fig. 50. Specifications of the system inverter based on information from Over Easy Solar AS and the inverter manufacturer.

After implementing the solar module technology and the inverter, we choose these technologies from the drop-down menus. We need to perform more specifications because we have a bifacial module. An additional tab named “bifacial system” appears when we choose

the PV modules, as shown in Fig. 52. Fig. 51 shows our inputs in this tab, where the 2D model we created in the system's orientation accounts for shading and reflected solar radiation to the rear side. When we save these settings, the bifacial module button in the definition of the system turns green.

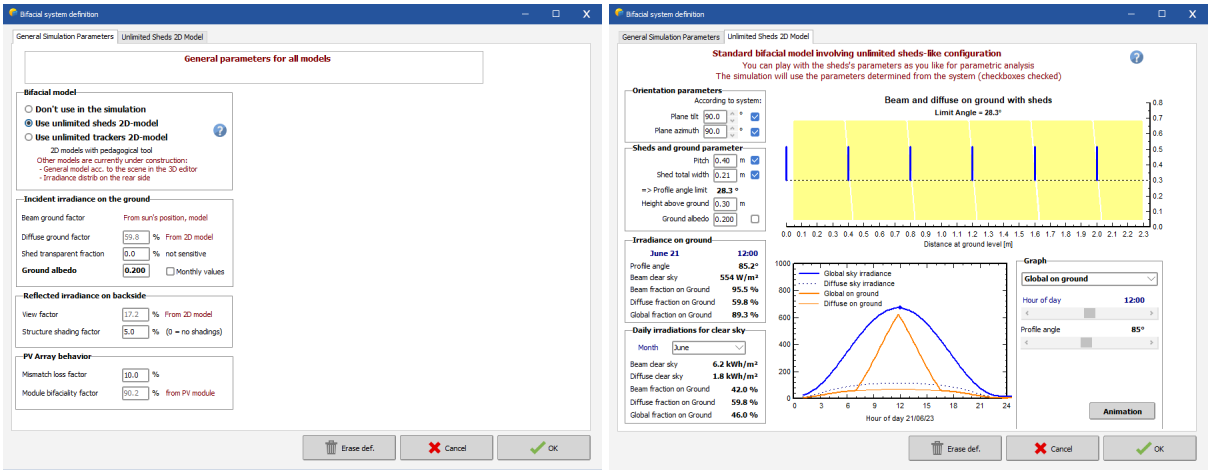

Fig. 51. The definition of the bifacial system.

We proceed with defining the sub-arrays of the system. The system is only a prototype system, so it is small. We register it as one string consisting of 42 modules connected in series. We can see a composed description of the system within the PVSyst software in Fig. 52.

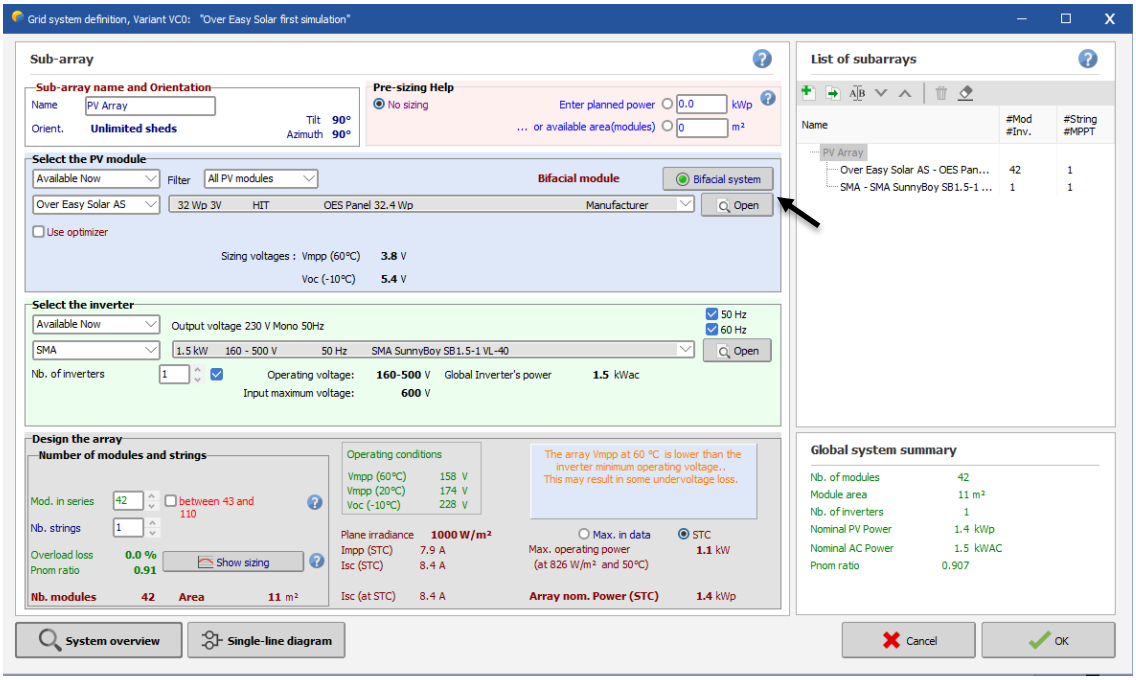

Fig. 52. The definition of the OES system in PVSyst software.

Next, we need to define the horizon. We import a horizon profile for the installation site from the PVGIS website API [77]. The PVSyst software has the PVGIS website API integrated. We use horizon profiles from PVGIS because researchers widely use them in the industry. Fig. 53 shows the sun paths of the site in a year and the imported horizon. In addition, we see that the self-shading for the system, calculated from the 2D unlimited sheds model, is visible as the stapled lines.

We register that some complications arise because the simulation only accounts for self-shading from the front side of the system, which is a weakness of the model. The PVSyst shading analysis assumes a monofacial module and does not consider the modules' backside. However, the shading of the rear side is somewhat accounted for in the backside irradiance calculations [78]. PVSyst also uses different models for calculating the front and rear sides of the solar module, which could make sense for regular tilted bifacial modules. However, this is a disadvantage for East-West-facing vertical bifacial solar modules, which are identical on both sides. The software may not capture the shading accurately. Therefore, the results could be inaccurate compared to the actual system.

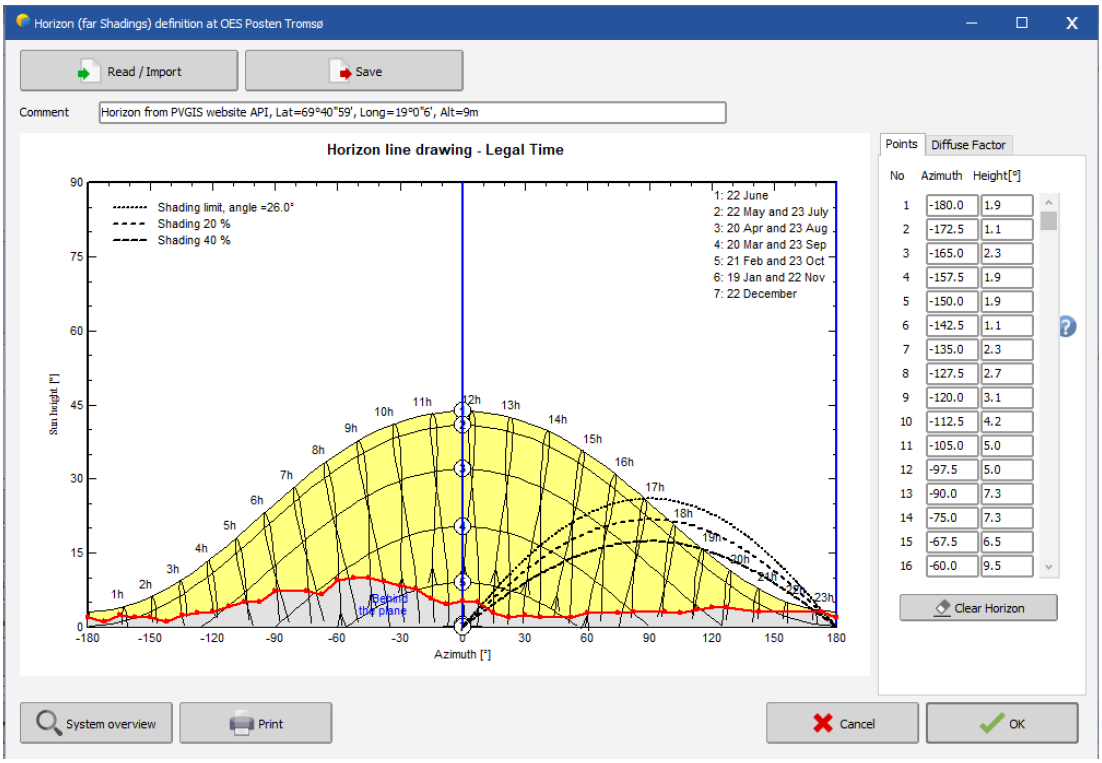

Fig. 53. Horizon line drawing and shading masks of the front of the system in PVSyst.

We will not make a 3D model of the system to account for near shadings because of the complexity and time-consuming nature of creating one, and no completed model was available. We acknowledge that adding a 3D model would improve the accuracy of the simulation. However, the 2D PV system field accounts for the self-shading of the system, which we consider the most important one. It is the most important one because the system is installed on a rooftop with few nearby sources of shading, as shown in Fig. 28.

We set the albedo at a constant value of 0.2 for the duration of the simulation, which is the default value in the software. In addition, we set the soiling losses to zero. We set these values because we do not want the models to account for the effect of snow, including both an increased ground albedo and soiling losses caused by snow cover. The period before the snow accumulation begins should validate the simulation results, and we can then try to quantify the net effect of snow on the system production.
Finally, we run the simulation and extract production and solar radiation data with hourly, daily, and monthly resolutions. We explain the exact data that we extract in section 0.

4.2.2 Modeling the ILP system

Now we want to model the ILP system. We start by implementing geographical and meteorological data. Similar to the OES system, we will perform two simulation variants, but the only parameter that separates them is the meteorological data. Therefore, we present the difference between the simulation variants first. Then, the rest of the implementation is identical for the two variants, and we will thus only present it once.

Both variants use the geographical data illustrated in Fig. 54. The first simulation uses the meteorology data file imported from the NASA-SSE external source named “NASA-SSE satellite data 1983-2005”, while the second variant uses the clear sky meteorological file shown in Fig. 46, with a Linke turbidity factor of 2.8. We use identical meteorology files in the simulations of both systems to keep as many factors as possible similar, and we have explained the reason for using these files in modeling the OES system.

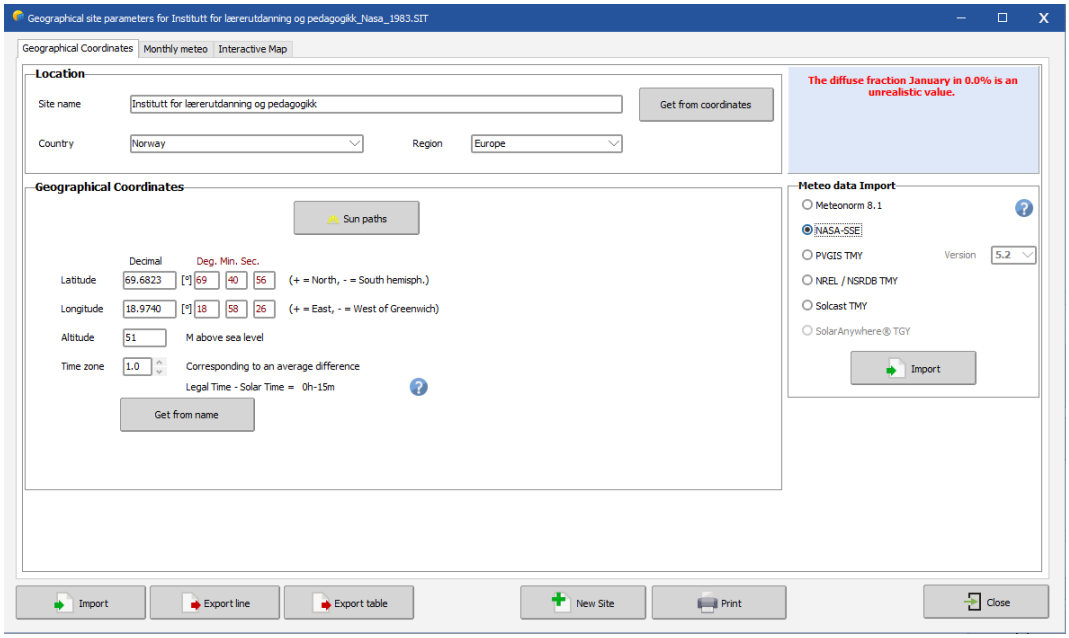

Fig. 54. Implementing the geographical and meteorological data.

The next step is to input the orientation of the system. We choose the field type “several orientations” because the ILP system has four orientations of the solar modules. We set the tilt angle at 10° for all the module orientations and input the azimuth of each direction, as Fig. 55 illustrates.

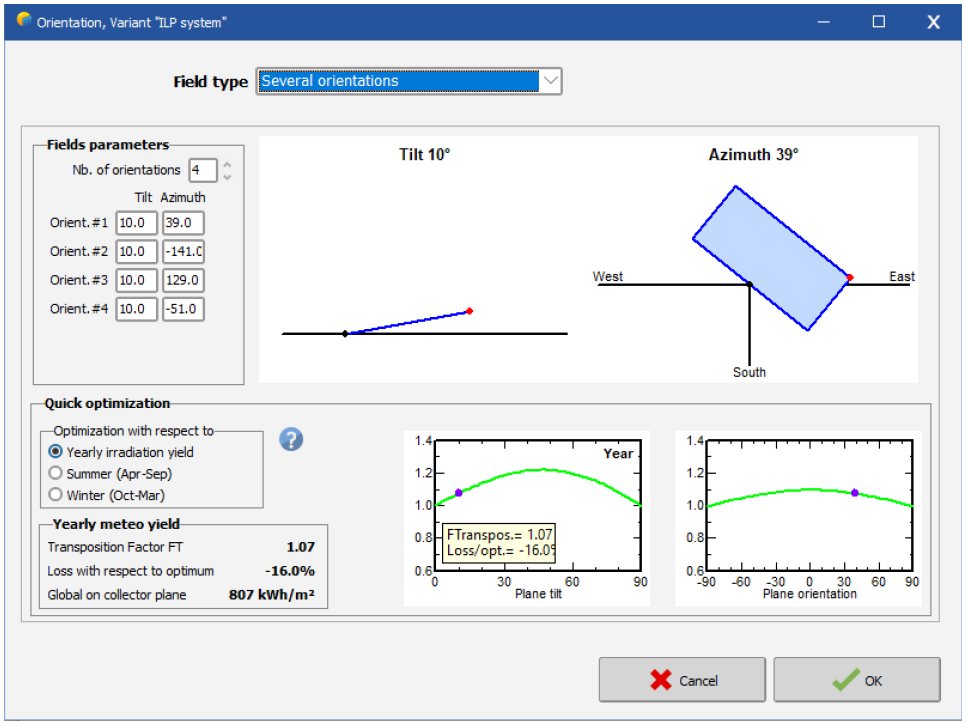

Fig. 55. The orientations of the solar modules in PVSyst.

Now, we need to design the system. The software database already has implemented the correct solar module and inverter technologies, so we choose these technologies from the drop-down menus. The next step is to define the sub-arrays, and we need to design each of them separately. Solbes AS provided access to a previous simulation report of the system, which showed the distribution of the system into seven sub-arrays based on their placement on the roof and their orientations. Thus, we divide the system into seven sub-arrays by adding each subarray to the list of subarrays on the right in Fig. 56 and modifying each, as shown in Table VI, with the total number of modules adding up to 720.

TABLE VI

THE SUBARRAYS WITH ORIENTATIONS AND NUMBER OF SOLAR MODULES

Sub-array	**Orientation (azimuth)**	**Number of modules**
Array #1 SOUTH	39°	36 (1 string of 36 modules)
Array #2 SOUTH	39°	38 (1 string of 38 modules)
Array #3 NORTH	-141°	36 (1 string of 36 modules)
Array #4 NORTH	-141°	38 (1 string of 38 modules)
Array #5 WEST	129°	190 (5 strings of 38 modules)
Array #6 WEST	129°	40 (1 string of 40 modules)
Array #7 EAST	-51°	342 (9 strings of 38 modules)

As for the choice of inverters, we use the correct inverter technology from the correct producer. However, we use a higher number of inverters in the simulation compared to the existing system. The larger inverters installed in the real system are composed of multiple smaller inverters, and the fact that we register them as multiple smaller ones rather than two large ones will not affect the simulation results. Solbes AS, the installer of the system, clarified this. We perform it this way for simplicity in the simulation. Fig. 56 shows a composed description of the system within the PVSyst software.

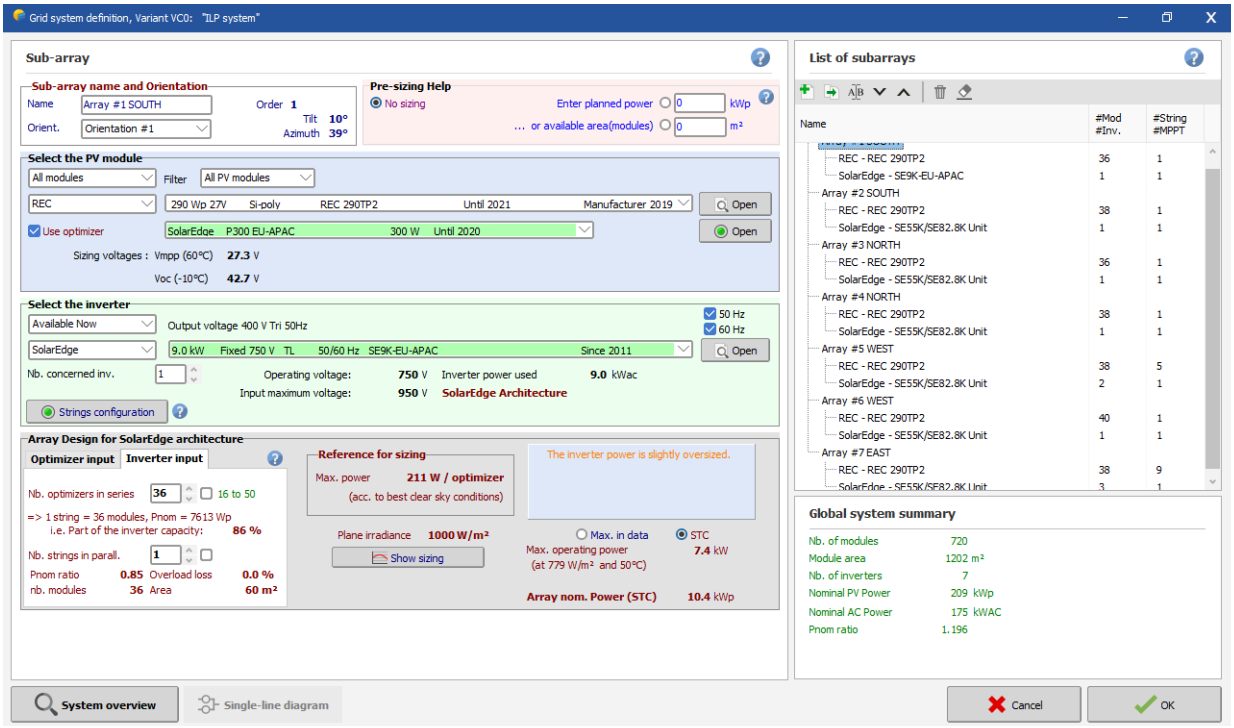

Fig. 56. The definition of the ILP system in the PVSyst software.

Now, we need to define the horizon. Like the OES system, we import the horizon from the PVGIS website API [77]. Fig. 57 shows the sun paths of the site in a year and the imported horizon profile.

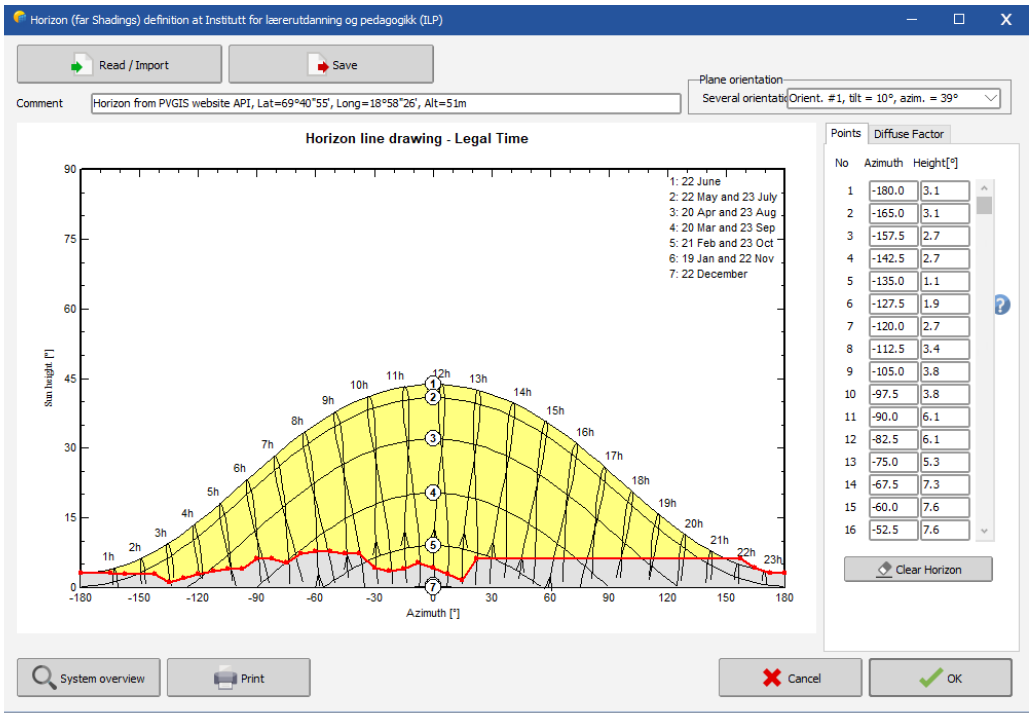

Fig. 57. Horizon line drawing of the system and the sun paths.

We will import an existing 3D shadings scene of the building and the ILP system. We expect shadings from the building to have a significant effect on the system production due to the various roof heights, and we thus find it important to include a 3D model. Fortunately, Solbes AS has already created a model of the PV field and the surrounding shading scene and provided access to it. We import it into the PVSyst software. Fig. 58 and Fig. 59 show the 3D representation of the PV field and surrounding shading scene and how it is linked with the system's orientation, respectively. The software then uses the 3D model to estimate the effect of shading on the system's energy production.

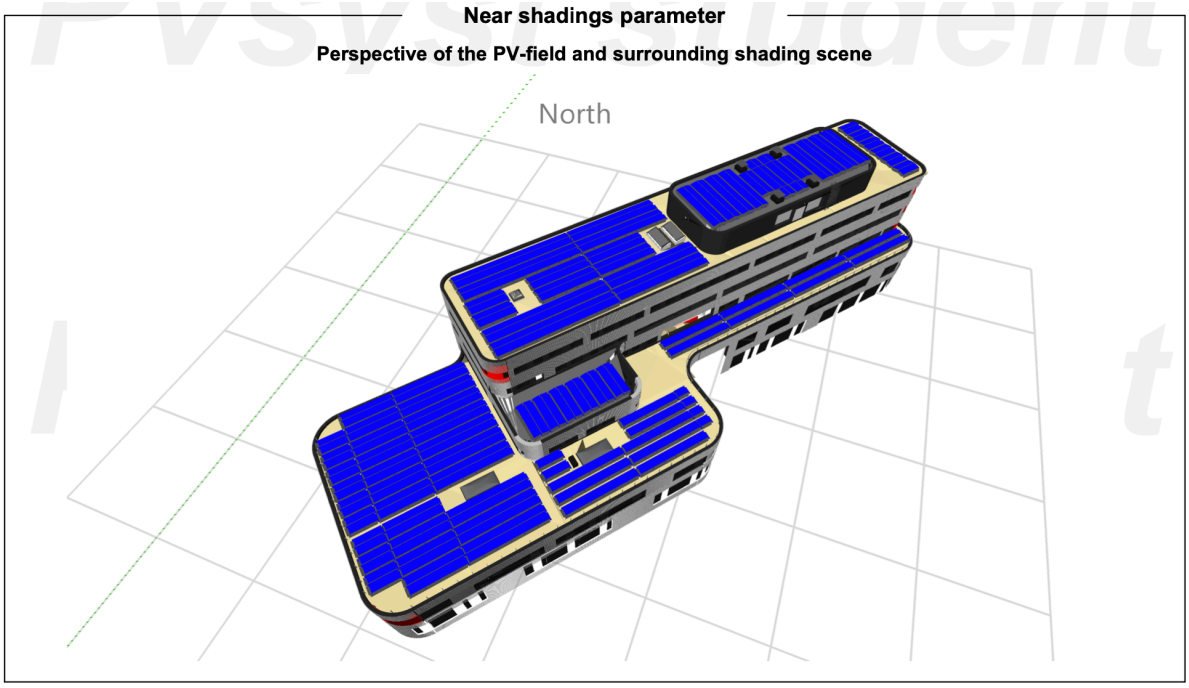

Fig. 58. The perspective of the PV field and surrounding shading scene in the software. Solbes AS created the 3D shading scene. Used with permission.

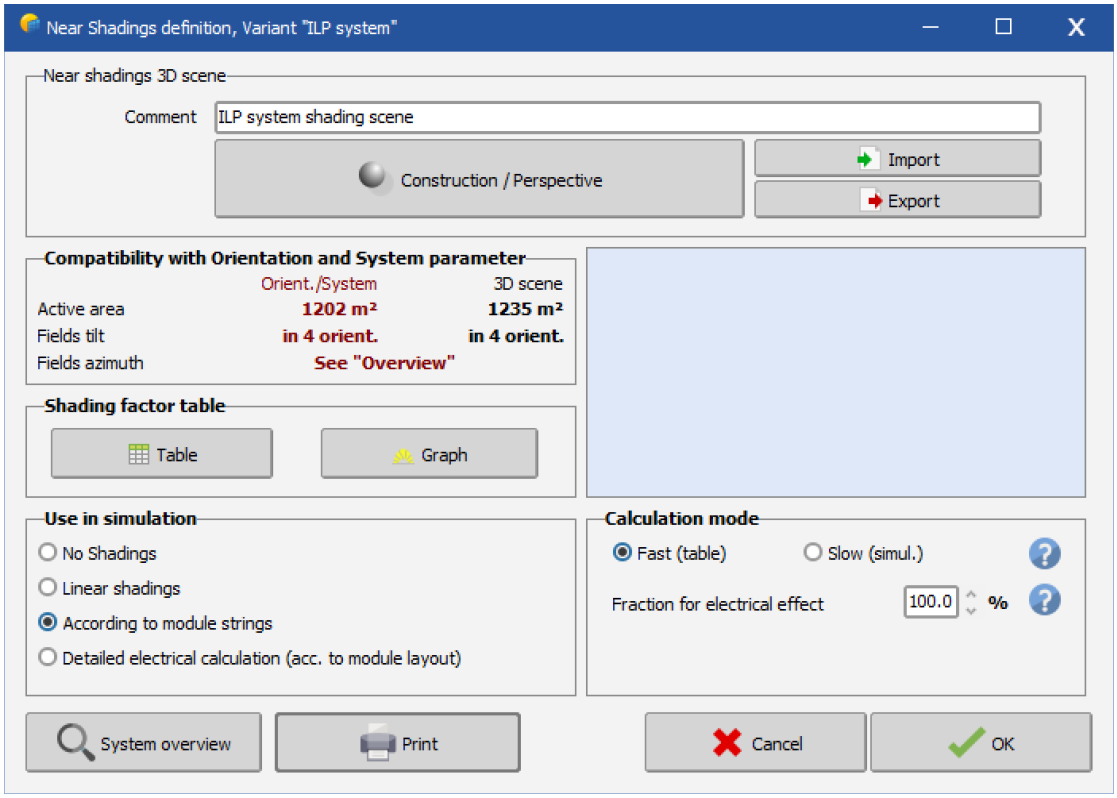

Fig. 59. Near shadings definition linking the orientation of the system and the 3D scene of the system.

Similar to the OES system, we set the albedo at a constant value of 0.2 for the duration of the simulation, which is the default value in the software. In addition, we set the soiling losses to zero for the same reasons as for the OES system.

Finally, we run the simulation and extract production and solar radiation data with hourly, daily, and monthly resolutions. We explain the exact data that we extract in the next section.

4.2.3 Simulation data

Upon completion of the simulations, we can access data from a full-year simulation and a simulation report. We create output files for the TMY and clear sky simulations for both systems with hourly, daily, and monthly resolutions. This results in twelve datasets based on the simulations, illustrated in Table VII.

TABLE VII

THE TWELVE DATASETS CREATED FROM SIMULATION RESULTS

Dataset number(s)	Simulation system	Simulation variant	Resolution(s)
1, 2, 3	OES system	TMY	Hourly, daily, monthly
4, 5, 6	OES system	Clear sky	Hourly, daily, monthly
7, 8, 9	ILP system	TMY	Hourly, daily, monthly
10, 11, 12	ILP system	Clear sky	Hourly, daily, monthly

We extract only the variables we are interested in from the software. We include the variables in all the datasets:

- Global Horizontal Irradiance (GHI) for hourly resolution data / Global horizontal irradiation for daily and monthly resolution data – "*GlobHor"* variable.
- The effective energy output of the system – "*EArray"* variable.
- The effective global energy incident on the collectors after all optical losses (including shading) – "*GlobEff"* variable.

For the OES system, we extract an additional variable provided for bifacial modules:

- Global irradiance on the rear side of the modules – "*GlobBak"* variable.

We will use these variables in the data analysis and explain how we use them in section 0.

4.3 Actual energy production data

We collect the production data from the systems from the solar monitoring systems Sunny Portal and SolarEdge. These monitoring systems operate through the inverters of solar photovoltaic systems. They collect power levels and energy production from the inverters and power optimizers and send them to cloud-based monitoring systems, where we can access and download the data.

Over Easy Solar AS provided access to the production data from the OES system via the Sunny Portal monitoring system. They own the production data from this system. Individuals must contact the company directly and request permission to access the data. The data is available on the inverter (system) level and is extracted from June 28, 2022, to April 30, 2023. We include data from June 28 because we want to investigate further the performance of this system since its commission. However, due to a gap in production data between August 18 and August 30, 2022, we exclude these dates from the analysis. We extract monthly data separately for 2022 and 2023 and manually merge them into one dataset. Furthermore, we extract the daily data on a month-by-month basis and manually merge these into a single dataset. With the Sunny Portal professional package (analysis pro), data with a 5-minute resolution is available every week. We obtain this data separately every week of the research before manually joining the files in CSV format.

The low-resolution data of the OES system only reports power generation, not energy production. For this reason, we calculate the hourly energy production manually from the 5-minute power generation reports. We calculate an approximation of the hourly energy production for every hour in the research period using the equation:

$$E_{(kWh)} = \frac{\sum P_{5min}}{N} \times 1\ hr \qquad (4.1)$$

P_{5min} represents the power generation every 5 minutes, and N represents the number of non-zero power generation values in the hour. We set the energy production to zero in an hour of zero power generation.

Statsbygg and Solbes AS provided access to the production data of the ILP system via the SolarEdge monitoring system. Individuals must contact the companies directly and request

permission to access the data. This system's data is available on module, string, inverter, and system levels. We extract data on the system level with hourly, daily, and monthly resolutions from September 20, 2022, to April 30, 2023. We do not include data before September 20 for this system because of an issue with the production reports of the systems. We elaborate on the production issues in section 0. Energy production data with these resolutions is easily accessible and we export it directly from the SolarEdge monitoring platform in CSV format. However, the hourly production data is only available for daytime hours. Consequently, we manually expand the dataset to include all hours of the period for comparison purposes. Night-time production values are all manually set to zero.

Table VIII summarizes the datasets containing the actual energy production of the systems.

TABLE VIII

THE SOLAR PHOTOVOLTAIC SYSTEM ENERGY PRODUCTION DATASETS

Dataset number(s)	**Dataset**	**Resolution(s)**	**Owner(s)**
13, 14, 15	OES production data	Hourly, daily, monthly	Over Easy Solar AS
16, 17, 18	ILP production data	Hourly, daily, monthly	Statsbygg, Solbes AS

4.4 Visual observation data

We collect visual observation data from a local Reolink camera at each site, accessible via their app. We have mounted cameras in each system's proximity to track the snow cover on the solar modules and their environment. Fig. 60 illustrates the camera setup, and the camera view for both systems is visible in Fig. 61 and Fig. 62.

The purpose is to monitor the snow cover on the solar modules and the roof. With help from Over Easy Solar AS, we have saved snapshots from each camera with an uneven interval, but approximately once a week starting at the time of installation. The original intention was to use the pictures to quantify the snow cover on the systems for the entire research period. However, the uneven interval of the pictures made it difficult. Instead, the primary use of the cameras in this research is to extract pictures at various points in the research period to illustrate the properties of each system in winter conditions.

Fig. 60. Cameras mounted adjacent to the OES and ILP systems.

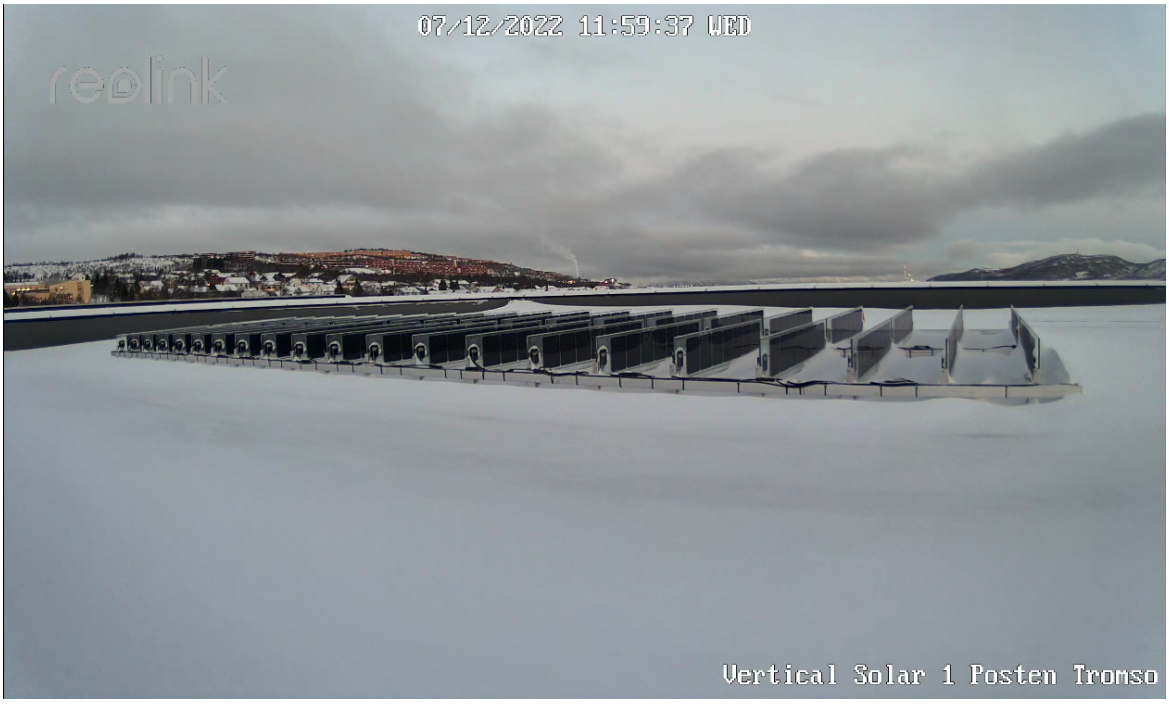

Fig. 61. Camera view of the OES system on a day in December with snow cover on the roof.

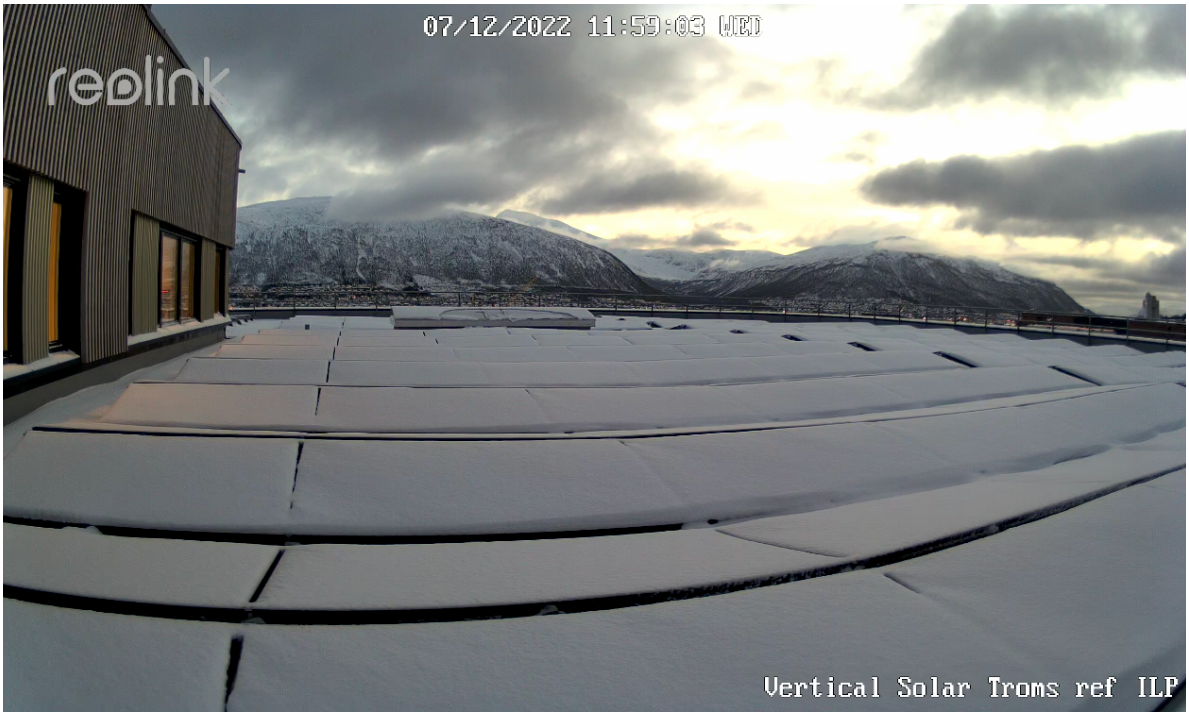

Fig. 62. Camera view of the ILP system on a day in December with fully snow-covered modules.

4.5 Data analysis

First, we want to investigate the weather in the research period compared to the historical average in the past decade. We do this because we want to know if we can expect the observed performance trends to be typical of the period or if the weather factors influence the systems more or less heavily than usual. These results constitute the first part of the results chapter. We state the data source of the weather data with the results.

We collect Global Horizontal Irradiance (in W/m^2) data from the TMY and clear sky simulations with the hourly resolution. We average the hourly values to find the average daily, monthly, and annual values of the GHI, including nights, for both the TMY and clear sky simulations. The meteorology file contains these values, which are thus identical for both systems. To estimate solar irradiation, we use the equation:

$$G_{day}(kWh/m^2) = \frac{\sum_{i=1}^{24} I_{hr}(i) * 1\ hr}{1000} \qquad (4.2)$$

G_{day} is the daily global horizontal irradiation, and I_{hr} is the hourly GHI in W/m^2. We want to look at these values to extract key data on the differences in solar irradiance and irradiation between the TMY and clear sky simulations to quantify the expected decrease in these variables due to weather. We do this for both simulations and perform similar calculations to find the average monthly and annual irradiation values.

We will calculate all energy performance metrics for the OES system starting June 28, 2022, even though the research period starts September 20. We do this because we have data available from this date, and this data can provide more information about how the system performs in the summer months. However, this research focuses on the period from September 20, 2022, to the end of April 2023. We will thus perform calculations starting June 28 for the OES system, but we direct the focus on the dates of the research period in the results, discussion, and conclusion. We explain why we cannot extend the research period to June 28 in the study's limitations in chapter 0.

For energy yield calculations, we use the actual production datasets directly. To estimate the industry standard value for specific yield (kWh / kW_p), we divide the energy yield by the system capacity. We further compare the energy yield of each system to the modeled energy

production in a TMY and clear sky conditions by comparing the actual production datasets to the simulation datasets. This way, we can validate that each system's expected energy yield (TMY simulation) resembles the actual energy yield. In addition, we want to see how both datasets compare to the ideal situation of the clear sky simulation.

We use the actual production datasets with hourly resolutions to estimate each system's availability (A). Only hours with non-zero energy production are available. To calculate the availability, we use the equation:

$$A = \frac{T_A}{T_T} \tag{4.3}$$

This calculation results in an availability estimate, where T_A indicates the number of hours with energy production, and T_T indicates the total operating time (in hours) of the calculation period. The calculation gives a measure of the time that the system is operational and available for power production. We perform this calculation with a monthly resolution and for the research period as a whole.

Next, we will approximate each system's performance ratio (PR) monthly and for the entire research period. For this calculation, we divide the actual energy yield by the expected theoretical output under ideal conditions. We use the equation:

$$PR = \frac{E_A}{E_T} \tag{4.4}$$

E_A corresponds to the actual energy yield of the system, and E_T corresponds to the expected theoretical output under ideal conditions. We base the calculation of the expected theoretical output under ideal conditions on the definition of Solar Mango [79]. Therefore, we approximate it as the product of the global incident irradiation on the collectors, the active area of the PV modules, and the PV module efficiency.

Due to the different technologies of the systems, we use different approaches to these calculations. Both systems use the energy yield in the calculations, but the global incident irradiation on the collectors varies. For the ILP system, consisting of monofacial technology

solar cells, we use the PVSyst variable *GlobEff*. We collect this variable from the clear sky simulation dataset of the system because we want the theoretical output under ideal conditions. Another option could have been to use the data from the TMY simulations, resulting in a weather-corrected performance ratio. However, we use the regular performance ratio and keep it similar for both systems. Next, we multiply the *GlobEff* variable by the active area of the PV modules and the PV module efficiency. These calculations result in an approximated performance ratio of the monofacial ILP system.

In contrast, the OES system utilizes bifacial technology solar cells. While *GlobEff* denotes the incident energy on the front side collectors, we must include the incident energy on the rear side. We thus also utilize the *GlobBak* variable. We collect both of these variables from the clear sky simulation dataset of the system. To find the usable irradiance of the rear side, we multiply the *GlobBak* variable by the bifaciality of the solar modules. With these variables, we approximate the expected theoretical output under ideal conditions by adding the product of the *GlobEff* variable, the front surface area, and the PV module efficiency to the product of the *GlobBak* variable, the bifaciality, the rear surface area, and the PV module efficiency. These calculations result in an approximated performance ratio of the bifacial OES system.

Lastly, we further use the actual energy yield of the systems to approximate their capacity factors (CF), where we use the equation:

$$CF = \frac{E_A}{C \times T} \qquad (4.5)$$

In this equation, E_A denotes the actual energy yield of the system, C indicates the system capacity in kilowatts, and T denotes the period in hours. This calculation results in a ratio of the actual production to the theoretical maximum output, assuming that the system operates at its rated capacity every hour of the period. Similar to the performance ratio, we calculate the capacity factor for every month as well as the entirety of the research period.

We calculate the performance metrics for each system individually, but we will also use them to compare the system performances in section 6.7.

4.6 Expected variations in system performances

We anticipate the vertically installed bifacial system (OES) and 10°-tilted monofacial system (ILP) to have varying performances during the research period between September and April as the sun and weather conditions change. During the research period, when the sun is low on the horizon, the bifacial system can take advantage of the reflected light from the ground and nearby surfaces to enhance the absorption of solar radiation. Additionally, the bifacial system has better absorption of diffuse radiation due to its bifaciality and tilt angle. In contrast, the design of the monofacial system primarily aims to absorb direct radiation from the sun.

These properties give the systems different strengths related to the available type of radiation. The bifacial system is advantaged on clear weather days as it captures direct, diffuse, and reflected radiation. In contrast, the monofacial system primarily absorbs direct radiation and may receive less direct radiation due to its low tilt angle and low solar altitude in the research period. These characteristics should cause the bifacial system to perform better because it can capture more available solar radiation. In contrast, on cloudy days, the reflected sunlight is significantly reduced, thus reducing the advantage of the bifacial solar cells. Depending on the concentration of clouds, parts of the direct sunlight still reach the ground, and both systems can take advantage of it.

Overall, we expect the OES to perform better than the monofacial system in the research period due to its ability to capture more available solar radiation, including direct, diffuse and reflected radiation. We expect the bifacial system to perform better on clear weather days, while on cloudy days, the performances should be more comparable.

Snow is another crucial factor, and we expect it to affect the systems unevenly due to the different module tilts and system designs. Generally, snow can bury roof-mounted solar photovoltaic systems, independent of a vertical or horizontal installation. The OES and ILP systems are 23.8 cm and 24.7 cm tall, respectively, meaning that such a snow depth would completely cover the system. However, a significant difference between the systems is that snow can easily accumulate on the surface of the ILP cells due to its low tilt, long before the snow depth reaches the system’s height, and snowfall can quickly cover the entire system. For the OES system, on the other hand, the vertical installation reduces the ability of snow to accumulate on the cell surfaces.

An accumulated layer of snow can persist for an extended period without human intervention. Solar cells generate heat when absorbing solar radiation, and bifacial cells have an advantage in this regard, as they absorb solar radiation from both sides, generating more heat and melting surrounding snow faster. However, the monofacial solar cells in the ILP system can be entirely covered by snow after a snowfall, thus rapidly reducing the generation of heat in the solar cells. As a result, an accumulated layer of snow can remain in place for a long time.

In contrast, snow will almost only cover the OES cells when the roof snow cover reaches the bottom of the cells since the snow cannot accumulate on the vertically installed modules. When the snow does reach the bottom of the cells, they experience partial shading, which causes significant power reduction, but the bypass diodes ensure that energy production continues. As a result of the solar cells still generating power, heat is generated in them, causing the snow to melt faster. Therefore, the OES system has an additional advantage in snowy conditions, providing another reason why it should perform better in periods of snow.

Considering the snowy conditions, we anticipate that the ILP system's energy yield will be significantly impacted by snowfall, with a substantial portion of the research period seeing the system covered in snow. On the other hand, we expect the OES system to be less affected by snow, where light snowfalls should not have a decisive impact on system production. However, the increased albedo on the roof could enhance system production. Nonetheless, if snow accumulates substantially, we anticipate drastically reduced energy yields for both systems.

Both systems are mounted on roofs, increasing the comparisons' relevance. Even though we can correlate the snow load on roofs to the ground snow depth, there usually is less snow accumulation on roofs for various reasons. These include heating from the building interior and increased wind and sun exposure, melting the snow faster. However, as mentioned, we expect the snow to melt faster around the OES system than the ILP system.

Due to variations in typical wind conditions, certain parts of roofs are more prone to snow accumulation. The OES system is relatively small compared to the ILP system. Over Easy Solar has purposely placed the system on a part of the roof where there, by experience, has been the lowest accumulation of snow in the winter. The ILP system, on the other hand, is installed in great capacity and covers (almost) the entirety of the roof. The OES system aims

to avoid the parts of the roof with the most considerable accumulation of snow, while the ILP system will naturally have some modules with a thicker snow cover than others. Snow cover's negative effect could be more prominent for the ILP system.

As a result of the proximity of the systems, we expect the weather to have a similar effect on the energy production of both systems. There may be some local differences, but if one system experiences a lasting cloud cover, so will the other. The systems should hence experience a similar solar irradiance. For this reason, we anticipate the energy yields of the systems to follow the same patterns. However, due to the difference in capacities, the energy yield of the ILP system will naturally be significantly higher. On the other hand, we expect the OES system to have a higher specific yield in the winter months due to its ability to take advantage of the long hours of low solar elevation and increased absorption of reflected radiation on both the front and rear sides of the modules.

The polar night period lasts from November to January, where the available usable solar radiation is insignificant. During this time, we do not expect any systems to produce a significant amount of energy.

5 Limitations and uncertainty

Before we look at the results of the data analysis, we must address the limitations and uncertainties of the research.

First, we should ideally place the systems side-by-side to ensure they experience similar weather conditions, shading, solar irradiance, and snow accumulation. This action would improve the accuracy of direct comparisons. Ensuring that all external factors remain the same for both systems would strengthen the results.

Now, we consider the actual production data collected from the monitoring systems. This data can have deviations from the actual values. The SolarEdge monitoring system reports a measurement accuracy of $\pm$ 2.5% for direct measurements, such as voltage and current [80]. The value of these measurements may hence deviate up to 2.5 % from their actual value. Variables like energy, however, are calculated from the product of other direct measurements. These variables have a measurement accuracy of $\pm$ 5%.

On the other hand, SMA (Sunny Portal owner) reports a measurement accuracy of $\pm$ 1% for voltage and current measurements and $\pm$ 2% for power measurements [81]. These values lead to a possible $\pm$ 5% and $\pm$ 2% deviation in power production reports for the ILP and OES systems, respectively. Differences in measurement accuracies can lead to misinterpretations of the results.

Further uncertainties exist in the production data, and we highlight the manual merging of CSV files. With human input of data follows uncertainties such as data entry errors (typos or incorrect values), inconsistent formatting, and the handling of gaps in the missing data. The actual production datasets with both hourly and daily resolutions had gaps. We exclude the missing data from the analysis. Errors in the merging could propagate through the analysis and lead to incorrect results or biases.

A significant limitation of the data analysis is the limited duration of data collection. The production reports from the ILP system have been unreliable for a significant part of 2022, as confirmed by Solbes, the system's installer. There was unstable communication with the inverters. The result is that data for much of 2022 is unreliable, and we cannot use it in the

data analysis. Therefore, we only use data generated starting September 20, 2022, from the ILP system in the data analysis. We have compared the data from September 20 to previous years of production as a validity check, and the research reports in the research period look realistic. In addition, Statsbygg reached out and stated that they had indications that they had resolved the issue. We see a significant change in the production reports starting from this date, suggesting that it is true. Therefore, we choose to use the data from September 20 in the analysis. However, we acknowledge that if the problem persists, albeit to a much smaller extent, there could be some errors in the data. If this is the case, it will lead to incorrect results. Therefore, unreliable production reports bring uncertainty.

Ideally, we would use data from a full year (or multiple years) to accurately represent the full-year performance of each system. However, such data is unfortunately not available. The issue on the production reports limits the ILP system, while the OES system only has available data from the end of June 2022, which makes the analysis short of an entire year.

We associate several uncertainties with the simulation data. First of all, according to the PVSyst documentation, the accuracy of the simulations is typically within 5-10% of the actual system production, assuming that the system input data is correct [82]. The parameters input by the user present the primary source of uncertainty. For example, the quality and accuracy of our weather data can significantly affect the results. The “NASA-SSE satellite data 1983-2005” file can contain measurement errors or data gaps. The file has an RMS (root-mean-square) error of around 13-16 %, and the MBE (mean bias error) is between -2 % and +0.7 % [75]. In addition, the meteorology file is a monthly averaged dataset from 1983-2005, which can cause an extrapolation error by assuming that the trends will continue. The period of 2022-2023 may not have weather representative of the area, which causes the systems to behave differently than expected. It is also worth noting that the dataset has a ground resolution of 1° x 1°. Hence, it does not differentiate between local weather phenomena on more minor scales, which could be significant in the region.

While addressing the meteorological data of the TMY simulation, we would ideally use actual historical weather data instead of the TMY simulations to improve the accuracy of performance comparisons. Furthermore, a pyranometer could be installed on each site to measure the available solar radiation accurately. Such technology was unfortunately not available at this time.

Inherent uncertainties in the module and inverter performance data could also exist. The performance data we implemented in the PVSyst system uses manufacturer specifications. Deviation from these performance data could occur in real-world conditions or specific system designs. The uncertainties in the accuracies of input data also apply to how we model system designs and configurations in PVSyst. Any errors in this input data can lead to inaccurate results of the simulations.

A significant limiting factor of the research is the ability of our solar photovoltaic systems to perform as their models. First of all, the weather data in the model is, as mentioned, a monthly averaged dataset from 1993-2005, meaning that it is not historical data from the research period. Hence, comparisons of actual production data and simulated data on a day-to-day basis are irrelevant. Instead, we can identify trends over months. We do not expect any systems to perform as the clear sky model, which we only use as a measure of an ideal world.

Furthermore, we have performed the simulations with no soiling losses and a constant albedo of 0.2. In the real world, we expect soiling losses due to sand/dust and snow cover of the modules, and the changing albedo will also affect the results. These factors limit the ability of the systems to perform as the models. The intention behind the exclusion of soiling losses and albedo changes is to investigate how the energy production of the two technologies is affected by snow.

6 Results

6.1 Comparing weather to the historical average

We start by looking at the weather in the research period compared to the historical average. Weather can significantly impact solar PV energy production, with temperature, cloud cover, and precipitation (especially snow) being the most relevant factors.

Fig. 63 compares temperature data during the research period to the historical average and its standard deviation. The data reveals that the temperature fluctuates around the average, following similar patterns, but some days experience notable deviations. Overall, the temperature during the research period aligns closely with the historical average. The consistently low temperatures in the research period should enhance the solar modules' efficiency compared to their specifications measured STC and thus enhance energy production.

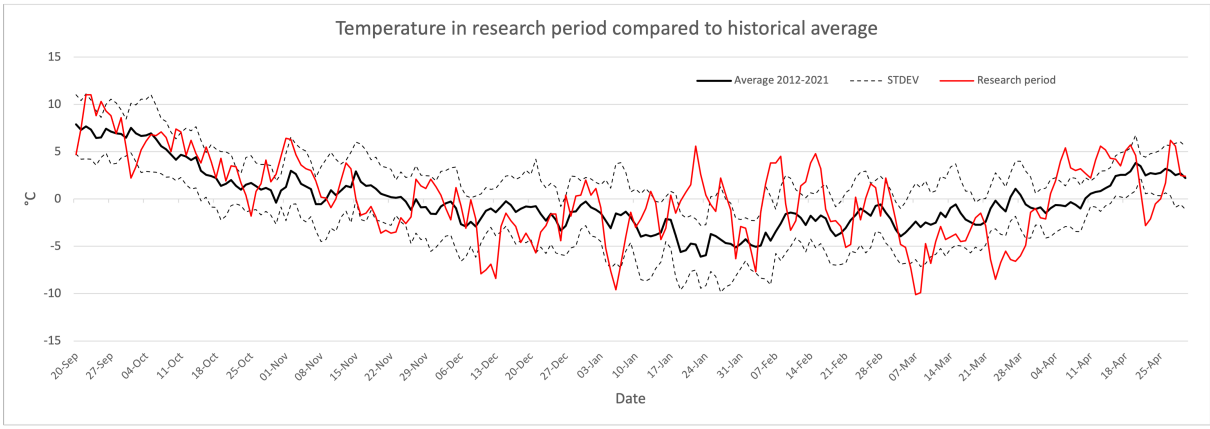

Fig. 63. Temperature in the research period compared to the historical average. Data source: https://seklima.met.no/observations/

Fig. 64 shows the cloud cover in the research period compared to the historically averaged distribution of cloud cover in the past decade. We split the cloud cover into clear (dark blue), mostly clear (light blue), partly cloudy (light grey), mostly cloudy (darker grey), and overcast (dark grey) weather. The data reveals that September, November, March, and April had higher occurrences of clear weather than historical averages, while October, January, and February had less clear skies and more cloudy and overcast weather. The weather in December appears to be typical for the season in Tromsø. These findings suggest that energy

production in October, January, and February may be lower than expected due to adverse weather conditions. In contrast, September, November, March, and April may exhibit improved energy productions.

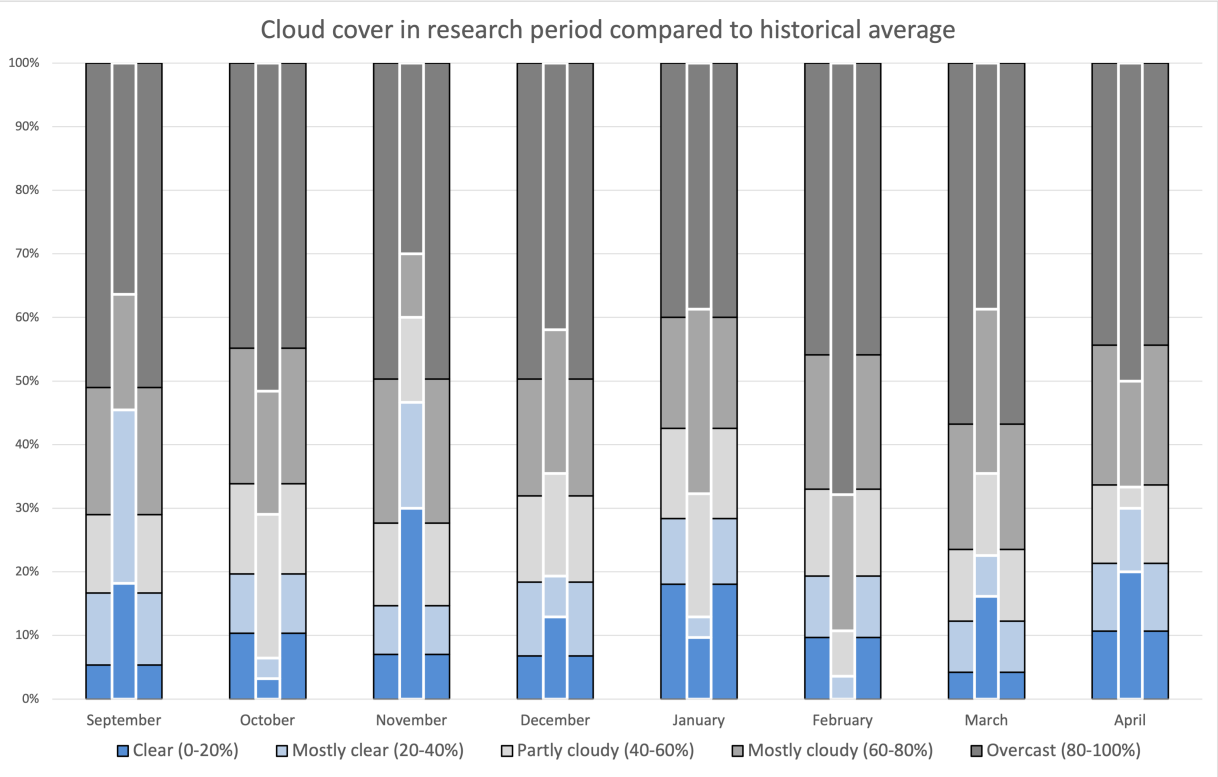

Fig. 64. Cloud cover in the research period (slim graphs in front) compared to the historically averaged cloud distribution for each month over the past decade (wide graph behind). Data source: https://seklima.met.no/observations/

Fig. 65 compares the ground snow depth during the research period to the historical average of the past decade. The results show below-average snow depth during November and early December, consistent depth from late December to the end of February, abnormally high depth from March to early April, and the remainder of April is typical of the region, with a peak in snow cover towards the end of the month falling within the standard deviation. Overall, the ground snow depth during the research period falls within the standard deviation of the average, except for the higher-than-usual snow cover from late February to the end of March. Therefore, we expect March's snow to impact the systems' performances more than it would in a typical year.

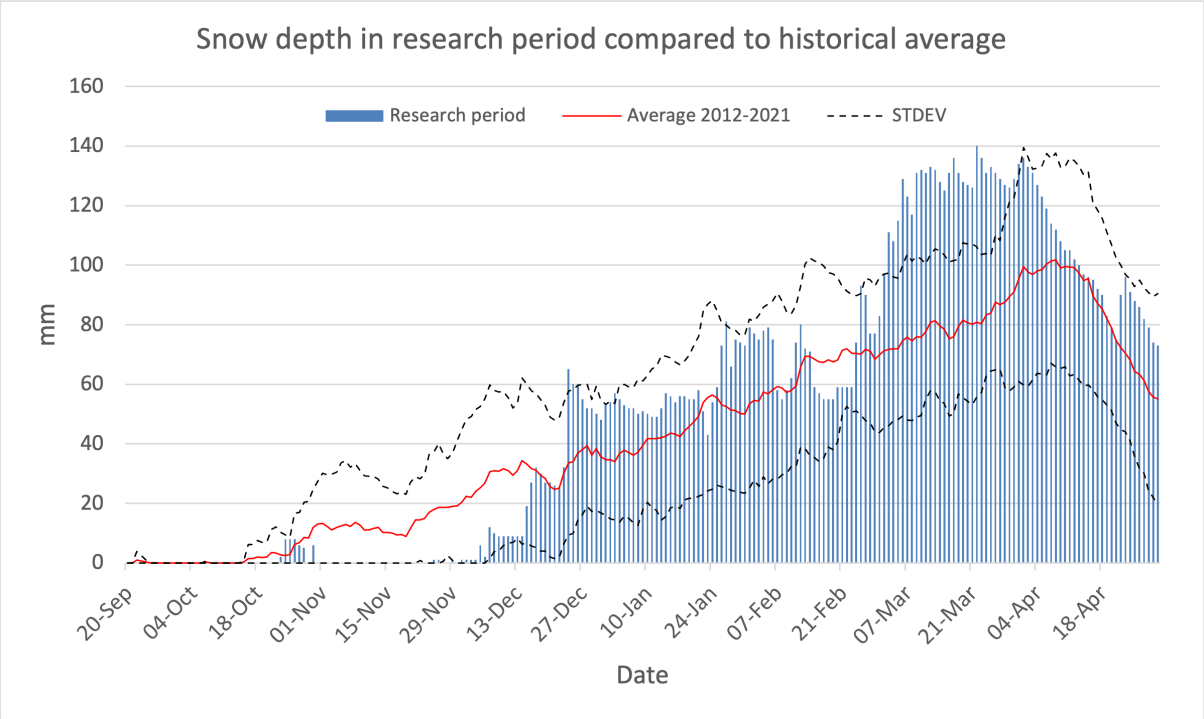

Fig. 65. Ground snow depth in Tromsø, Norway. Period of research (shown in blue) compared to the average from 2012-2022 (shown in red). Data source: https://seklima.met.no/observations/

Although the ground snow cover may vary from that on the roof, it provides insight into the timing and impact of snow on system production. Based on the snow data, we expect to see a repeating pattern when estimating the energy performance metrics that reveal a significant effect of snow in February, March, and April due to the high snow cover.

The research we conduct in Tromsø records 163 days of snow cover, falling within the expected range of 150-200 annual snow-cover days. This finding suggests that most snow-covered days occurred within the study's timeframe, and we have thus included the period with the most significant effect of snow on the energy production of the systems in a year. However, studying Fig. 8, the snow cover will likely persist for a considerable part of May despite a rapid decline.

6.2 Solar irradiance and irradiation

We look at the solar irradiance and irradiation to approximate the available solar radiation in Tromsø and estimate the effect of weather on these values. Fig. 66 and Fig. 67 illustrate the monthly and daily differences in GHI between the ideal clear sky (yellow) and TMY (gray) simulations, respectively. While Fig. 66 displays monthly averaged values, Fig. 67 emphasizes the daily fluctuations in a typical year. We attribute these fluctuations to various factors affecting the actual conditions on-site, where we expect clouds, snow, and environmental conditions such as atmospheric pressure and humidity to be the main contributors. The difference in GHI between the simulations is most pronounced during summer when irradiance levels are highest and lowest in winter.

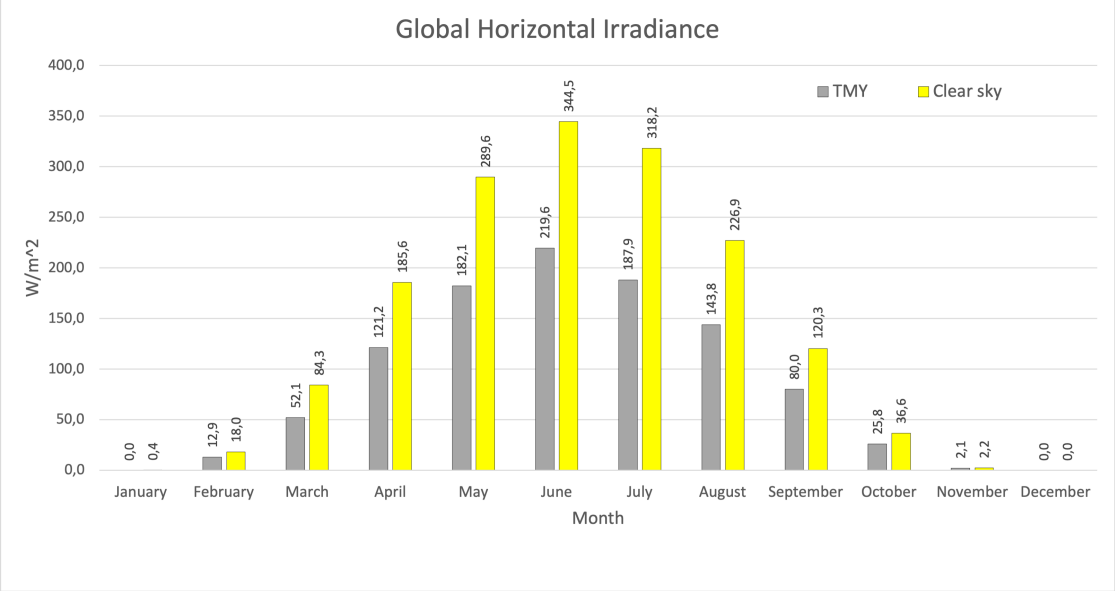

Fig. 66. Monthly Global Horizontal Irradiance (GHI) for Tromsø, Norway, including nights.

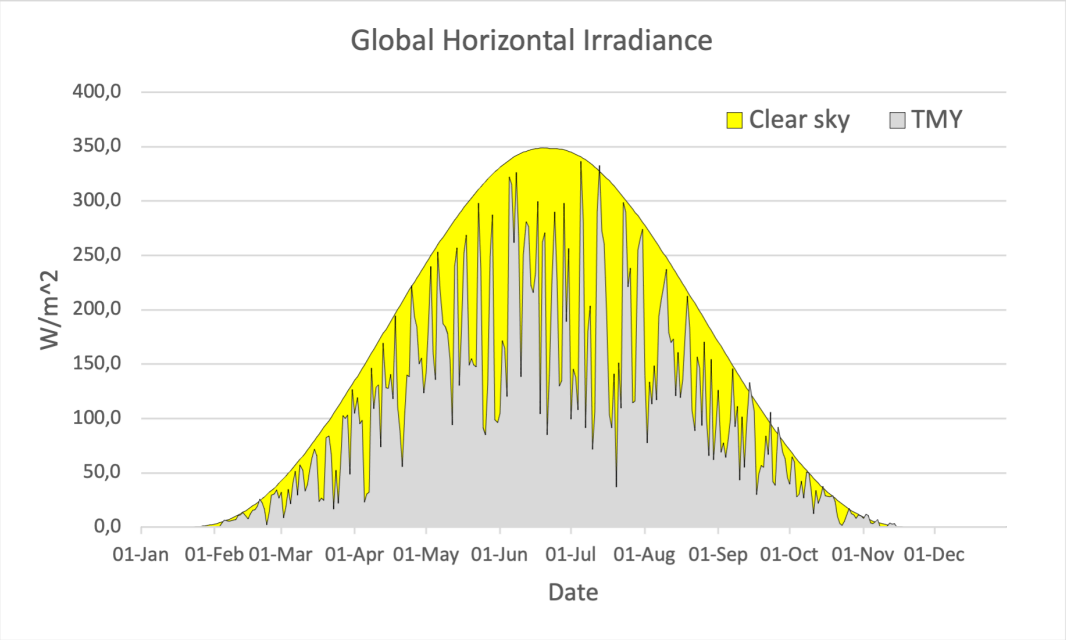

Fig. 67. Daily Global Horizontal Irradiance (GHI) values for Tromsø, Norway, including the clear sky (yellow) and TMY models (light gray).

Table IX summarizes the solar irradiance data presented in the previous figures, while Table X presents solar irradiation data. The average annual solar irradiance per hour, including nights, is estimated as 86.00 W/m^2 and 136.35 W/m^2 by the TMY and clear sky simulations, respectively, while the annual solar irradiation showed 750.42 kWh/m^2 and 1188.65 kWh/m^2. In Tromsø, weather reduced solar annual average solar irradiance and solar irradiation by almost 37%, with the most significant reduction occurring in July. Monthly reductions fell within 28-41%, except for the polar night period, which comprises November, December, and January when the irradiance is nearly zero.

TABLE IX

MONTHLY AVERAGED GLOBAL HORIZONTAL IRRADIANCE (GHI) FROM SIMULATIONS

Month	GHI (TMY) [W/m^2]	GHI (Clear sky) [W/m^2]	Ratio	Decrease
January	0.00	0.36	0.00	100.00%
February	12.92	18.00	0.72	28.26%
March	52.08	84.25	0.62	38.18%
April	121.18	185.62	0.65	34.72%
May	182.09	289.56	0.63	37.11%
June	219.59	344.48	0.64	36.26%
July	187.90	318.16	0.59	40.94%
August	143.75	226.92	0.63	36.65%
September	80.00	120.33	0.66	33.52%
October	25.83	36.56	0.71	29.35%
November	2.08	2.17	0.96	4.21%
December	0.00	0.00	1.00	0.00%
Total	**86.00**	**136.35**	**0.63**	**36.92%**

TABLE X

GLOBAL HORIZONTAL IRRADIATION DATA FROM SIMULATIONS

Month	Global horizontal irradiation (TMY) [kWh/m^2]	Global horizontal irradiation (clear sky) [kWh/m^2]	Ratio	Loss
January	0.00	0.27	0.00	100.00%
February	8.68	12.10	0.72	28.26%
March	38.75	62.68	0.62	38.18%
April	84.34	129.19	0.65	34.72%
May	135.48	215.43	0.63	37.11%
June	158.10	248.03	0.64	36.26%
July	139.80	236.71	0.59	40.94%
August	106.95	168.83	0.63	36.65%
September	57.60	86.64	0.66	33.52%
October	19.22	27.20	0.71	29.35%
November	1.50	1.57	0.96	4.21%
December	0.00	0.00	1.00	0.00%
Total	**750.42**	**1188.65**	**0.63**	**36.87%**

The values in the TMY model prediction are consistent with the expected values of global horizontal irradiation and the global average annual solar irradiance that we estimated in Fig. 13 and Fig. 14. We estimated them as 700-750 kWh/m^2 and 50-100 W/m^2, while the TMY model estimates them as 750 kWh/m^2 and 86 W/m^2, respectively. These results strengthen the credibility of the meteorology file we used in the TMY simulations.

The research period from late September to the end of April coincides with the period of the year when the solar irradiation levels are typically the lowest. This period corresponds to fall, winter, and spring, with the lowest solar altitude and the shortest days. Only 22.7 % of the total yearly solar irradiation in a TMY falls within the research period, indicating that the system performances in the research period can only be representative for part of the year, as the solar irradiation levels for the other months differ significantly from those observed during the research period. In particular, November, December, and January have limited usable irradiance, which implies that we should expect a low energy yield from solar photovoltaic systems.

6.3 Energy yield and specific yield

6.3.1 OES system

Table XI presents the energy yield data we obtained from actual observations and both simulations for the OES system. The rows starting from the first yellow one indicate the research period from September 20. In a TMY, the simulations predict that the system will produce 61.5% of the energy yield under ideal conditions in the research period, which decreases to 56.9% if we extend the period to the commission date. However, the actual energy yield of the system during the research period only corresponds to 84.3% of the simulated energy yield in a TMY and 94.7% from the commission date. Furthermore, comparing the actual energy yield to the ideal situation, the system achieved an energy production of 51.9%, which increased to 53.9% from the commission date.

TABLE XI

MONTHLY ENERGY YIELD OF THE OES SYSTEM COMPARED TO SIMULATED VALUES

Month	**Energy yield [kWh]**	**Simulated energy yield (TMY) [kWh]**	**Simulated energy yield (clear sky) [kWh]**	**Energy yield / TMY**	**Energy yield / Clear sky**	**TMY / Clear sky**
June*	20.489	18.865	29.435	108.6%	69.6%	64.1%
July	160.228	173.030	332.221	92.6%	48.2%	52.1%
August*	107.401	81.0615	150.346	132.5%	71.4%	53.9%
September	72.492	76.990	126.750	94.2%	57.2%	60.7%
September**	27.484	24.442	34.617	112.4%	79.4%	70.6%
October	21.801	25.603	39.288	85.2%	55.5%	65.2%
November	0.712	1.4674	1.295	48.5%	55.0%	113.3%
December	0.000	0	0.000	N/A	N/A	N/A
January	0.055	0	0.037	N/A	149.9%	0.0%
February	5.811	11.2782	16.695	51.5%	34.8%	67.6%
March	16.640	53.416	94.534	31.2%	17.6%	56.5%
April	126.77	120.28	197.86	105.4%	64.1%	60.8%
Total**	**199.273**	**236.487**	**384.325**	**84.3%**	**51.9%**	**61.5%**
Total	**532.399**	**561.991**	**988.461**	**94.7%**	**53.9%**	**56.9%**

* Data starts from June 28, and dates between August 18 and 30 are excluded from analysis due to missing data.

** Indicates the research period from September 20 to April 30.

Fig. 68 compares the actual energy yield to the results obtained from the simulations with a daily resolution. The clear sky simulation (shown in red) provides a reference point for the system's performance under ideal conditions. On the other hand, the TMY simulation (in grey) shows the expected energy yield in a typical year. Although the actual energy yield (represented by the black line) follows the same trends as the TMY simulations, the fluctuations vary because actual weather conditions differ from the historically averaged meteorological data used in the TMY simulation. The results of the clear sky simulation do not display any fluctuations since they do not consider any weather data.

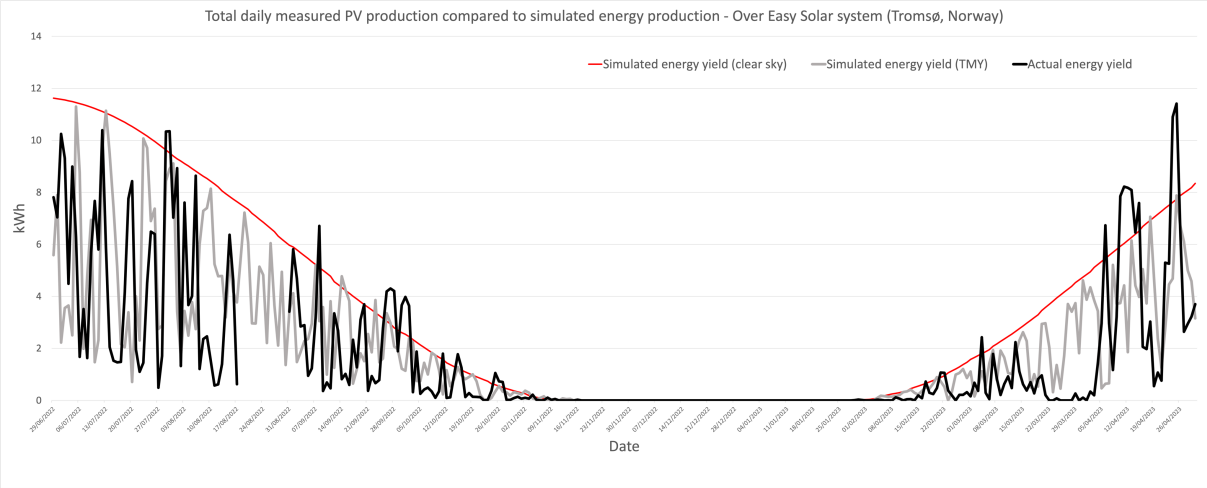

Fig. 68. Total daily measured energy yield of OES system (black) compared to simulated energy production in a TMY (light grey) and a clear sky analysis (red).

The comparison of the TMY and clear sky simulations reveals that, in some cases, the former outperforms the latter, which suggests a potential error in the clear sky meteorology file. This discrepancy is unexpected as both simulations assume similar conditions, and the TMY model should not yield higher energy production than the clear sky model. There is reason to believe that we have overestimated the Linke turbidity factor used in the clear sky simulation, leading to an overestimation of atmospheric absorption and scattering and, consequently, underestimating the system's energy yield. However, despite some outliers, the correlation between the two simulation models appears reasonable.

Moreover, we observe that the actual energy yield exceeds the clear sky simulation in multiple instances, spanning from July until the conclusion of the research period. This finding is also unexpected. We can attribute the causes for this inconsistency to several factors. Firstly, as mentioned, overestimating the Linke turbidity factor leads to

underestimating energy yield in the clear sky simulation. Secondly, the model does not consider changes in the albedo caused by the accumulation of snow around the solar cells, leading to a significant increase in the absorption of solar radiation. The effect of albedo could explain the substantial spikes we observed in April. These massive spikes were unexpected, emphasizing snow's effect as a reflector. Thirdly, there could be inaccuracies in the representation of the system in the models, which can result from both the classification as a HIT technology (instead of HJT) and the fact that the PVSyst software imperfectly represents vertically installed bifacial solar modules.

Excluding the months of polar night, when the energy production is low and consistent with our expectations, the OES system displays performances consistent with the predicted performance of the TMY simulation. Although the system’s representation is imperfect, the energy productions revolve around the same values. We interpret that these results can validate the results of the TMY simulations to a certain degree. However, February and March show significant deviations when the actual energy production reaches only 51.5% and 31.2% of the expected values, respectively, before returning to expected values in April. This discrepancy coincides with a significant snow accumulation in February and an abnormally high accumulation in March, as depicted in Fig. 65. The energy production displays two distinct periods (late February to early March and late March to early April) of particularly low performance, which we attribute to the impact of the snow.

The system performed better than expected in September and worse than expected in October. We can attribute it to the weather conditions in those months. September had clearer weather, resulting in better performance, while October had cloudier weather, leading to lower performance. The impact of cloud cover on energy production is evident. February had more cloudy and overcast weather than usual, contributing to low energy production. In contrast, March displayed clearer weather, but energy production still deviated even further from the expected value. Therefore, we assume that snow substantially negatively affected energy production during these months. In April, although the snow depth remained significant, the net effect of snow and more clear weather than usual had a net positive effect on the monthly performance of the system.

6.3.2 ILP system

Table XII compares the energy yield from actual observations and simulations. The TMY model predicts the system will produce 65.4% of the energy yield under ideal conditions during the research period. In contrast, the actual energy yield of the system during the research period corresponds to only 31.1% of the simulated energy yield in a TMY and 20.3% compared to the ideal scenario of the clear sky simulation.

TABLE XII

MONTHLY ENERGY YIELD OF THE ILP SYSTEM COMPARED TO SIMULATED VALUES

Month	Energy yield [kWh]	Simulated energy yield (TMY) [kWh]	Simulated energy yield (clear sky) [kWh]	Energy yield / TMY	Energy yield / Clear sky	TMY / Clear sky
September*	2496.92	2508.11	3991.17	99.6%	62.6%	62.8%
October	1840.23	2982.40	4036.50	61.7%	45.6%	73.9%
November	112.52	145.65	80.97	77.3%	139.0%	179.9%
December	0.00	0.00	0.00	N/A	N/A	N/A
January	0.15	0.00	1.18	N/A	12.3%	0.0%
February	189.69	1212.40	1553.40	15.6%	12.2%	78.0%
March	4.74	6761.40	10952.00	0.1%	0.0%	61.7%
April	4623.38	16182.00	24949.00	28.6%	18.5%	64.9%
Total	**9267.618**	**29791.960**	**45564.220**	**31.1%**	**20.3%**	**65.4%**

* Data starts from September 20.

Fig. 69 displays the daily energy yield of the ILP system as measured by the actual performance and the results of the simulations. The clear sky simulation, depicted in black, is a benchmark for the system's performance under ideal conditions. In contrast, the TMY simulation shows the expected energy yield in a typical year. Similar to the OES system, the actual energy yield follows the trends of the TMY simulation but displays fluctuations that differ due to variances in actual weather conditions compared to the historical weather data used in the TMY simulation. The results of the clear sky simulation do not display any fluctuations since they do not consider weather data.

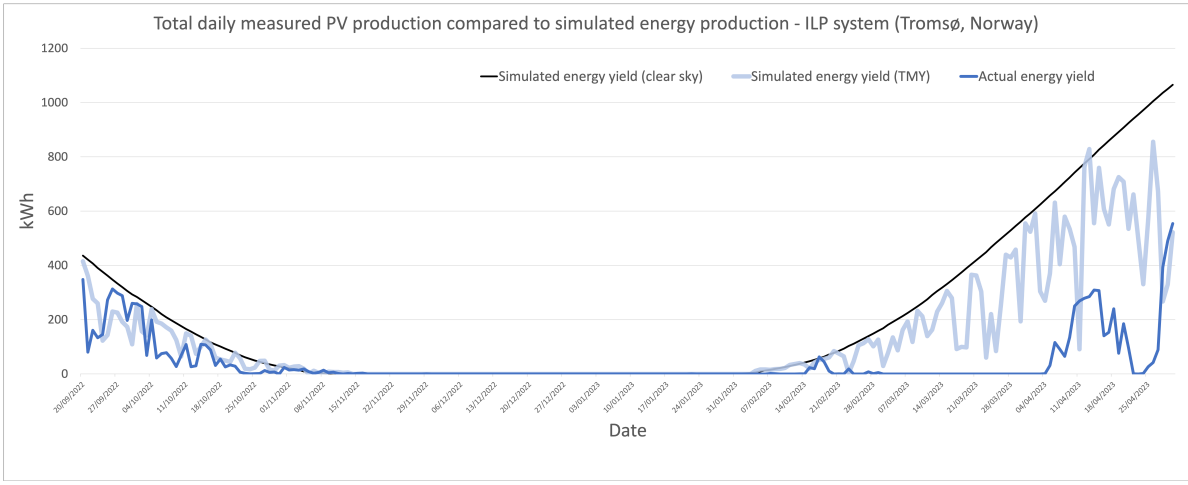

Fig. 69. Total daily measured energy yield of the ILP system (dark blue) compared to simulated energy production in a typical year (light blue) and a clear sky analysis (black).

The performance analysis of the ILP system using the TMY and clear sky simulations reveals similar tendencies to the OES system. In some instances, the TMY simulation slightly outperforms the clear sky simulation. We believe that the overestimation of the Linke turbidity factor is the cause of the discrepancy, leading to an underestimation of the system's energy yield under ideal conditions. Similarly, on some days, the actual energy yield exceeds the simulated energy yield of the clear sky model, which is unexpected. While the overestimation of the Linke turbidity factor is a possible contributing factor, the increased albedo due to roof snow cover and an imperfect representation of the system in the PVSyst software could also play a role. Despite these variations, the correlation between the simulations and the actual energy yield appears reasonable.

Investigating the connection between the actual energy yield and the simulated energy yield in a TMY, September performed as expected. We can use this result to validate that the results of the TMY simulation approximate what we can expect from the system. However, it was a month of more clear weather than usual, so we should expect this number to exceed the expected performance. If we had a few additional months before the snow accumulation began to validate that the actual values resemble the expected values, as we have for the OES system, this would strengthen the claim and validate the results. The PVSyst model of the system might be overestimating the expected system productions. October only achieved 61.7% of the expected energy yield, which is low. We can attribute this to the slight snow accumulation in late October and a month of less clear weather than usual.

November, December, and January exhibit low energy productions due to the period of polar night, which aligns with our expectations. Later, there was a significant decrease in energy production in February, March, and April, with the system producing only 15.6%, 0.1%, and 28.6% of the expected energy production, respectively. We can largely attribute the decrease to snow accumulation, which affects energy production massively. Although February was more cloudy and overcast than usual, March and April had clearer weather. However, the months produced energy far from the expected production. March is a prime example, as it had clearer weather than usual, but the system only produced 0.01% of the expected production.

6.3.3 Specific yield comparison and snow

We compare the total daily specific yields of the two systems in the research period in Fig. 70. As expected, the specific yield of the two systems follows the same pattern for significant parts of the period, which we can attribute to their proximity and the similar local weather patterns. However, there are deviations from this pattern, notably in late October and the period from February to early April. In this period, the specific yield of the ILP system is limited. The pattern then reverts to some degree in April. Overall, the specific yield of the OES system is higher than that of the ILP system.

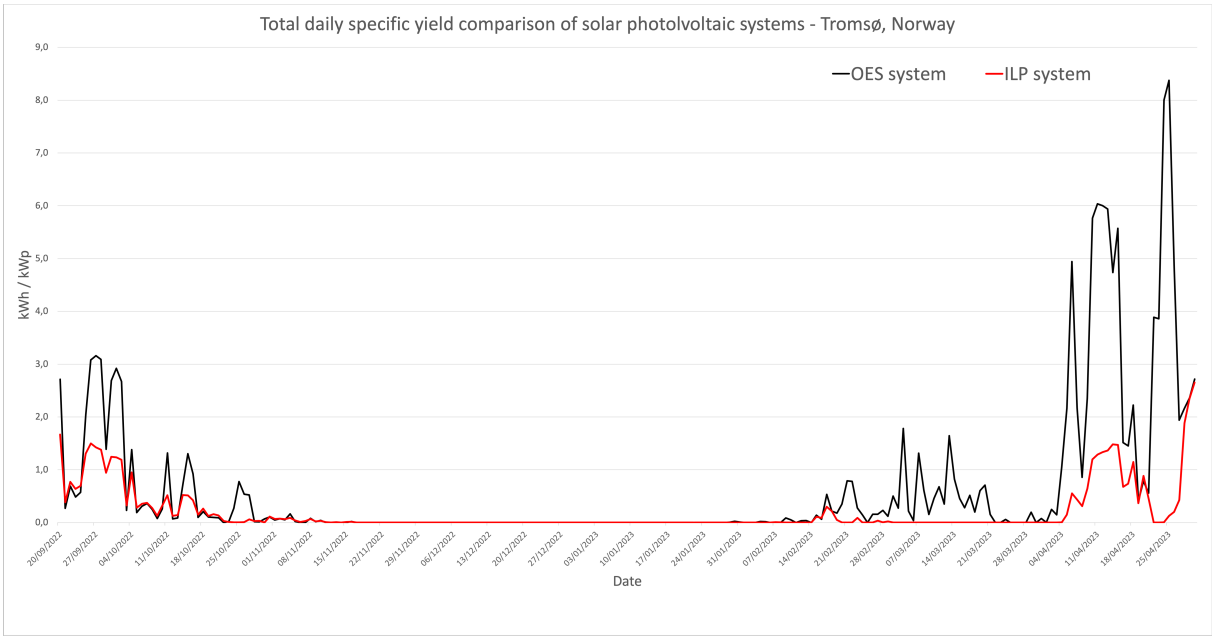

Fig. 70. Total daily specific yield comparison of OES (black) and ILP (red) solar photovoltaic systems.

During periods when the patterns of the systems' energy production coincide, particularly before the first snowfall, their relationship aligns with the expected characteristics. Specifically, the OES system outperforms the ILP system on peak days, typically clear or mostly clear weather days. In contrast, the systems exhibit similar performances between peaks, which are cloudy or overcast days. This trend persists until late October. However, we suspect that the different effects of snow on the systems cause major differences between the systems in the research period.

If we add the ground snow depth and snowfall days to Fig. 70, we reveal a pattern in Fig. 71. We can associate days of snowfall and a resulting rise in ground snow depth with severe dips

(toward zero) in the energy production of the ILP system. We have highlighted three snow crystals (with a circle) showing three occurrences where this phenomenon is particularly evident. We cannot find the same pattern for the energy production of the OES system, which appears less affected by snowfall, and only falls toward zero when the snow accumulation is significant.

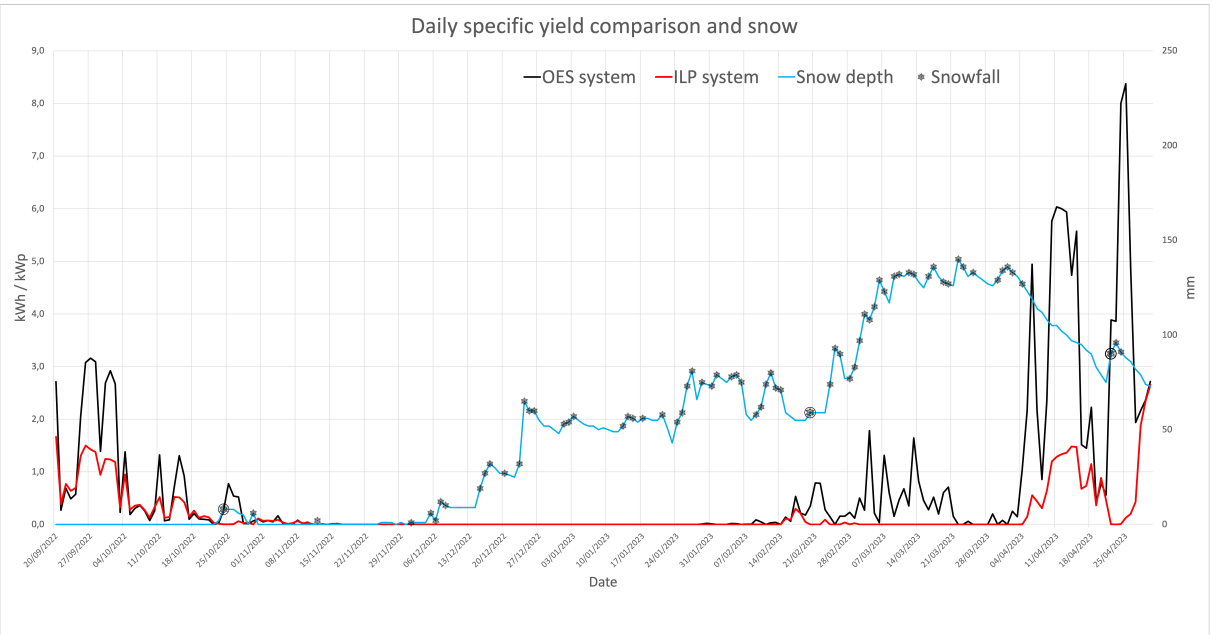

Fig. 71. Daily specific yield comparison of the systems (left axis) shown with the ground snow depth (right axis) in the research period. The black snow crystals indicate days of snowfall.

The ILP system is more prone to snow accumulation on the solar cell surface, and when in place, it can persist for an extended period. Fig. 71 visualizes this phenomenon, where the system barely produces energy from February to April. In contrast, the OES system continuously produces energy in this period, except for late March and early April, when the snow accumulation peaks. The observed trend is consistent with the expected differences in the impact of snow on the systems.

Fig. 72 illustrates the effect of snowfall on the two systems, showing light snowfall over the systems on February 19 and the specific yield of both systems graphed for the previous, same, and following days. On February 18, on a cloudy day before this snowfall, both systems and the ground next to them were free of snow, and the systems demonstrated comparable performances. However, on February 19, light snowfall occurred, resulting in the ILP solar

cells being entirely covered by a thin layer of snow, reducing energy production to zero, while the OES solar cells were free of snow and could take advantage of the increased albedo from the snow-covered ground. As a result, on February 20, exhibiting similar weather to February 18, the energy production of the ILP system was zero, while the OES system performed better than the day before the light snowfall. The increased performance is potentially due to the high albedo of the snow-covered roof.

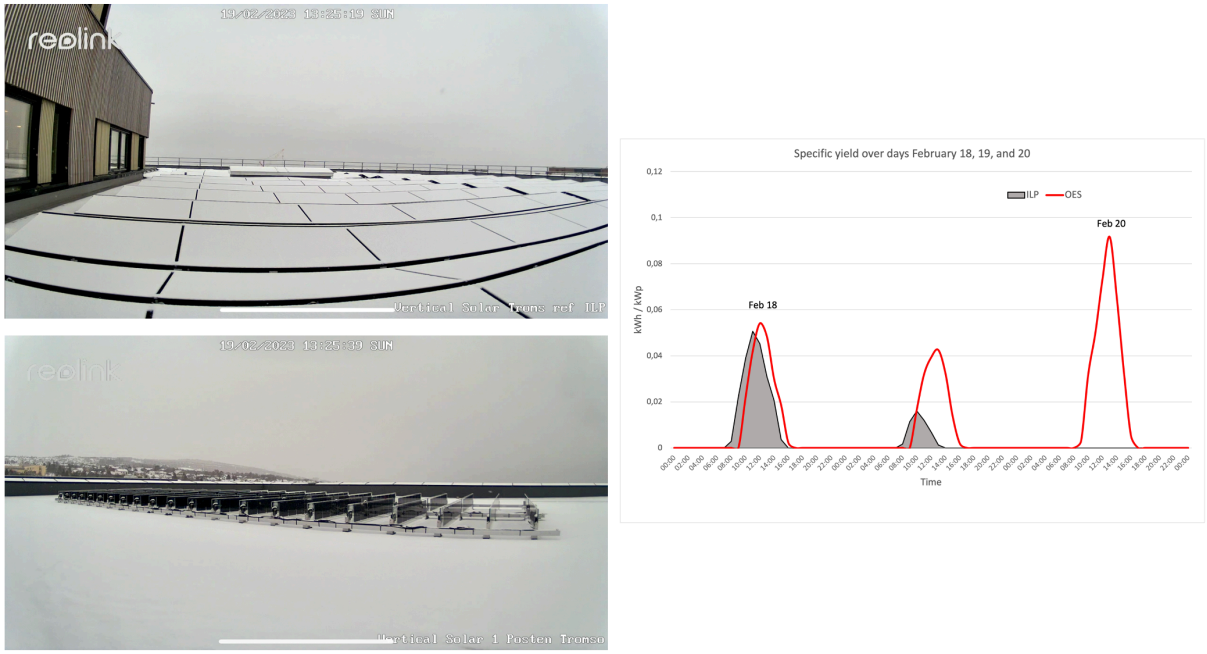

Fig. 72. Camera views of light snowfall on ILP (top left) and OES (bottom left) systems on February 19 with resulting specific yield comparisons on the previous, same, and following days (right).

Table XIII presents a rough estimate of the net effect (snow cover and albedo increase) of snow and other factors on energy production in the research period. Estimating this effect involves subtracting the TMY simulation ratio from the actual energy yield ratio to the clear sky simulation. By doing so, we remove the impact of weather (we separate snow from weather in in this regard) and find an approximation of the loss that we can attribute to snow and other factors. The values in the table thus represent the additional loss compared to the clear sky model after subtracting the expected loss due to weather.

TABLE XIII

LOSSES ATTRIBUTED TO NET EFFECT OF NON-WEATHER-RELATED FACTORS

Month	OES system	ILP system
September*	+8.8%	-0.3%
October	-9.7%	-28.3%
November	-58.3%	-40.9%
December	N/A	N/A
January	+149.9%	+12.3%
February	-32.7%	-65.8%
March	-38.9%	-61.7%
April	+3.3%	-46.4%
Total	**-7.6%**	**-45.1%**

These results illustrate how snow's effect on systems differs and do not precisely indicate the energy production losses due to a snow cover. Many factors can affect these values. We understand these values as a net effect of other factors, including both the losses due to snow cover and the gains due to an increased albedo. Understanding these values as simply the losses due to snow cover can be misleading, also considering that if snow entirely covers the modules, the weather is irrelevant, and the snow losses would therefore be higher.

Based on these results, snow has a more significant impact on the energy production of the ILP system compared to the OES system, especially during the months with the highest snow cover, which are February, March, and April. Variations in snow cover affect the energy performance of both systems during the research period, resulting in noticeable differences between them. Overall, the OES system experienced an additional loss of 7.6% over the entire research period, while the ILP system demonstrated an additional loss of 45.1%. Although other factors contribute, we attribute the primary cause for this difference to snow cover on the solar modules.

Fig. 73 comprises eight different graphs showing the specific yield of the two systems on selected days during the research period. We include May 1 even though it falls one day after the end of the research period because it was a clear weather day and marked the end state when both systems were snow-free. The graphs on the left depict clear weather days, where the OES system appears to outperform the ILP system, as expected. However, on May 1, at

the end of the research period, the difference between the systems was reduced compared to earlier in the research period. The graphs on the right side show cloudy days. As expected, the systems show similar performances on these cloudy days.

The production data of the two systems look shifted by approximately an hour. We can potentially attribute this shift to the distance between the systems and that passing clouds affect the systems at different times. However, we also acknowledge the possibility that the two solar monitoring systems have different reporting methodologies. It could be the case that the monitoring systems register the system production at different times. However, our focus is on the amplitude of the energy production, meaning that we do not expect this shift in system energy production to affect any of the performance metrics we approximate in this research. The monitoring systems register the energy production of each system on the correct day, and the number of hours of system production each day will not change, which is vital for the availability metric.

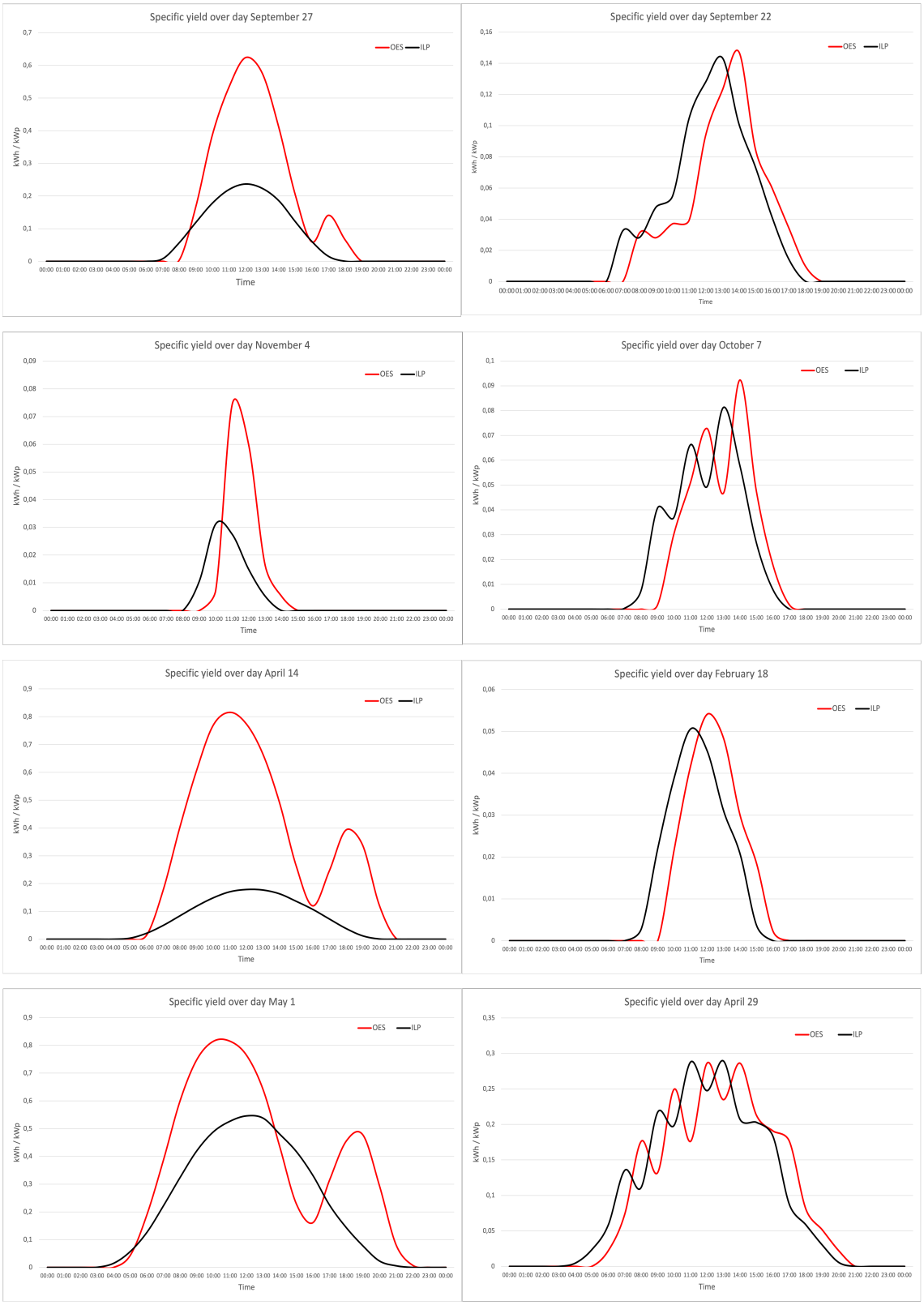

Fig. 73. Specific yield comparisons between the systems for selected days in the research period. The left column shows clear weather days, and the right shows cloudy days.

6.4 Availability

Table XIV presents the availability measurements of the OES system for each month compared to the simulated availability in a TMY. The rows marked in yellow indicate the research period from September 20. As evident from the data, the system's availability was highest in June, during which it produced energy 91.8% of the time. However, the availability gradually declines from June until it reaches 45.1% at the start of the research period and zero in December. Onwards, the availability increases towards April, abruptly reaching 60.1%. The total availability for the research period is 21.5%, increasing to 33.3% if we extend the period to the commission date.

TABLE XIV

TOTAL AVAILABILITY MEASUREMENTS FOR THE OES SYSTEM PER MONTH

Month	Simulated hours of energy production (TMY)	Hours of energy production	Total hours	Simulated availability	Availability
June*	60	56	61	98.4%	91.8%
July	636	603	744	85.5%	81.0%
August*	299	295	432	69.2%	68.3%
September	356	359	720	49.4%	49.9%
September**	117	119	264	44.3%	45.1%
October	220	230	744	29.6%	30.9%
November	40	43	720	5.6%	6.0%
December	0	0	744	0.0%	0.0%
January	0	8	744	0.0%	1.1%
February	137	115	672	20.4%	17.1%
March	305	201	744	41.0%	27.0%
April	432	433	720	60.0%	60.1%
Total**	**1251**	**1149**	**5352**	**23.4%**	**21.5%**
Total	**2485**	**2343**	**7045**	**35.3%**	**33.3%**

* Data starts from June 28, and dates between August 18 and 30 are excluded from analysis due to missing data.

** Indicates the research period from September 20 to April 30.

We look at the relationship between the expected and actual availability and find that the values are similar for most of the research period. Both simulated (expected) and actual availability follow the daylight-hours pattern from Fig. 22. However, there is a higher deviation between these values in February and March. This deviation indicates that snow has completely covered the system for parts of these months, consistent with the high snow accumulation in this period. The simulated availability in the research period is 1.9% higher than the actual availability, increasing to 2.0% from the date of commission.

Similar to Table XIV for the OES system, Table XV shows the availability measurements for the ILP system in the research period. The data reveals that the system's availability started at 49.2% in September. Subsequently, the availability decreases gradually, reaching zero in December. Onwards, it increases slightly in January and February but declines to near zero in March. April shows a significant increase to the highest availability in the research period, at 69.6%. The system demonstrates an overall availability of 19.4%.

TABLE XV

TOTAL AVAILABILITY MEASUREMENTS FOR THE ILP SYSTEM PER MONTH

Month	**Simulated hours of energy production (TMY)**	**Hours of energy production**	**Total hours**	**Simulated availability**	**Availability**
September*	119	130	264	45.1%	49.2%
October	242	250	744	32.5%	33.6%
November	44	71	720	6.1%	9.9%
December	0	0	744	0.0%	0.0%
January	0	3	744	0.0%	0.4%
February	151	73	672	22.5%	10.9%
March	320	8	744	43.0%	1.1%
April	438	501	720	60.8%	69.6%
Total	**1314**	**1036**	**5352**	**24.6%**	**19.4%**

* Data starts from September 20.

The expected availability of the ILP system exhibits a similar trend to the OES system concerning daylight hours. Similarly, the expected and actual values for this system align closely. However, a consistent discrepancy between the higher actual and expected availability until January indicates a flaw in the system's model representation, as these values should be more similar. As we progress into February and March, the deviations between these values reverse and increase. Notably, the March deviation of 41.9% implies that the system remained snow-covered for a significant portion of the month. Overall, the simulated availability surpasses the actual availability by 5.2%.

6.5 Performance ratio

Table XVI presents the estimated performance ratio of the OES system. The rows marked in yellow indicate the research period from September 20 onwards. The data indicates that the performance ratio remains relatively stable, ranging from 40% to 60% between June and November. While November, December, and January have limited available solar radiation, the performance ratio decreases to below 30% in February and below 20% in March. It increased to 51.0% in April, within the typical 40%-60% range. The calculated performance ratio for the research period is 41.3%, increasing to 45.7% if we extend the period to the commission date.

TABLE XVI

PERFORMANCE RATIO CALCULATIONS FOR THE OES SYSTEM

Month	**Energy yield [kWh]**	**Irradiation on front side [kWh/m^2]**	**Usable irradiation on rear side [kWh/m^2]**	**Performance ratio**
June*	20.489	14.029	8.094	53.9%
July	160.228	108.190	86.282	48.0%
August*	107.401	61.974	51.649	55.0%
September	72.492	50.899	42.876	45.0%
September**	27.484	13.716	13.039	59.8%
October	21.801	15.500	13.149	44.3%
November	0.712	0.520	0.464	42.1%
December	0.000	0.000	0.000	N/A
January	0.055	0.013	0.018	103.3%
February	5.811	6.469	5.595	28.0%
March	16.640	36.743	31.105	14.3%
April	126.770	78.933	65.901	51.0%
Total**	**199.273**	**151.894**	**129.271**	**41.3%**
Total	**532.399**	**373.270**	**305.133**	**45.7%**

* Data starts from June 28, and dates between August 18 and 30 are excluded from analysis due to missing data.

** Indicates the research period from September 20 to April 30.

Compared to the rest of the research period, the system exhibits a remarkably low performance ratio in February and March, meaning that the system less effectively converted incident energy into usable electricity during this period. We attribute this effect to significant snow accumulation in the period, affecting energy performance.

Like Table XVI for the OES system, Table XVII estimates the performance ratio for the ILP system. The data shows a performance ratio exceeding 60% and 40% in September and October. The system is inactive in November, December, and January due to the absence of usable irradiance. The performance ratio remains low in February, hits zero in March, and then increases to 19.4% in April. Overall, the calculated performance ratio for the research period is 21.2%.

TABLE XVII

PERFORMANCE RATIO CALCULATIONS FOR THE ILP SYSTEM

Month	**Energy yield [kWh]**	**Irradiation on front side [kWh/m^2]**	**Performance ratio**
September*	2496.921	20.022	64.3%
October	1840.228	20.804	45.6%
November	112.517	0.605	95.9%
December	0.000	0.000	N/A
January	0.146	0.022	3.4%
February	189.687	8.481	11.5%
March	4.740	53.265	0.0%
April	4623.38	122.640	19.4%
Total	**9267.619**	**225.839**	**21.2%**

* Data starts from September 20.

The results indicate a relatively high performance ratio for the system before the snow accumulation begins. However, from the first snowfall in late October, excluding the polar night months, the system exhibits a consistently low performance ratio, reaching 0.0% in March, even if March showed more clear weather days than usual. We can entirely attribute the low performance to the snow cover on the modules, hindering the solar radiation from reaching the solar cells, causing the system to be ineffective in converting incident energy into usable electricity during this period.

6.6 Capacity Factor

Table XVIII shows the capacity factor estimations for the OES system for each month compared to the simulated capacity factor in a TMY. The rows painted yellow mark the research period from September 20 onwards. The capacity factor commences at 25.5% in June, gradually declining towards 7.64% at the start of the research period and zero in December. We noticed a slight increase in the capacity factor in January, February, and March before it abruptly reached 12.93% in April. We estimate the overall capacity factor for the research period to be 2.73%, which improves to 5.55% if we extend the period to the commission date.

TABLE XVIII

CAPACITY FACTOR CALCULATIONS FOR THE OES SYSTEM

Month	Simulated energy yield [kWh]	Energy yield [kWh]	Time [h]	Theoretical maximum output [kWh]	Simulated capacity factor (TMY)	Capacity factor
Jun-22*	18.87	20.49	59	80.36	23.48%	25.50%
Jul-22	173.03	160.23	744	1013.33	17.08%	15.81%
Aug-22*	81.06	107.40	432	588.38	13.78%	18.25%
Sep-22	76.99	72.49	720	980.64	7.85%	7.39%
Sep-22**	24.44	27.48	264	359.57	6.80%	7.64%
Oct-22	25.60	21.80	744	1013.33	2.53%	2.15%
Nov-22	1.47	0.71	720	980.64	0.15%	0.07%
Dec-22	0.00	0.00	744	1013.33	0.00%	0.00%
Jan-23	0.00	0.06	744	1013.33	0.00%	0.01%
Feb-23	11.28	5.81	672	915.26	1.23%	0.64%
Mar-23	53.42	16.64	744	1013.33	5.27%	1.64%
Apr-23	120.28	126.77	720	980.64	12.27%	12.93%
Total**	**236.49**	**199.27**	**5352**	**7289.42**	**3.24%**	**2.73%**
Total	**561.99**	**532.40**	**7043**	**9592.57**	**5.86%**	**5.55%**

* Data starts from June 28, and dates between August 18 and 30 are excluded from analysis due to missing data.

** Indicates the research period from September 20 to April 30.

We find similar patterns to the availability and performance ratios upon investigating these values. The two months that stand out are February and March, where the capacity factors are low compared to the expected values. As with the other metrics, we attribute this difference to the impact of snow. In April, the capacity factor is back to expected values. The overall capacity factor for the ILP system is about 0.83% in the research period.

Table XIX shows the equivalent variables and capacity factor approximations for the ILP system for each month compared to the simulated capacity factor in a TMY. We observe a similar pattern for this system, commencing at 4.53% in September and gradually declining to zero in December. However, the capacity factor remained at zero in January, and we observed a slight increase in February before the capacity factor dropped back to zero in March. In April, there was an abrupt increase to 3.08%. The overall capacity factor for the ILP system is about 0.83% in the research period.

TABLE XIX

CAPACITY FACTOR CALCULATIONS FOR THE ILP SYSTEM

Month	Simulated energy yield	Energy yield [kWh]	Time [h]	Theoretical maximum output [kWh]	Simulated capacity factor (TMY)	Capacity factor
Sep-22*	2508.1	2496.9	264.0	55123.2	4.56%	4.53%
Oct-22	2982.4	1840.2	744.0	155347.2	1.92%	1.19%
Nov-22	145.7	112.5	720.0	150336.0	0.10%	0.08%
Dec-22	0.0	0.0	744.0	155347.2	0.00%	0.00%
Jan-23	0.0	0.1	744.0	155347.2	0.00%	0.00%
Feb-23	1212.4	189.7	672.0	140313.6	0.86%	0.14%
Mar-23	6761.4	4.7	744.0	155347.2	4.35%	0.00%
Apr-23	16182.0	4623.4	720.0	150336.0	10.76%	3.08%
Total	**29792.0**	**9267.6**	**5352.0**	**1117497.6**	**2.67%**	**0.83%**

* Data starts from September 20.

We observe that February, March, and April show significantly reduced capacity factors compared to the expected values, strengthening the claim that snow cover of the modules substantially affects the system performance in all these months.

6.7 Comparing the energy performance metrics

Table XX summarizes each system's key energy performance metrics and compares them. The green cells indicate OES results, and the yellow ones show the ILP results. The higher value is bolded, and the difference between them is shown below in the color of the higher performer.

TABLE XX

SUMMARIZING TABLE OF SOLAR IRRADIATION (TMY) AND ENERGY PERFORMANCE METRICS

Month	Solar irradiation [kWh/m^2]	Availability		Specific yield [kWh/kW$_p$]		Performance ratio		Capacity factor	
September*	17.82	45.1%	**49.2%**	**20.18**	11.96	59.8%	**64.3%**	**7.64%**	4.53%
		+4.2%		**+8.22**		**+4.5%**		**+3.11%**	
October	19.22	30.9%	**33.6%**	**16.01**	8.81	44.3%	**45.6%**	**2.15%**	1.19%
		+2.7%		**+7.20**		**+1.3%**		**+0.96%**	
November	1.50	6.0%	**9.9%**	0.52	**0.54**	42.1%	**95.9%**	0.07%	**0.08%**
		+3.9%		**+0.02**		**+53.8%**		**+0.01%**	
December	0.00	0.0%	0.0%	0.00	0.00	N/A	N/A	0.00%	0.00%
		0.0%		0.00		N/A		0.00%	
January	0.00	**1.1%**	0.4%	**0.04**	0.00	**103.3%**	3.4%	**0.01%**	0.00%
		+0.7%		**+0.04**		**+99.9%**		**+0.01%**	
February	8.68	**17.1%**	10.9%	**4.27**	0.91	**28.0%**	11.5%	**0.64%**	0.14%
		+6.2%		**+3.36**		**+16.5%**		**+0.50%**	
March	38.75	**27.0%**	1.1%	**12.22**	0.02	**14.3%**	0.0%	**1.64%**	0.00%
		+25.9%		**+12.20**		**+14.3%**		**+1.64%**	
April	84.34	60.1%	**69.6%**	**93.08**	22.14	**51.0%**	19.4%	**12.93%**	3.08%
		+9.5%		**+70.94**		**+31.6%**		**+9.85%**	
Total	**170.31**	**21.5%**	19.4%	**146.31**	44.39	**41.3%**	21.2%	**2.73%**	0.83%
		+2.1%		**+101.92**		**+20.1%**		**+1.90%**	

* Data starts from September 20.

We divide the research period into three parts: the fall months of September and October, the polar night and winter months of November, December, and January, and the winter and spring months of February, March, and April. We split them into these parts based on the characteristic performance features of the systems.

During September and October, the ILP system demonstrated a higher availability and performance ratio than the OES system. It had a higher operational uptime, indicating that the system placement and design allow it to intercept solar radiation for a larger fraction of the day. We suspect that the difference in altitude between the systems and the four different system orientations are contributing factors. The ILP system also produced more energy relative to its expected performance under ideal conditions. The ideal conditions imply converting all solar energy incident on the cells under clear skies into usable electricity at its STC-rated efficiency. The system thus exhibits a greater overall operational efficiency. On the other hand, the OES system showed a higher specific yield and capacity factor, indicating that it exhibits a higher energy production efficiency and greater utilization of its capacity. We can attribute this to the increased absorption of solar radiation due to the bifacial modules and the higher efficiency of the HJT technology cells compared to the c-Si cells.

We cannot conclude on system performances in terms of the performance metrics based on the data of the polar night period (November to January). The reason is that small changes in energy production during this period can significantly alter the energy performance metrics. Therefore, we should interpret the results from these months with caution, considering that they may not be representative of the overall performance of the systems. However, we can look at the data and find clues on which system performs better in low-daylight conditions. The data shows that the ILP system outperformed the OES system in November, performing better across all the metrics. The ILP system thus utilized the low available solar radiation in November better.

We observe that the snow accumulation was much more significant in January than in November and thus had a more significant effect on the systems. The OES system performed better in these conditions, as expected in a snowy environment. It thus performed better across all metrics in January, although it barely produced anything. Both of the systems were inactive in December.

Starting from February, except for the availability in April, the OES system outperformed the ILP system significantly in all energy performance metrics. Snow's different effects on the system performances overshadow the performance metrics in this period. We use availability as evidence. The OES system has far superior availability in February, particularly in March, where it exhibits a 25.9% higher availability, in line with the month of abnormally high snow depth. The major difference indicates that snow covered the ILP system for most of March. Although the ILP system had higher availability than the OES system in April, the OES system had a considerably higher performance ratio, specific yield, and capacity factor. The low values of other energy performance metrics of the ILP system in this period suggest that although it produced energy, it was likely partially covered by snow for a long time, affecting all energy performance metrics.

Because the ILP system exhibited higher availability and performance ratio before the snow accumulation became significant, these findings suggest that the OES system performs better in snowy conditions. This claim is consistent with the earlier discussion on the advantages of the OES system in such conditions, indicating that the systems perform as expected.

Overall, the OES system performs better than the ILP system on every energy performance metric, with a 2.1% higher availability, 20.1% higher performance ratio, 1.90% higher capacity factor, and a 230% higher (101.9 kWh/kW_p) specific yield.

7 Discussion

In this study, we investigated and compared the performance of two solar PV systems in Tromsø, focusing on energy yield, specific yield, availability, performance ratio, and capacity factor. The systems under investigation were a vertically installed bifacial heterojunction technology (HJT) system and a 10°-tilted monofacial crystalline silicon (c-Si) system. Our findings provide valuable insights into the energy performance of these systems in a high-latitude region characterized by challenging environmental conditions. Next, we want to relate our research to existing studies conducted on systems in similar climatic settings, providing an understanding of their respective performance characteristics and the implications for future solar PV deployments in high-latitude regions.

Our research suggests that the vertically installed bifacial modules of the OES system perform better than the 10°-tilted monofacial modules of the ILP system in the research period. We will discuss our findings from different perspectives.

First, we focus on the bifacial and monofacial properties of the systems, where for our systems, the bifacial system demonstrates superior performance in snowy conditions. Multiple studies based on simulations also suggest that bifacial modules are favorable in high-latitude areas. Guo et al. [83] conducted a study suggesting that in the conventional way of mounting monofacial solar modules – facing south (towards the equator) with an angle approximating the latitude of the location of the installation [84] – bifacial modules can generate up to 20% more energy compared to side-by-side monofacial modules in high-latitude areas. This benefit increases with the latitude and duration of the snow cover, which benefits our high-latitude system in Tromsø, with 163 days of snow cover recorded in the research period.

The OES system in our research demonstrated a significantly higher specific yield and capacity factor than the monofacial system, which underlines the benefits of increased absorption of bifacial modules. However, according to a study performed by Asgharzadeh et al. [85], the advantage of bifacial systems is more pronounced in small systems with ample open space, which is the case for the OES system in our study. Based on this study, we could expect performance to decrease if we expand the pilot project due to increased self-shading from the system.

Furthermore, our study emphasized that the snow surrounding and covering the bifacial system melts quicker than for a monofacial system, which a study performed by Hayibo et al. [86] underlines. Their study hypothesizes that the backside heating causes the surrounding snow to melt faster, and our study supports this hypothesis. The difference between the systems in this regard was stunning.

Researchers have also studied the importance of orientations of systems. East-west-facing systems can take advantage of the long hours of the low-angle morning and evening sun on typical summer days and the low solar elevation during winter [87]. Both systems in our study have modules facing east-west, and both perform well in low solar elevation conditions. These strengths were most prominent before snow accumulation began. Furthermore, combining orientations to even out the energy production during the day presents an exciting opportunity [87]. The OES system is faced in two directions due to its bifaciality, while the ILP system consists of modules faced in four directions. Thus, the ILP system shows one broad peak of electricity production, which we expect to be even broader in the summer with more daylight hours. In contrast, the OES system typically exhibits two distinct peaks: one in the morning and one in the afternoon. Adding new modules to the OES system facing north-south would be an exciting expansion of the pilot project, particularly because a study by Ito et al. [88] claims that east-west and north-south-facing vertically installed bifacial modules exhibit similar performances in high-latitude regions.

Studies on the optimal tilt angle of solar modules are of high importance. The study of Ito et al. [88] points out the distinct advantages of vertically installed systems in terms of an optimal orientation for harvesting reflected light from the snow-covered ground. The OES system demonstrated an extremely high energy yield towards the end of April, far exceeding the clear sky simulation. This finding suggests that the system took advantage of the high albedo of the snow-covered ground, supporting the advantages of these systems. Furthermore, the study emphasizes the advantage of reducing soiling caused by snow accumulation, which could be an issue for conventionally installed monofacial modules. This advantage is the most prominent finding in our research. The ILP solar cells have an even lower elevation angle than a conventional installation, making them more prone to snow accumulation, and we have found that this severely affects energy production.

Linking tilt angle and orientation, the study by Ito et al. [88] further suggests that vertically mounted bifacial systems are 10%-30 % more energy efficient than conventionally installed

monofacial systems in high-latitude regions. The seasonal gain is highest in the summer and lowest in the winter, indicating that if we had extended the study to include the summer, we might have seen a more significant difference between the systems. However, the ILP system installers have not installed conventionally, so we cannot directly draw links to our study.

It seems natural to compare the energy performance metrics of our systems to other systems. For the two systems in research, the energy performance metrics availability, performance ratio, and capacity factor are, by definition, highly dependent on the availability of solar radiation. By our definition, the availability of a system has an upper limit depending on the number of daylight hours, meaning that comparison to systems at lower latitudes would not be helpful. However, the difference between the simulated and actual availability adds to the existing body of literature on the effect of tilt angle on snow accumulation on solar cells, emphasizing the importance of a high tilt angle.

Furthermore, the performance ratio metric is calculated differently in various sources and research, and many of the choices made in the calculation, such as which losses to include and which not to include, make a significant difference regarding performance ratio comparisons between systems. These variations limit the suitability of the metric for comparisons, and researchers do not typically compare large PV power based on their performance ratios [89]. Therefore, we have used the same method for both systems in our study to compare them accurately, but we will not further compare these performance ratios to those of other systems.

On the other hand, the capacity factor is more widely used for comparisons, and solar photovoltaic systems' annual capacity factor typically ranges between 10%-25% [90]. However, these values can be higher in regions with excellent solar resources and lower in regions with worse solar resources. The systems in our research demonstrate a low capacity factor, which can be attributed to the high-latitude installation site and the short duration of the research period, not including the summer months. In order to compare the capacity factor of the systems to typical values, we must continue the research for an entire year.

The KGPV classification [31] describes locations in the EL climate zone as cold climate locations with frequent snowfall, long winters, and a low amount of solar irradiation. Our findings in Tromsø are consistent with all the elements of the expected weather. The classification does not consider Tromsø an ideal installation location, and based on our

findings, there are many climate-related challenges for solar photovoltaic systems, especially the snow and low solar elevation. The two technologies show different characteristics in these conditions during winter, and even though none of the systems produce energy in the polar night period, the OES system is most suited for snowy conditions.

These findings show that we can successfully adapt solar photovoltaic technologies to the environment where we want to deploy them. The vertical bifacial installation allows the system to withstand snow accumulation and simultaneously take advantage of the increased snow cover albedo. Therefore, despite the region's non-ideal conditions, we consider it a viable option for winter conditions. Our research thus proves the importance of performing field studies of technologies to identify technological improvements that can make them successful in new regions.

The research in this thesis contributes to the existing body of knowledge by further demonstrating the considerable benefit of bifacial PV modules to increase absorption and significantly enhance energy production compared to monofacial PV modules in high-latitude regions. In addition, our study has contributed significantly to understanding the critical correlation between solar module tilt angle and snow accumulation, where higher module tilts are favorable to avoid snow accumulation that causes significant production losses. Furthermore, our research contributes with field measurements of two different solar photovoltaic technologies adding to the knowledge of solar photovoltaic viability in high-latitude regions and the impact of snow on energy production.

8 Conclusion

We conducted our research in Tromsø, situated at a high latitude of 69°N, with a maximum solar elevation of 44° and periods of polar day and night shaping solar radiation availability. Our study revealed an estimated annual solar irradiation of 750 kWh/m^2, and along with low temperatures consistent with historical averages, the KGPV classification classifies Tromsø as an unfavorable city for large-scale solar photovoltaic system installations. The observed weather is consistent with the characteristics of the classification. Approximately 60% of days each month typically exhibit mostly cloudy or overcast weather. However, cloud cover analysis in the research period revealed that September, November, March, and April were relatively clear, and October, January, and February experienced more cloudy weather than usual. We observed snow cover 163 out of 222 days, consistent with the expected annual 150-200 days, with March standing out for its abnormally high snow depth.

The research findings revealed that while there were variations from month to month, the OES system performed better across all performance metrics overall. These performances entail a 2.1% higher availability, a 20.1% higher performance ratio, and a 1.90% higher capacity factor. Generally, the OES system performed better on clear weather days, while the systems exhibited comparable performances on cloudy days. Neither of the systems produced significant amounts of energy in the polar night months of November, December, and January. Regarding specific yield, the OES system produced 146.31 kWh/kW_p compared to the ILP system's 44.39 kWh/kW_p, indicating a 230% higher specific yield. The spring months constitute the biggest difference between the systems, where the most significant disparity occurred in March, likely due to the abnormally high snow depth.

We found that the 10°-tilted ILP system is more prone to snow accumulation on the solar cell surfaces than the vertically installed OES system, and even light snowfall could render the ILP system's power output zero. In addition, an accumulated layer remained in place for a long time. In contrast, the OES system capitalized on increased albedo, leading to significant energy production spikes. Accumulated layers of snow around the modules melted quickly. We removed the weather effects and roughly estimated an additional loss of -7.6% for the OES system and -45.1% for the ILP system. We primarily attributed these losses to snow, with the ILP system suffering significantly higher snow-related losses.

Our study concludes that the vertically installed HJT technology bifacial OES system performed better than the 10°-tilted c-Si monofacial ILP during the research period. The OES system's ability to withstand snow accumulation and capitalize on increased albedo contributed to its superior performance, and it excelled in the specific environmental conditions of Tromsø. The findings indicate that the technology is viable in these regions in winter conditions. On the other hand, the ILP system was significantly affected by snow for an extended period, making it inactive for a long time. However, we emphasize that the system performances observed during this period may not represent the entire year, as solar irradiation levels and environmental conditions differ significantly throughout other months. Therefore, a comprehensive study is necessary to conclude the systems' full-year performances.

9 Further work

The study of solar cells in high-latitude regions is a topic of broad interest. However, the lack of substantial research could prevent or limit further technology deployment in the regions. Based on the findings of this research, we suggest further work to extend and improve the study:

- Perform calculations on the energy production per roof area for the systems to find out which system better utilized the available roof area.

- Extend the study to a full year. It would be interesting to investigate and include the effect of the midnight sun in a whole year and look at the full-year performances of the systems. A full-year study would make it easier to conclude which technology performs better in high-latitude regions. Data from a full year also makes comparisons of the performance metrics to systems in other regions make sense.

- Install the two technologies side-by-side to keep all external factors constant. Another interesting variant would be to install two identical systems of each technology and manually remove snow from one but not the other to estimate the snow losses of each system accurately. We could perform similar actions for single strings of solar modules in large systems, where we manually clear snow from one string but not the adjacent one.

- Expand the vertically installed HJT technology OES system to include north-south-facing modules to investigate the difference in performances between the orientations.

- Perform more TMY simulations specifying the effects of soiling losses and albedo on each system and see if it is possible to align the results with the actual production. For this purpose, it would also be beneficial to visually observe and find methods to quantify the snow cover of the system daily or at least frequently.

- Distinguish the effect of an increased albedo and soiling losses on energy production and see the fraction of each. It would be interesting to assess the relationship between these effects and find if the sum is positive or negative for each month of the research period and if this relationship changes.

10 Bibliography

[1] G. o. Canada, "Remote Sensing Tutorials - Interactions with the Atmosphere," Government of Canada, 02 03 2016. [Online]. Available: https://www.nrcan.gc.ca/maps-tools-publications/satellite-imagery-air-photos/remote-sensing-tutorials/introduction/interactions-atmosphere/14635. [Accessed 30 January 2023].

[2] "Albedo," Energy Education, [Online]. Available: https://energyeducation.ca/encyclopedia/Albedo. [Accessed 10 May 2023].

[3] "The AM1.5 Spectrum," Ossila, [Online]. Available: https://www.ossila.com/pages/standard-solar-spectrum. [Accessed 13 April 2023].

[4] "BIFACIAL SOLAR PANELS: CHARACTERISTICS AND ADVANTAGES," Trace Software International, [Online]. Available: https://www.trace-software.com/bifacial-solar-panels-characteristics-and-advantages/. [Accessed 12 February 2023].

[5] "Bifacial PV technology: technical considerations," DNV, [Online]. Available: https://www.dnv.com/article/bifacial-pv-technology-technical-considerations-186095. [Accessed 10 May 2023].

[6] "The Solar Spectrum," Ossila, [Online]. Available: https://www.ossila.com/pages/the-solar-spectrum. [Accessed 11 May 2023].

[7] S. E. T. Office, "Solar Radiation Basics," U.S. Department of Energy, Solar Energy Technologies Office. [Online]. Available: https://www.energy.gov/eere/solar/solar-radiation-basics. [Accessed 01 February 2023].

[8] SoDa (Solar radiation Data), "LINKE TURBIDITY (TL) FACTOR WORLDWIDE," MINES ParisTech / Transvalor, [Online]. Available: https://www.soda-pro.com/help/general-knowledge/linke-turbidity-factor. [Accessed 6 May 2023].

[9] "Solar radiation: what is its impact on the planet and on humans?," Iberdrola, [Online]. Available: https://www.iberdrola.com/social-commitment/solar-radiation. [Accessed 29 May 2023].

[10] E. Hecht, Optics, 5th global edition, Pearson Education Limited , 2017.

[11] "Soiling (solar energy)," Wärtsilä, [Online]. Available: https://www.wartsila.com/encyclopedia/term/soiling-solar-energy-. [Accessed 10 April 2023].

[12] Sciencing, "What Is Solar Altitude?," LEAF GROUP LTD., [Online]. Available: https://sciencing.com/solar-altitude-23364.html. [Accessed 10 February 2023].

[13] "Insolation," Energy Education, [Online]. Available: https://energyeducation.ca/encyclopedia/Insolation. [Accessed 27 May 2023].

[14] Global Solar Atlas, "What's the difference between DNI, DIF and GHI?," The World Bank Group, [Online]. Available: https://globalsolaratlas.info/support/faq. [Accessed 27 May 2023].

[15] "What Is Solar Noon?," Time and Date AS, [Online]. Available: https://www.timeanddate.com/astronomy/solar-noon.html. [Accessed 8 May 2023].

[16] "angle of incidence," Merriam Webster, [Online]. Available: https://www.merriam-webster.com/dictionary/angle%20of%20incidence. [Accessed 27 May 2023].

[17] "Solar Energy," SEIA, [Online]. Available: https://www.seia.org/initiatives/about-solar-energy. [Accessed 22 May 2023].

[18] "Solar Energy Basics," NREL, [Online]. Available: https://www.nrel.gov/research/re-solar.html. [Accessed 24 May 2023].

[19] "Solar power generation, 2022," Our World in Data, [Online]. Available: https://ourworldindata.org/grapher/solar-energy-consumption. [Accessed 14 May 2023].

[20] "Renewables 2022," IEA, Paris, 2022.

[21] F. M. Fossland, "Literature review of the use and performance of monofacial and bifacial solar modules in high latitude regions," UiT The Arctic University of Norway, Tromsø, 2022.

[22] "electromagnetic spectrum," Britannica, [Online]. Available: https://www.britannica.com/science/electromagnetic-spectrum. [Accessed 10 May 2023].

[23] "The Electromagnetic Spectrum," Mini Physics, [Online]. Available: https://www.miniphysics.com/electromagnetic-spectrum_25.html. [Accessed 12 May 2023].

[24] C. Honsberg and S. Bowden, "Atmospheric Effects," Photovoltaics Education Website, [Online]. Available: https://www.pveducation.org/pvcdrom/properties-of-sunlight/atmospheric-effects. [Accessed 29 May 2023].

[25] C. Honsberg and S. Bowden, "Air Mass," [Online]. Available: https://www.pveducation.org/pvcdrom/properties-of-sunlight/air-mass. [Accessed 12 May 2023].

[26] "Sunrise and sunset times > Tromsø, Norway," Suncurves AS, [Online]. Available: https://suncurves.com/en/v/17634/. [Accessed 12 May 2023].

[27] "Clouds and Climate," CMMAP, [Online]. Available: https://hogback.atmos.colostate.edu/cmmap/learn/clouds/climate2.html. [Accessed 10 May 2023].

[28] "Clouds and Albedo," National Learning Network for Remote Sensing, [Online]. Available: https://www.nln.geos.ed.ac.uk/courses/english/ars/a3110/a3110008.htm. [Accessed 10 May 2023].

[29] Y. Kotak, M. S. Gul, T. Muneer and S. M. Ivanova, "Investigating the Impact of Ground Albedo on the Performance of PV Systems," in *CIBSE Technical Symposium*, London, 2015.

[30] A. El Ouiqary, E. Kheddioui and M. F. Smiej, "Estimation of the global horizontal solar irradiation GHI for the Moroccan national territory from meteorological satellite images of the Second Generation Meteosat series MSG," *European Journal of Molecular & Clinical Medicine,* vol. 08, no. 03, 2021.

[31] J. Ascencio-Vásquez, K. Brecl and M. Topič, "Methodology of Köppen-Geiger-Photovoltaic climate classification and implications to worldwide mapping of PV system performance," *Solar Energy,* vol. 191, pp. 672-685, 2019.

[32] "Country and regional maps," PHOTOVOLTAIC GEOGRAPHICAL INFORMATION SYSTEM, [Online]. Available: https://re.jrc.ec.europa.eu/pvg_download/map_index.html. [Accessed 28 May 2023].

[33] "Country and regional maps - Germany," PVGIS, [Online]. Available: https://re.jrc.ec.europa.eu/pvg_download/map_index.html#!. [Accessed 14 May 2023].

[34] C. Honsberg and S. Bowden, "Calculation of Solar Insolation," Photovoltaics Education Website, 2019. [Online]. Available: https://www.pveducation.org/pvcdrom/properties-of-sunlight/calculation-of-solar-insolation. [Accessed 6 March 2023].

[35] M. Loster, "Total Primary Energy Supply — From Sunlight," 2010. [Online]. Available: https://www.ez2c.de/ml/solar_land_area/. [Accessed 6 Mar 2023].

[36] "Photovoltaic effect," Energy Education, [Online]. Available: https://energyeducation.ca/encyclopedia/Photovoltaic_effect. [Accessed 9 February 2023].

[37] C. Honsberg and S. Bowden, "Introduction," Photovoltaics Education Website, [Online]. Available: https://www.pveducation.org/pvcdrom/introduction/introduction. [Accessed 9 February 2023].

[38] "semiconductor," Britannica, [Online]. Available: https://www.britannica.com/science/semiconductor. [Accessed 29 May 2023].

[39] "What are Semiconductors – Properties of Semiconductors," Nuclear Power, [Online]. Available: https://www.nuclear-power.com/nuclear-engineering/radiation-detection/semiconductor-detectors/what-are-semiconductors-properties-of-semiconductors/. [Accessed 15 February 2023].

[40] NREL, "Solar Photovoltaic Technology Basics," The National Renewable Energy Laboratory (NREL), [Online]. Available: https://www.nrel.gov/research/re-photovoltaics.html. [Accessed 15 February 2023].

[41] C. Honsberg and S. Bowden, "Semiconductor Structure," Photovoltaics Education Website, [Online]. Available: https://www.pveducation.org/pvcdrom/pn-junctions/semiconductor-structure. [Accessed 29 May 2023].

[42] C. Honsberg and S. Bowden, "Conduction in Semiconductors," Photovoltaics Education Website, [Online]. Available: https://www.pveducation.org/pvcdrom/conduction-in-semiconductors. [Accessed 12 May 2023].

[43] C. Honsberg and S. Bowden, "Band Gap," Photovoltaics Education Website, [Online]. Available: https://www.pveducation.org/pvcdrom/pn-junctions/band-gap. [Accessed 29 May 2023].

[44] C. Honsberg and S. Bowden, "Doping," Photovoltaics Education Website, [Online]. Available: https://www.pveducation.org/pvcdrom/pn-junctions/doping. [Accessed 14 May 2023].

[45] C. Honsberg and S. Bowden, "Formation of a PN-Junction," Photovoltaics Education Website, [Online]. Available: https://www.pveducation.org/pvcdrom/pn-junctions/formation-of-a-pn-junction. [Accessed 14 May 2023].

[46] "PN Junction," AnkPlanet, [Online]. Available: https://ankplanet.com/physics/modern-physics/semiconductor-devices/pn-junction/. [Accessed 14 May 2023].

[47] C. Honsberg and S. Bowden, "Absorption of Light," Photovoltaics Education Website, [Online]. Available: https://www.pveducation.org/pvcdrom/pn-junctions/absorption-of-light. [Accessed 29 May 2023].

[48] C. Honsberg and S. Bowden, "Optical Properties of Silicon," Photovoltaics Education Website, [Online]. Available: https://www.pveducation.org/pvcdrom/materials/optical-properties-of-silicon. [Accessed 15 May 2023].

[49] C. Honsberg and S. Bowden, "Collection Probability," Photovoltaics Education Website, [Online]. Available: https://www.pveducation.org/pvcdrom/solar-cell-operation/collection-probability. [Accessed 16 May 2023].

[50] "Our Technology," QD Solar, [Online]. Available: https://qdsolarinc.com/technology/#. [Accessed 16 May 2023].

[51] S. Sharma, K. K. Jain and A. Sharma, "Solar Cells: In Research and Applications—A Review," *Materials Sciences and Applications,* vol. 6, no. 12, pp. 1145-1155, 2015.

[52] S. De Wolf, A. Descoedres, Z. C. Holman and C. Ballif, "High-efficiency Silicon Heterojunction Solar Cells: A Review," *Green,* vol. 2, no. 1, p. 7–24, 2012.

[53] "Heterojunction Solar Panels: How They Work & Benefits," Solar Magazine, [Online]. Available: https://solarmagazine.com/solar-panels/heterojunction-solar-panels/. [Accessed 27 May 2023].

[54] C. Honsberg and S. Bowden, "Refining Silicon," Photovoltaics Education Website, [Online]. Available: https://www.pveducation.org/pvcdrom/manufacturing-si-cells/refining-silicon. [Accessed 18 May 2023].

[55] C. Honsberg and S. Bowden, "Types of Silicon," Photovoltaics Education Website, [Online]. Available: https://www.pveducation.org/pvcdrom/manufacturing-si-cells/types-of-silicon. [Accessed 27 May 2023].

[56] "Made how - Solar Cell," Advameg, Inc., [Online]. Available: http://www.madehow.com/Volume-1/Solar-Cell.html. [Accessed 27 May 2023].

[57] J. Svarc, "Solar Panel Construction," Clean Energy Reviews, 20 March 2020. [Online]. Available: https://www.cleanenergyreviews.info/blog/solar-panel-components-construction. [Accessed 01 February 2023].

[58] C. Honsberg and S. Bowden, "Module Circuit Design," Photovoltaics Education Website, [Online]. Available: https://www.pveducation.org/pvcdrom/modules-and-arrays/module-circuit-design. [Accessed 27 January 2023].

[59] C. Honsberg and S. Bowden, "Photovoltaics Education Website," 2019. [Online]. Available: https://www.pveducation.org/pvcdrom/welcome-to-pvcdrom/instructions. [Accessed 27 January 2023].

[60] C. Honsberg and S. Bowden, "Bypass Diodes," Photovoltaics Education Website, [Online]. Available: https://www.pveducation.org/pvcdrom/modules-and-arrays/bypass-diodes. [Accessed 10 February 2023].

[61] R. Vieira, F. M. U. de Araújo, M. Dhimish and M. I. d. S. Guerra, "A Comprehensive Review on Bypass Diode Application on Photovoltaic Modules," *Energies,* vol. 13, p. 2472, 2020.

[62] D. Hahn, "What are DC power optimizers?," SolarReviews, 20 12 2022. [Online]. Available: https://www.solarreviews.com/blog/complete-guide-to-power-optimizers. [Accessed 01 February 2023].

[63] C. Good, H. Persson, Ø. Kleven, W. Sulkowski, K. Ellingsen and T. Boström, "SOLAR CELLS ABOVE THE ARCTIC CIRCLE -MEASURING CHARACTERISTICS OF SOLAR PANELS UNDER REAL OPERATING CONDITIONS," in *24th European Photovoltaic Solar Energy Conference (EUPVSEC)*, Hamburg, 2009.

[64] fjordtours, "Polar night season in Tromsø," fjordtours, 13 Jan 2020. [Online]. Available: https://www.fjordtours.com/inspiration/articles/polar-night-season-tromsoe-norway/. [Accessed 12 May 2023].

[65] Visit Nordic", "Midnight Sun in Tromsø," VisitNordic, [Online]. Available: https://www.visitnordic.com/en/midnight-sun-in-tromso. [Accessed 12 May 2023].

[66] Z. Peng, M. R. Herfatmanesh and Y. Liu, "Cooled solar PV panels for output energy efficiency optimisation," *Energy Conversion and Management,* vol. 150, pp. 949-955, 2017.

[67] E. Andenæs, B. P. Jelle, K. Ramlo, T. Kolås, J. Selj and S. E. Foss, "The influence of snow and ice coverage on the energy generation from photovoltaic solar cells," *Solar Energy,* vol. 159, pp. 318-328, 2018.

[68] S. A. Hansen, "Bifacial Solar Cells in Nordic Climate," Norwegian University of Science and Technology (NTNU), 2018.

[69] A. J. Dietz, C. Wohner and C. Kuenzer, "European Snow Cover Characteristics between 2000 and 2011 Derived from Improved MODIS Daily Snow Cover Products," *Remote sensing,* vol. 4, pp. 2432-2454, 2012.

[70] Seaward Electronic Ltd, "What is solar PV I-V curve tracing?," Seaward Electronic Ltd, [Online]. Available: https://www.seaward.com/gb/support/solar/faqs/84179-what-is-solar-pv-i-v-curve-tracing/. [Accessed 22 February 2023].

[71] A. Walker and J. Desai, "Understanding Solar Photovoltaic System Performance - An Assessment of 75 Federal Photovoltaic Systems," U.S. Department of Energy, Office of Energy Efficiency and Renewable Energy, Dec 2021. [Online]. Available: https://www.energy.gov/sites/default/files/2022-02/understanding-solar-photo-voltaic-system-performance.pdf. [Accessed 24 February 2023].

[72] The National Renewable Energy Laboratory (NREL), "Solar PV AC-DC Translation," NREL, U.S. Department of Energy, Office of Energy Efficiency and Renewable Energy, [Online]. Available: https://atb.nrel.gov/electricity/2021/pv-ac-dc. [Accessed 27 February 2023].

[73] "PVSyst," PVsyst SA, [Online]. Available: https://www.pvsyst.com/. [Accessed 19 February 2023].

[74] PVSyst SA, "PVSyst 7 Grid-connected tutorial," PVSyst SA, 2020. [Online]. Available: https://www.pvsyst.com/wp-content/uploads/2020/10/PVsyst_Tutorials_V7_Grid_Connected.pdf. [Accessed 13 May 2023].

[75] "NASA-SSE data," PVSyst, [Online]. Available: https://www.pvsyst.com/help/meteo_source_nasa.htm. [Accessed 10 March 2023].

[76] SMA Solar Technology AG, "Operating manual - SUNNY BOY 1.5 / 2.0 / 2.5," 26 Jan 2022. [Online]. Available: https://files.sma.de/downloads/SBxx-1VL-40-BE-en-19.pdf. [Accessed 10 March 2023].

[77] PVGIS, "PHOTOVOLTAIC GEOGRAPHICAL INFORMATION SYSTEM," European Commission - EU Science Hub, [Online]. Available: https://re.jrc.ec.europa.eu/pvg_tools/en/#PVP. [Accessed 7 March 2023].

[78] PVSyst, "PVSyst 7 Help - Bifacial Systems," [Online]. Available: https://www.pvsyst.com/help/index.html?bifacial_procedure.htm. [Accessed 18 March 2023].

[79] Solar Mango, "Performance Ratio of Solar Power Plant – Definition, Glossary, Details – Solar Mango," [Online]. Available: https://www.solarmango.com/dictionary/performance-ratio/. [Accessed 9 April 2023].

[80] SolarEdge, "Accuracy of the SolarEdge Monitoring System, Technical Note," [Online]. Available: https://enelogic-blog.s3.eu-west-1.amazonaws.com/files/Accuracy-of-the-SolarEdge-Monitoring-System.pdf. [Accessed 13 March 2023].

[81] SMA Solar Technology AG, "Measurement accuracy - Energy values and efficiency for PV Inverter Sunny Boy and Sunny Mini Central," [Online]. Available: https://files.sma.de/downloads/Messgenau-UEN092520.pdf. [Accessed 13 March 2023].

[82] "PVSyst 7 Help - Validations," PVSyst, [Online]. Available: https://www.pvsyst.com/help/index.html?validations.htm. [Accessed 15 March 2023].

[83] S. Guo, T. M. Walsh and M. Peters, "Vertically mounted bifacial photovoltaic modules: A global analysis," *Energy,* vol. 61, pp. 447-454, 2013.

[84] M. de Witt, H. Stefánsson, Á. Valfells and J. N. Larsen, "Energy resources and electricity generation in Arctic areas," *Renewable Energy,* vol. 169, pp. 144-156, 2021.

[85] A. Asgharzadeh, B. Marion, C. Deline, C. Hansen, J. S. Stein and F. Toor, "A Sensitivity Study of the Impact of Installation Parameters and System Configuration on the Performance of Bifacial PV Arrays," *IEEE JOURNAL OF PHOTOVOLTAICS,* vol. 8, no. 3, pp. 798-805, 2018.

[86] K. S. Hayibo, A. Petsiuk, P. Mayville, L. Brown and J. M. Pearce, "Monofacial vs bifacial solar photovoltaic systems in snowy environments," *Renewable Energy,* vol. 193, 2022.

[87] S. Jouttijärvi, G. Lobaccaro, A. Kamppinen and K. Miettunen, "Benefits of bifacial solar cells combined with low voltage power grids at high latitudes," *Renewable and Sustainable Energy Reviews,* vol. 161, 2022.

[88] M. Ito and E. Gerritsen, "Geographical Mapping of the Performance of Vertically Installed Bifacial Modules," in *32nd EUPVSEC*, Munich, 2016.

[89] "Comparisons of PR factors for large-scale solar PV power plants limited," pv magazine group, [Online]. Available: https://www.pv-magazine.com/2020/05/27/comparisons-of-pr-factors-for-large-scale-solar-pv-power-plants-limited/. [Accessed 25 May 2023].

[90] "What is capacity factor and how do solar and wind energy compare?," What Next Now, [Online]. Available: https://www.whatnextnow.com/home/solar/what-is-capacity-factor-and-how-does-solar-energy-compare. [Accessed 25 May 2023].